INFORMATION TO USERS

This manuscript has been reproduced from the microfilm master. UMI films the text directly from the original or copy submitted. Thus, some thesis and dissertation copies are in typewriter face, while others may be from any type of computer printer.

The quality of this reproduction is dependent upon the quality of the copy submitted. Broken or indistinct print, colored or poor quality illustrations and photographs, print bleedthrough, substandard margins, and improper alignment can adversely affect reproduction.

In the unlikely event that the author did not send UMI a complete manuscript and there are missing pages, these will be noted. Also, if unauthorized copyright material had to be removed, a note will indicate the deletion.

Oversize materials (e.g., maps, drawings, charts) are reproduced by sectioning the original, beginning at the upper left-hand corner and continuing from left to right in equal sections with small overlaps.

Photographs included in the original manuscript have been reproduced xerographically in this copy. Higher quality 6" x 9" black and white photographic prints are available for any photographs or illustrations appearing in this copy for an additional charge. Contact UMI directly to order.

Bell & Howell Information and Learning
300 North Zeeb Road, Ann Arbor, MI 48106-1346 USA

UMI®
800-521-0600

CHIP FORMATION AND SURFACE INTEGRITY IN HIGH SPEED MACHINING OF HARDENED STEEL

By

HOSSAM ELDEEN A. KISHAWY

A Thesis

Submitted to the School of Graduate Studies

in Partial Fulfilment of the Requirements

for the Degree of

Doctor of Philosophy

McMaster University

CHIP FORMATION AND SURFACE INTEGRITY IN HIGH SPEED MACHINING

DOCTOR OF PHILOSOPHY (1998) McMaster University

(Mechanical Engineering) Hamilton, Ontario

Title: CHIP FORMATION AND SURFACE INTEGRITY IN HIGH SPEED MACHINING OF HARDENED STEEL

Author: Hossam Eldeen A. Kishawy, B.Sc. (Honor), M.Sc.

Supervisor: Professor M. A. Elbestawi

Number of pages: xvii, 202

ABSTRACT

Increasing demands for high production rates as well as cost reduction have emphasized the potential for the industrial application of hard turning technology during the past few years. Machining instead of grinding hardened steel components reduces the machining sequence, the machining time, and the specific cutting energy. Hard turning is characterized by the generation of high temperatures, the formation of saw toothed chips, and the high ratio of thrust to tangential cutting force components. Although a large volume of literature exists on hard turning, the change in machined surface physical properties represents a major challenge. Thus, a better understanding of the cutting mechanism in hard turning is still required. In particular, the chip formation process and the surface integrity of the machined surface are important issues which require further research.

In this thesis, a mechanistic model for saw toothed chip formation is presented. This model is based on the concept of crack initiation on the free surface of the workpiece. The model presented explains the mechanism of chip formation. In addition, experimental investigation is conducted in order to study the chip morphology. The effect of process parameters, including edge preparation and tool wear on the chip morphology, is studied using Scanning Electron Microscopy (SEM). The dynamics of chip formation are also investigated.

The surface integrity of the machined parts is also investigated. This investigation

focusses on residual stresses as well as surface and sub-surface deformation. A three dimensional thermo-elasto-plastic finite element model is developed to predict the machining residual stresses. The effect of flank wear is introduced during the analysis. Although residual stresses have complicated origins and are introduced by many factors, in this model only the thermal and mechanical factors are considered. The finite element analysis demonstrates the significant effect of the heat generated during cutting on the residual stresses. The machined specimens are also examined using x-ray diffraction technique to clarify the effect of different speeds, feeds and depths of cut as well as different edge preparations on the residual stress distribution beneath the machined surface. A reasonable agreement between the predicted and measured residual stress is obtained. The results obtained demonstrate the possibility of eliminating the existence of high tensile residual stresses in the workpiece surface by selecting the proper cutting conditions.

The machined surfaces are examined using SEM to study the effect of different process parameters and edge preparations on the quality of the machined surface. The phenomenon of material side flow is investigated to clarify the mechanism of this phenomenon. The effect of process parameters and edge preparations on sub-surface deformation is also investigated.

ACKNOWLEDGMENTS

The author would like to express his sincere gratitude to his research supervisor Professor M. Elbestawi for his guidance, support, encouragement, and helpful advice throughout the course of this research. Sincere appreciation is also expressed to the members of the supervisory committee Dr. S. Subramanian and Dr. M. Sklad for their helpful discussions.

Special thanks and appreciations goes to all the colleagues and staff at the mechanical engineering department for their help at various occasions. In particular, thanks to Dr. T. Elwardany for her help and useful discussions and to Ms. C. Gerhard and Ms. R. Clifford for reviewing the manuscript.

Dedicated to my wife, Rehab, and my son, Ahmed, who accompanied me along the way

and in memory of my grandfather, Ali, who inspired me to enter this field

TABLE OF CONTENTS

CHAPTER 3 CHIP FORMATION

CHAPTER 4 RESIDUAL STRESSES: EXPERIMENTAL INVESTIGATION

CHAPTER 5 RESIDUAL STRESSES: FINITE ELEMENT ANALYSIS

LIST OF FIGURES

LIST OF TABLES

CHAPTER 1

INTRODUCTION

1.1 Motivation and background

Turning of hardened steel (hard turning) is an economical method of generating a high quality machined surface. The high potential of hard machining to increase productivity, to offset environmental concerns by using dry cutting, as well as its competitiveness (high surface quality of 0.2 μm R_a) with grinding processes, have generated a significant industrial interest in hard turning. As an example, hard turning of automotive differential side gears is one successful industrial application of hard machining. Traditionally, grinding was the preferred method for finished machining of hardened steel. The advent of super hard tool materials has made it possible to circumvent the traditional machining practice for hardened steels. Although a high surface quality has been achieved

in earlier investigations, industrial application of this technology is still rather limited. This is due to the uncertainties related to the integrity of the surfaces produced and the resulting part accuracy. Surface quality and integrity of hard machined parts are affected by many factors such as process variables, tool wear and cutting edge preparation.

The surface quality of a machined part is typically assessed in terms of parameters such as surface texture (roughness, waviness, material side flow, etc.) and dimensional tolerances. For hardened steel components, however, the sub-surface damage produced by machining process affects its resistance to fatigue, creep, and stress corrosion cracking (Bailey et al., 1976). Clearly, it is important to ascertain the integrity of the machined surface, particularly when the components produced are used under severe service conditions of stresses, temperature, and environment.

Surface integrity includes the existence of microcracks, phase transformation, residual stresses imposed by the machining process, the pull-out of carbides from the grain boundary, intergranular attack, plastic deformation, and changes in the subsurface microhardness. These factors determine the behaviour and service life of the components produced. Numerous valuable data and empirical equations on surface integrity, including residual stresses, have been previously published. However, most of these studies were performed to investigate the machined surface in soft steel. In addition, the fundamental relationship between the metal cutting mechanism and surface integrity was not clarified in any of these previous studies.

1. 2 Scope of the work

The mechanism of hard machining is investigated throughout this work. The study consists of two main parts. The first part is focussed on studying the mechanism of saw toothed chip formation during hard machining. In the second part, the surface quality and integrity of the hard machined part is investigated.

The study of saw toothed chip formation included modelling of the chip formation mechanism as well as extensive experimental observations. A mechanistic model was developed to explain the mechanism of saw toothed chip formation. In order to examine chip morphology, chips were collected after each cutting test and examined under the optical and the scanning electron microscope. The experimental investigation includes the effect of process parameters and edge preparation on the chip morphology. In addition, the dynamics of the chip formation were investigated and correlated to the fluctuations in the cutting force signal.

In studying the surface quality and integrity of the machined surface, the research is focussed on residual stresses, surface and sub-surface deformation and the phenomenon of material side flow. The study of residual stresses includes three dimensional finite element modelling for predicting residual stresses, as well as an experimental investigation of residual stresses during hard machining. Residual stresses have a very complicated origin and are introduced by many factors. However, in this investigation, only the thermal and mechanical loads are considered.

Two types of hard steels were utilized in these investigations, case hardened steel

(AISI 1550) and tool steel (D2). Although, both case hardened steel and tool steel were used in modelling the residual stresses, the sub-surface deformation study focussed only on the machining of die materials (D2 steel). In studying the surface quality, attention was given to the origin of the phenomenon of material side flow which was observed during hard machining.

1.3 Thesis outline

This thesis is comprised of seven chapters. Chapter two presents an overview of the relevant research work in this area. It covers three main topics; hard turning, chip formation, and surface integrity.

In Chapter three, the development of a model for saw toothed chip formation is presented. In addition, an experimental investigation is presented in order to study the effect of process parameters on chip morphology during the machining of hardened steel.

Chapter four covers the study of residual stresses during hard machining. This study includes experimental investigation using x-ray diffraction technique. In this chapter, the effect of feed, depth of cut, cutting speed, and edge preparation on residual stress distribution is investigated.

Chapter five presents a three dimensional finite element model for the prediction of residual stresses during machining process. In this model, both mechanical and thermal loads are considered. To include the thermal effect, thermo-elasto-plastic finite element analysis is used.

Chapter six presents an experimental study of the surface and sub-surface deformation during the machining of hardened steel. Surface roughness was measured and the machined surface was examined using a scanning electron microscope. In particular, attention is given to the mechanism of material side flow on the machined surface and the effect of different parameters on its mechanism. In addition, this study includes the examination of the sub-surface deformation and phase transformation.

Chapter seven presents a summary of this study as well as suggestions for future work in this area.

CHAPTER 2

LITERATURE REVIEW

2.1 Introduction

This chapter consists of three main sections describing special features of hard turning, chip formation, and surface integrity.

2.2 Hard turning

Increasing demands for higher production rates as well as cost reductions have emphasized the potential for wide spread industrial application of hard turning. Industrial application of hard turning shows a great reduction in the production sequences and savings in the production time and cost. Figure 2.1 shows a comparison between conventional and optimized production sequences using hard turning (Köing et al., 1990). The machining time

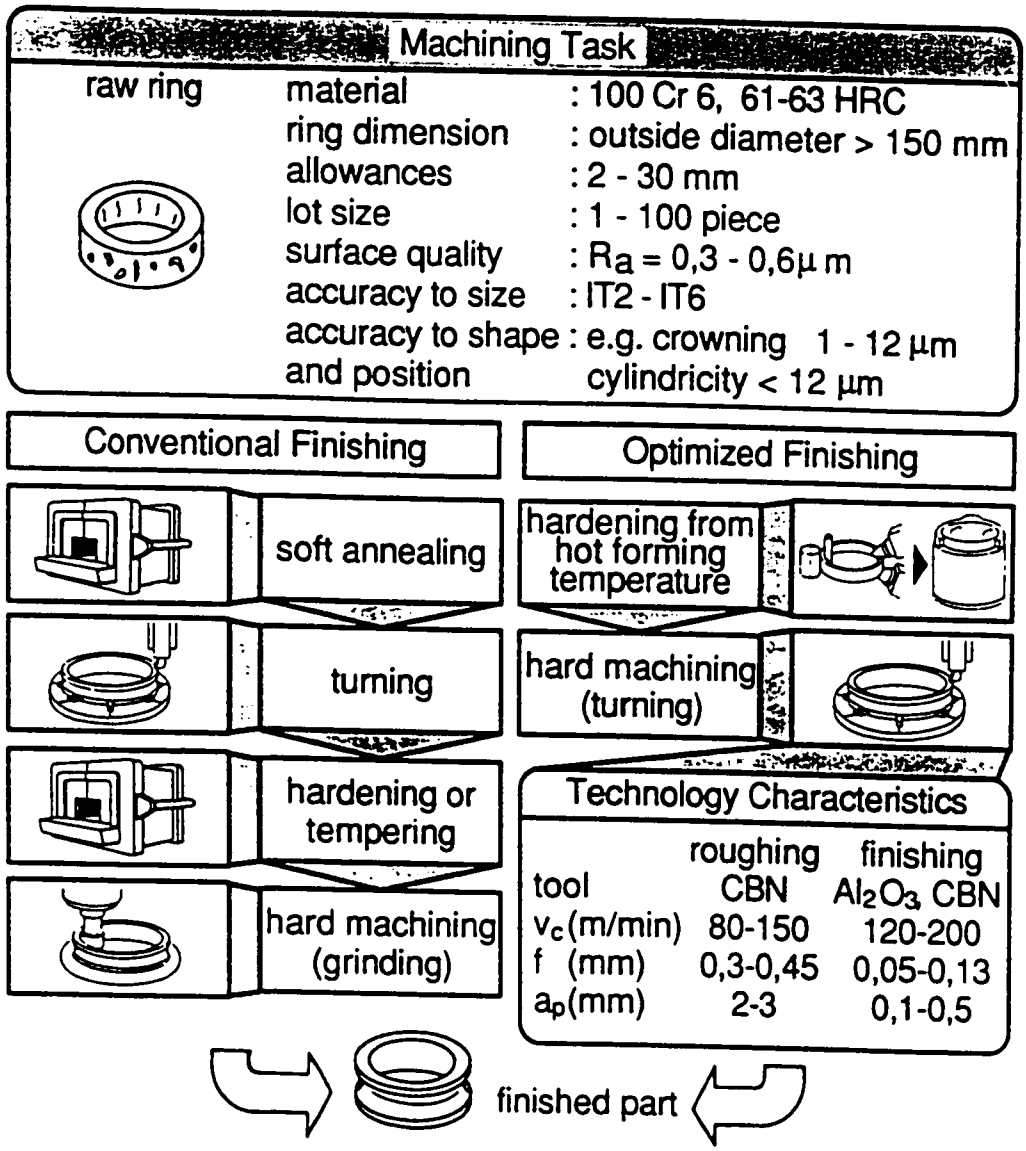

Fig. 2.1 Conventional and optimized production sequences for the production of the roller bearing rings (König et al., 1990)

is reduced to almost 40 % of the time required for a grinding. Figure 2.2 shows the benefits of hard turning as an alternative machining process to grinding of the gear component.

Steel with hardness higher than 30 Rc is difficult to cut, particularly at low cutting speeds, where the cutting forces were found to be much higher (Trent, 1991). Recently, the development of new cutting materials such as alumina based ceramic reinforced with titanium carbide (Al_2O_3/TiC), and Polycrystalline Cubic Boron Nitride (PCBN), have made it possible to machine hardened steel. The hard turning process is characterized by the generation of high temperature, high ratio of thrust to tangential force components, low specific energy consumption compared to grinding, relatively low cutting forces, and the formation of the saw toothed chips. The formation of the saw toothed chips produces high dynamic forces. These forces affect the cutting tool wear pattern and, consequently, the accuracy of the workpiece produced. Figure 2.3 shows saw toothed chip obtained during machining of case hardened steel (König et al., 1990).

Although high surface quality has been achieved in earlier investigations, industrial application of hard turning technology is still limited. This is due to the uncertainties with regard to the properties of the produced surface. When hardened steel is machined, its surface tends to undergo phase transformation due to the heat generated. In addition, since the chip formation is created mainly at the tool radius, a high ploughing force is generated which, in turn, generates mechanical compressive residual stress at the outer surface. During machining a wear land is developed at the tool workpiece interface. The larger the magnitude of wear land, the higher the thermal load produced. Thus, the depth of the plastic

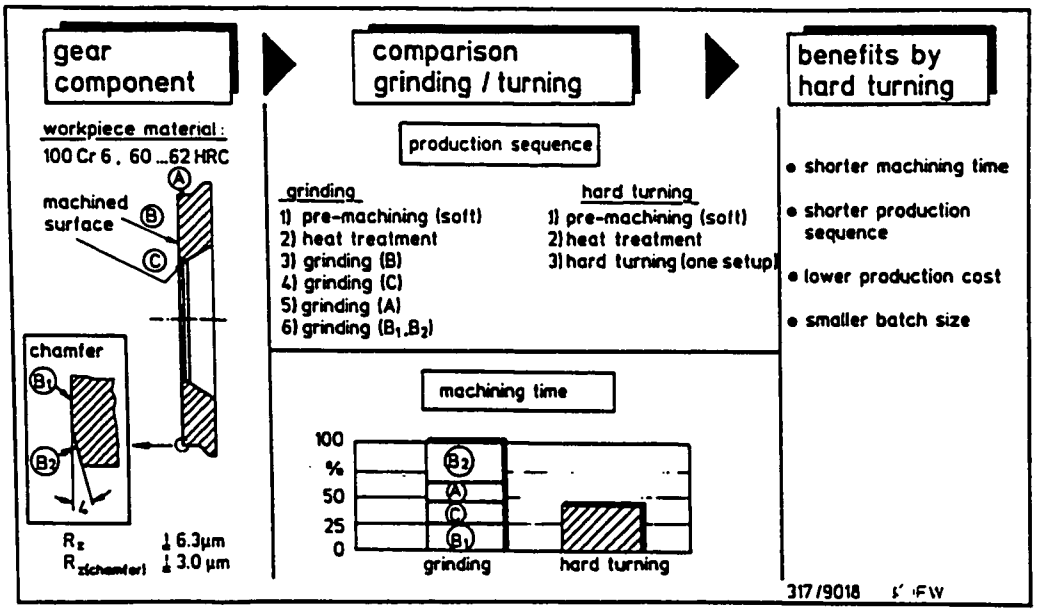

Fig. 2.2 Hard turning versus grinding (Tönshoff et al., 1995c)

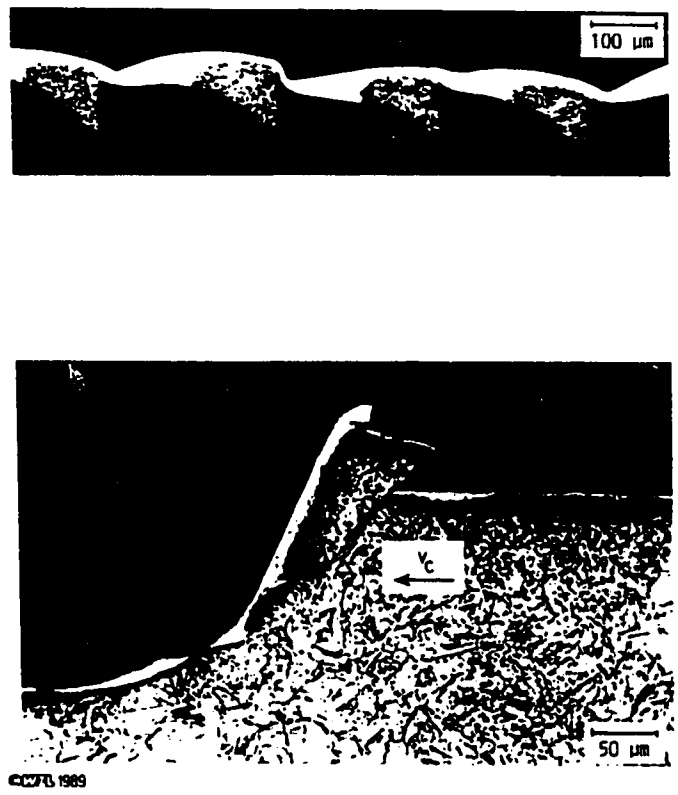

Fig. 2.3 Chip formation during machining of case hardened steel (König et al., 1990)

zone increases as well as the maximum value of the tensile residual stress.

During the metal removal process, it is assumed that all the work done is converted into thermal energy. The main sources of thermal energy produced are the plastic deformation associated with the chip formation and the friction between the wear land and the workpiece. The thermal energy generated affects both the tool and the workpiece. Thermal expansion is a result of the thermal energy developed in the workpiece. In a turning operation, the thermal expansion of the tool and the workpiece increase the effective depth of cut. Increasing the depth of cut leads to a reduction in the produced workpiece size. Fortunately, most of the heat generated is dissipated with the chips produced and only about 20% flows into the workpiece.

In a hard turning operation, the thermal strain results mainly from the friction between the wear land and workpiece. Most of the heat generated at the wear land, approximately 80%, flows into the workpiece (König et al., 1993). In hard turning, coolants are often not used in order to reduce the cost and to eliminate tool breakage due to thermal shock (Tönshoff et al., 1995a). Thus, thermal expansion of the parts produced by hard turning should be much more significant than that in conventional turning operation. The use of coolants in hard turning applications is not essential unless extremely close dimensional tolerances are required (Tönshoff et al., 1995a). Meanwhile, dry cutting has its advantages since it decreases the waste disposal of cooling and lubricating liquids as well as their potential hazardous environmental effects. In addition, dry cutting at high cutting speed can eliminate the distortion of the workpiece surface produced and increase the tool life.

Moreover, intense increase in the cutting edge temperature softens the workpiece material which, in turn, decreases the cutting forces and, consequently, the power consumption.

To understand the process of hard turning, one needs a better understanding of its cutting mechanism. The cutting process involves a different chip formation process, wear mechanisms and their effects on the surface integrity of the machined surface.

2.2.1 Special features of hard turning

Hard turning is different from the conventional turning process. As a finishing operation, the depth of cut and the feed are fairly small. Cutting tools with relatively large cutting edge radius are normally used. Thus, the chip formation takes place exclusively in the corner radius and on the chamfer of the cutting tool. In addition, a chamfered cutting edge is used to reduce the chipping of the cutting edge. Figure 2.4 shows the typical geometrical conditions in hard turning. Hard turning has some special features such as:

a- Negative rake angle

Cutting tools having a negative rake angle are normally used in hard turning to reduce the chipping of the cutting edge. In fact, the highly abrasive quality of the workpiece material blunts the cutting edge which further increases the negative effective rake angle.

b- Saw toothed chips

Saw toothed chips are usually formed during hard turning. This can be attributed to the brittleness of the workpiece material.

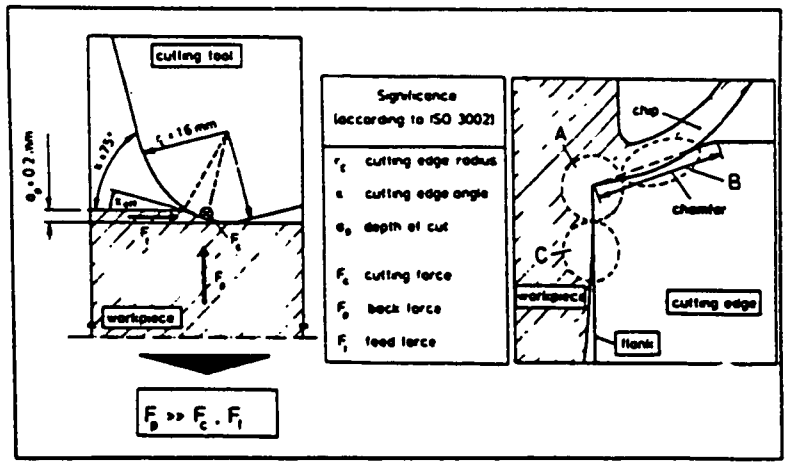

Fig. 2.4 Geometrical conditions in hard turning (Tönshoff et al., 1995a)

c- High ratio of thrust to cutting force component

In hard turning, the thrust force component (F_p) appears to be the largest force component. The force ratio F_p/F_c is always greater than one. A significant increase of the force ratio F_p/F_c is also observed with an increase in cutting length.

d- Relatively low specific energy consumption

Relatively, the specific cutting energy consumed during hard turning is much less than that in grinding operation.

e- Low cutting forces

The high temperature generated during hard turning facilitates the thermal softening in the cutting zone. Hence, the cutting forces are reduced.

2.2.2 Properties of hard materials

From a machining point of view "hard materials" are characterized by the following (Nakayama et al., 1988):

a- High indentation resistance

High indentation resistance of the workpiece material requires a cutting tool with higher hardness, usually three times harder than the workpiece material. Also, it causes high stress concentration on the small area of contact between the tool and the workpiece.

b- High abrasiveness

High abrasiveness of the workpiece requires a cutting tool material with a high abrasive resistance.

c- Low ductility

The brittleness of the workpiece material is the main cause of saw toothed chip formation.

d- High ratio of (Hardness/E-modulus)

High ratio of (Hardness/E-modulus) cause a local elastic recovery. Thus, the geometrical error becomes significant in the case of finish machining of hard steel.

2.2.3 Hard turning versus grinding

Figure 2.5 shows the geometrical similarities between hard turning and grinding during the machining of hardened steel. The common high negative rake angle in hard turning produces a compressive stress field similar to that produced in grinding. The possibility of structural change beneath the machined surface exists in both cases. In both machining processes, the tensile residual stresses produced are attributed to the high thermal energy generated during machining. This makes the main source for change in physical properties similar in both cases. Figure 2.6 presents the results of roundness inspections of two workpieces produced by grinding and hard turning. It can be concluded that the turning process gives better results. The question as to whether the properties of hard machining surfaces are comparable to ground ones has not yet been satisfactorily solved (König

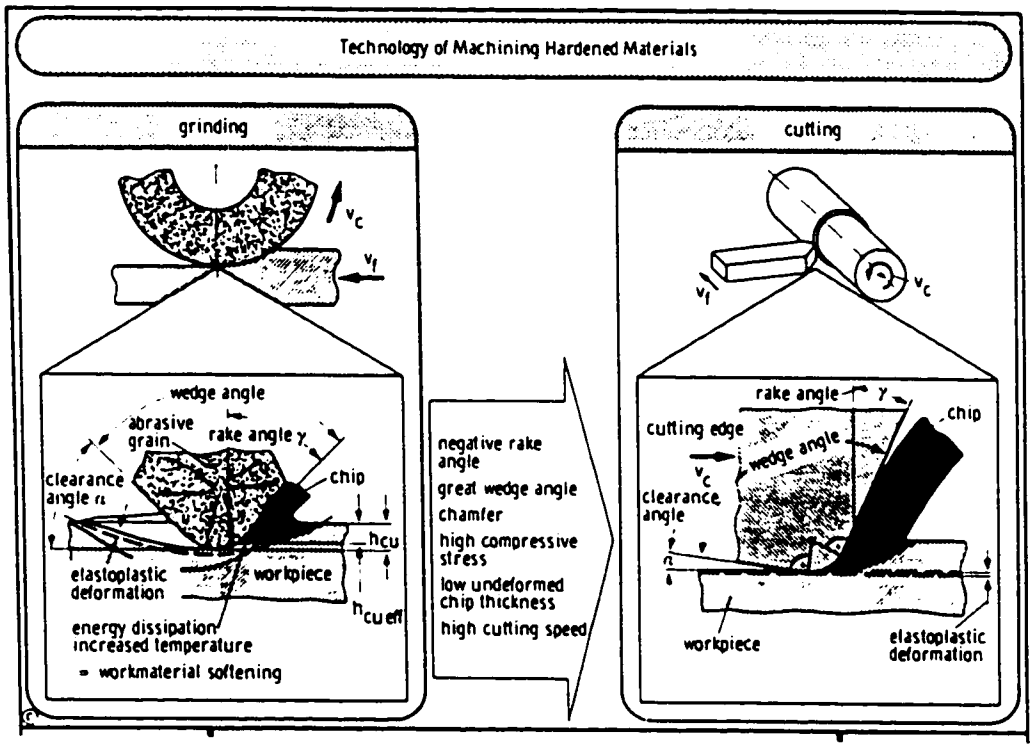

Fig. 2.5 Similarities between grinding and machining with a large negative rake tool (König et al., 1984)

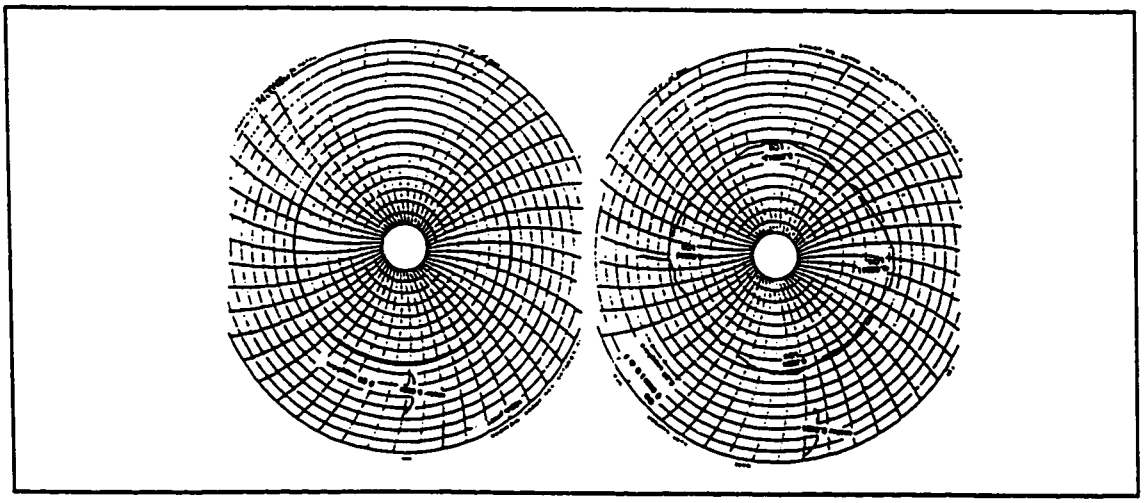

Fig. 2.6 Roundness inspection of ground (left) vs. turned diameter (right) (Buschmohle, 1995)

et al., 1993). There are many aspects of distinction between hard turning and grinding, such as:

a- The contact length between the grinding wheel and the workpiece is several times larger than the contact length between the wear land, source of friction and thermal energy, and the workpiece in hard turning.

b- The average stress over the entire length in grinding is less than that in turning.

c- The compressive stress in hard turning occurs over the entire wear land, but in grinding it occurs in the grain contact area.

d- The penetration depth of residual stress caused by Hertzian stress in the grinding operation is less than that in hard turning.

e- The greater length of contact between the grinding wheel and the workpiece results in a comparatively slow decrease in surface temperature of the workpiece.

2.3 Chip formation

Variety of chips are normally formed during machining. The nature of the chip formation process is extremely complicated. The exact mechanism or combination of mechanisms for chip formation depend upon the metallurgical aspects of the tool-workpiece system and the cutting process parameters. Three main types of chips were early classified, namely, continuous, continuous with built up edges, and discontinuous chips.

Earlier investigations of metal cutting have been focussed on continuous chip formation. According to Lajczok (1980), the first simple model presented for continuous

chip formation in orthogonal machining was presented by Mallock (1882). In this model, it was assumed that the chip is formed by a shearing process along a narrow zone. Merchant (1945) presented chip geometry and the force system in the case of orthogonal machining. The shearing strain undergone by the workpiece material during chip formation, and the shear velocity were among the quantities which were determined. Schematic representation of the shearing process as well as the cutting velocities are shown in Fig. 2.7-a and b, respectively.

The formation of the build up edge is an unstable and transient phenomenon. During the unstable stage, some fragments of built up edge break down and are carried away with the chip. Cyclical formation of a build up edge is shown in Fig. 2.8

Discontinuous chips are formed during dry machining of ductile materials at low cutting speeds where high friction exists between the chip and the cutting tool, or when machining brittle materials, such as cast iron. Field and Merchant (1949) presented a model for discontinuous chip formation. They assumed that the discontinuous chip formation occurs in two stages. However, they did not clarify in their model when the chip segmentation takes place. Cook et al. (1954) observed the process of discontinuous chip formation using a video camera. They concluded that the chips form by an extrusion action in front of the cutting tool, as shown in Fig. 2.9.

Serrated chips are normally formed during rough machining of different materials. It is mainly attributed to the instability of the cutting process within certain ranges of process variables. Komanduri and Brown (1981) classified the mechanisms of serrated chips as:

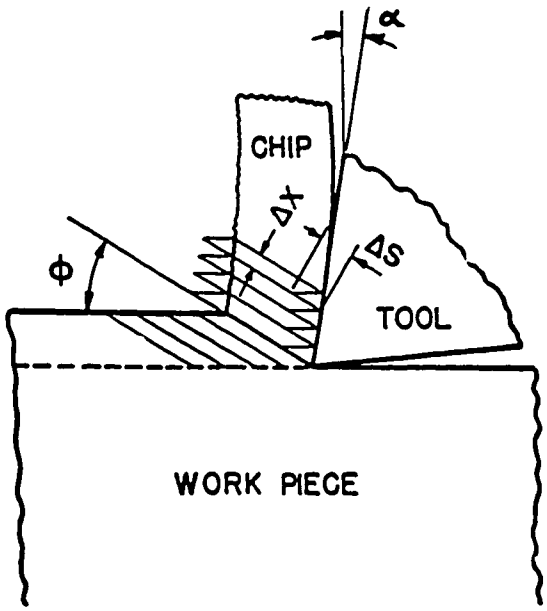

a- Shearing plane in metal cutting

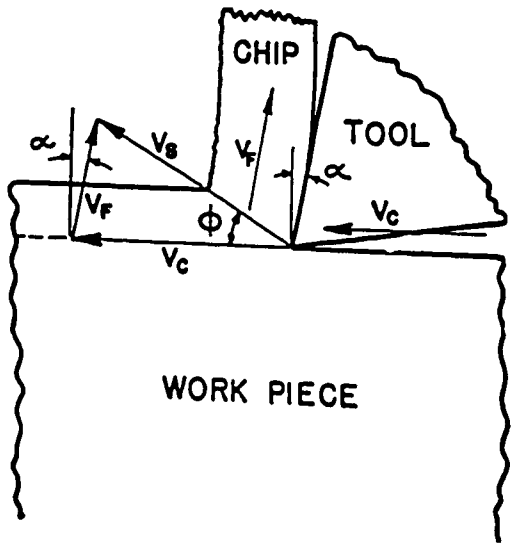

b- Cutting velocities

Fig. 2.7 Shearing process and cutting velocities during machining (Merchant, 1945)

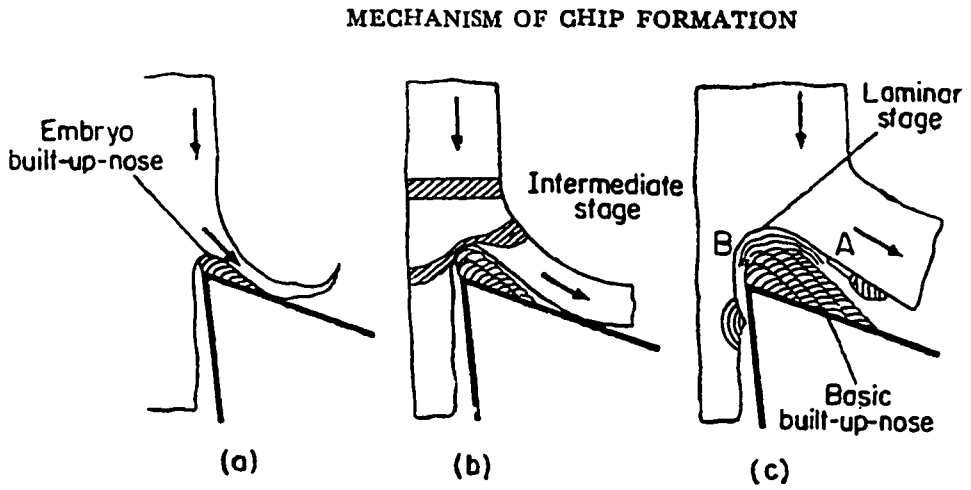

a- Formation of build up edge (Bahttacharyya, 1985)

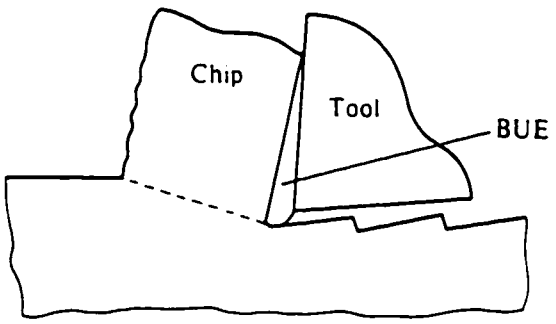

b- Surface roughness due to build up edge (BUE) (Shaw, 1984)

Fig. 2.8 Continuous chip with build up edge

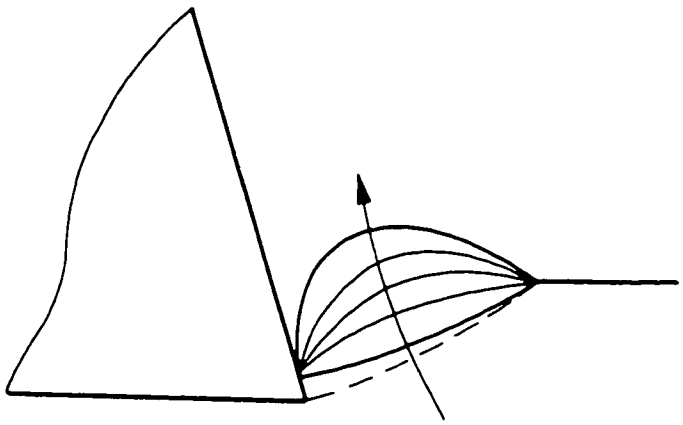

Fig. 2.9 Extrusion of chip into parabolic shape in discontinuous chip formation (Cook et al., 1954)

a- Wavy chip

The wavy chip is symmetrical and resembling a harmonic wave. This type of chip is formed as a results of cyclic variations in the undeformed chip thickness due to regenerative chatter under self excited vibration. This is attributed to the limited rigidity and low damping of the machine tool system.

b- Catastrophic shear chip

This type of chip occurs during the machining of a certain type of materials whose ability to deform plastically varies with the temperature due to phase transformation and consequent changes in their crystal structure. For example, catastrophic chips are normally formed during the machining of titanium alloys which have poor thermal properties. In other materials, catastrophic chips are formed at very high cutting speeds due to plastic instability in the shear zone, leading to catastrophic shear failure along the shear plane.

c- Segmental chip

A segmented chip is a continuous chip with periodic variations in thickness. This type of chip is normally formed in a certain range of speeds and cutting conditions and it depends on the composition and microstructure of the workpiece material. The variation of chip thickness due to regenerative effects cannot effectively account for the variation in segmentation thickness. Although the waviness of this type of chip is symmetrical, the deformation within the chip cross section is not homogeneous.

d- Discontinuous chip

A discontinuous chip is considered a special type of catastrophic shear chip. It is formed due to the periodic rupture along the shear plane. Hence, a complete separation of the chip segments occurs. Details of the nature and mechanism of discontinuous chip formation have been described by Field and Merchant (1949), Cook et al. (1954), and Palmer (1967).

The mechanism of chip formation in hard materials has been studied by several authors (Cook et al., 1954; Recht, 1964; Nakayama, 1974; Komanduri and Brown, 1981; Komanduri et al., 1982; Semiatin and Rao, 1983; Nakayama et al., 1988; Sowerby and Chandrasekaran, 1989; König et al., 1991; Shaw and Vyas, 1993; König et al., 1993). A pioneer work was presented by Recht (1964) which explained the mechanism of cyclical chip formation based on the catastrophic shear instability. According to the presented model, catastrophic shear instability occurs when the local temperature gradients offset the strengthening effect of strain hardening. Based on the similarity between the morphology of the chips generated during machining of 4340 Steel and Titanium alloy, catastrophic shear instability is proposed as the cause for cyclical chip formation when machining AISI 4340 steel at high cutting speed (Komanduri et al., 1982; Semiatin and Rao, 1983). Sowerby and Chandrasekaran (1989) suggested that chip segmentation occurs when steel accumulates a certain amount of damage during the machining operation. Thus, the lower the critical accumulated damage factor, the easier it is for steel to exhibit chip segmentation. Using a

different concept for chip formation, Nakayama (1974) attributed the nature of cyclical chip formation in hardened steel to the lack of ductility of the workpiece material. Nakayama (1974) proposed that the saw toothed chips formed due to shear cracks initiated on the free surface of the workpiece. The initiated cracks are governed by the ductility or the ultimate shear strain of the workpiece material. König et al. (1993) used the same concept to explain the chip formation during hard machining. Recently, Elbestawi et al. (1996) used the concept of surface layer energy and strain energy density to predict the initiation and propagation angle of surface cracks during hard turning. In their approach, the problem was considered to be a mixed mode crack problem of mode I and II. According to the work presented in their paper, the chip formation in hard turning cannot be fully explained based on the shear deformation process only.

2.4 Surface integrity

Studying the surface integrity of the machined part after hard turning gives further information about the physical properties of the machined surface. Changes in the machined surface microstructure during hard turning were observed. The well-known "white layer" is mainly a rehardened layer on the produced surface, which represents a thermally affected zone. By conventional etching, this layer does not show any visible structure. Hence, the layer appears "white" under the microscope. The white layer was observed after certain time of machining, when the tool wear land reached a certain value. This layer is very brittle and easy to crack.

To get more information about the machined surface, residual stresses should be examined. Investigations of the residual stresses in hard turned surfaces reveal favourable compressive residual stresses (König et al., 1993), while the residual stresses in the same workpiece produced by conventional turning operation are frequently tensile. Although a large volume of literature exists on hard turning, the change of the produced surface's physical properties represents the major obstacle of its industrial applications. Thus, to improve the physical properties of the machined surface, a better understanding of the effect of all cutting parameters is needed.

The quality of the surface produced by machining is typically assessed in terms of parameters such as surface texture (e.g., roughness, waviness, material side flow) and dimensional tolerances. For hardened steels, however, the sub-surface damage produced in the machined component affects its resistance to fatigue, creep, and stress corrosion cracking (Bailey et al., 1976). Clearly, it is important to ascertain the integrity of the machined surface, particularly when the components produced are used under severe service conditions such as stress, temperature, and environment.

Surface integrity includes the existence of microcracks, untempered and over tempered martensite, phase transformation, residual stresses imposed by the machining process, the pull-out of carbides from the grain boundary, intergranular attack, plastic deformation, and changes in the microhardness. These factors determine the behaviour and service failures of the components produced. Numerous valuable data and empirical equations on surface integrity including residual stresses have been previously published

(Field et al., 1970; Field and Kahles, 1971; Brinksmeier et al., 1982; Leskovar and Peklenik, 1982). These analyses were performed to investigate the machined surface in soft steel, however, the fundamental relationship between the metal cutting mechanism and surface integrity was not clarified. It is unrealistic to expect that the same results can be applied to the case of hard machining.

2.4.1 Surface and sub-surface deformation

Changes in the surface textures, alterations in the sub-surface microstructure, and microcracking, which are likely to occur when cutting hardened steels, have been investigated by several researchers (Bailey, 1974; Matsumoto et al., 1986; Tonshöff et al., 1995a and b; Chou and Evans, 1996). It has been observed that when flank wear increases to a certain value (V_{Bb} = 0.15 mm), a thermally affected layer appears on the surface produced (Ogata, 1989). It was also observed from the experimental results performed by König et al. (1990) that a microstructural change exists 2-3 μm beneath the surface as the tool wear increases.

Several reports on the integrity and quality of the surface produced by hard machining appear in the literature (Ogata, 1989; König et al., 1990, 1993; El-Wardany et al., 1992, 1993; Tönshoff et al., 1995a, b; Abrão et al., 1995; Chou and Evans, 1996; Bresseler et al., 1997). The existing literature on hard machining is concerned primarily with the understanding of the surface characteristics during the cutting of case hardened or bearing steels used in the automotive industry.

Tönshoff et al.(1995) studied the effect of cutting speed on the integrity of a hard machined surface. Examining the machined surface reveals the existence of a rehardened layer of untempered martensite "white layer". The thickness of the white layer and the tensile residual stress on the machined surface is proportional to the cutting speed. However, the presented results were obtained based on different levels of tool wear where the cutting time was kept constant. By using a constant cutting time, the generated residual stresses are influenced by the tool wear effect where increases in the cutting speed accelerated the tool wear. The white layer was also observed when machining hardened steel using a chamfered cutting tool (Matsumoto et al., 1986). However, conducting the same test using a sharp tool reveals no existence of this layer. Based on this observation, it was concluded that phase transformation is not the source of residual stresses.

Generally, mould and die making involves either an Electron Discharge Machining (EDM) process or a milling operation. Although, the EDM process is independent of the material's hardness and is capable of handling deep moulds and very small radii, metallurgical damage to the surface and sub-surface of the mould is unavoidable. As illustrated by Field and Kahles (1971), the D2 tool steel surface produced by the EDM process suffers from a heat affected layer. The defective surface consists of a recast layer (with or without microcracks), which may extend into the base metal, in addition to metallurgical alterations such as rehardened and tempered layers. Hence, manual polishing of the workpiece is essential to remove these altered surface layers since they significantly lower the fatigue strength of the component.

Recently, high speed hard machining was introduced to the mould and die making industry (Ikeda et al., 1992; Rigby, 1993; Elbestawi et al., 1997). The main objectives of these investigations were to reduce the machining cycle times, reduce the dimensional tolerances, obtain better surface quality, and eliminate the dependency on the availability of skilled hand fitter craftsmen for the post metal removal rework and finishing operations.

Abráo et al. (1995) studied the sub-surface deformation of AISI E52100 hardened steel and H13 tool steel. They observed that the white layer was formed in both types of steels. However, a dark overtempered martensitic layer below the white layer existed only in the AISI E52100 steel. It was concluded that surface and sub-surface alterations are minimal when compared to the published information on grinding.

Several reports on the microhardness and residual stresses distribution, which are induced on the workpiece surface during hard machining, appear in the literature (Field et al., 1970; Bailey et al., 1976; Kono et al., 1980; Matsumoto et al., 1986; Schreiber and Schlicht, 1986; Ogata, 1989; Wu and Matsumoto, 1990; König et al., 1990, 1993; Abráo et al., 1995; Tönshoff et al., 1995a, b; Abráo et al., 1996). Small changes in the microhardness of the workpiece surface produced by hard turning were observed by several investigators (Kono et al., 1980; Ogata, 1989; Tönshoff et al., 1995a). On the other hand, when grinding the same workpiece material, a drop in the hardness near the surface was obtained (Kono et al., 1980). However, these results conflict with those presented by others where the hardness at the workpiece surface was either higher (Tönshoff et al., 1995a; Abrào et al., 1995) or lower (Field et al., 1970) than the hardness beneath the surface, especially with the progress

of tool wear.

2.4.2 Residual stresses

Residual stresses resulting from machining operations involve various input parameters linked together through a multitude of complex internal interactions. They are caused by many sources such as mechanical loads, thermal loads due to the uneven heating and cooling of machined subsurface layers, and phase transformation. In a machining process, the mechanical load induced by cutting forces creates an inhomogeneous plastically deformed layer beneath the machined surface which leads to mechanically induced compressive residual stresses with a definite depth, dependent upon the cutting conditions (Kloos and Kaiser, 1990). In high speed machining, the friction at the tool/workpiece interface introduces additional thermal energy that influences the state of deformation in the machined sub-surface. As a result of the high temperature induced by high speed machining, the yield point of the workpiece material is reduced leading to significant alterations in residual stresses. Rapid cooling of the outer layer of the machined surface produces tensile residual stresses which satisfy the equilibrium conditions with the compressive residual stresses beneath this layer (Matsumoto et al., 1986). Thus, the final distribution of residual stresses is highly dependent upon the amount of mechanical and thermal loads generated during machining.

The behaviour of residual stresses induced in the machined surface and sub-surface region under different conditions was investigated by many researchers. Specifically, the

effect of workpiece hardness, phase transformation, tool wear, types of cutting processes, and cutting conditions on residual stresses were investigated experimentally and analytically by Liu and Barash, (1982); Schreiber and Schlicht, (1986); Wu and Matsumoto, (1990); Tönshoff et al., (1995a) and Abràо and Aspinwall, (1996). The results obtained show that material hardness has a significant effect on the pattern of residual stress that remains in the machined parts (Wu and Matsumoto, 1990).

Matsumoto et al.(1986) studied the effect of material hardness on residual stresses during the machining of AISI 4340 hardened steel. They concluded that the material hardness significantly affects the residual stresses beneath the machined surface. Figure 2.10 shows the effect of material hardness on the residual stress distribution beneath the machined surface. The variation of residual stress patterns in the machined surface was explained mainly by the mechanical deformation where the effect of thermal load was considered to be secondary. Increasing the hardness of a machined component shifts the residual stresses to the compressive side and, hence, improves its fatigue performance.

Mechanical deformation of the workpiece surface was considered to be the cause of producing both tensile and compressive residual stresses in hard machining (Liu and Barash, 1982). On the other hand, the phase transformation of the workpiece structure was discarded as a cause of producing residual stresses during hard machining. Their hypothesis was based on the fact that no phase transformation existed when using a sharp tool with no chamfer. However, tools with chamfer are usually used in hard machining to obtain stronger cutting edges, which indicates that phase transformation is likely to occur. Liu and Barash

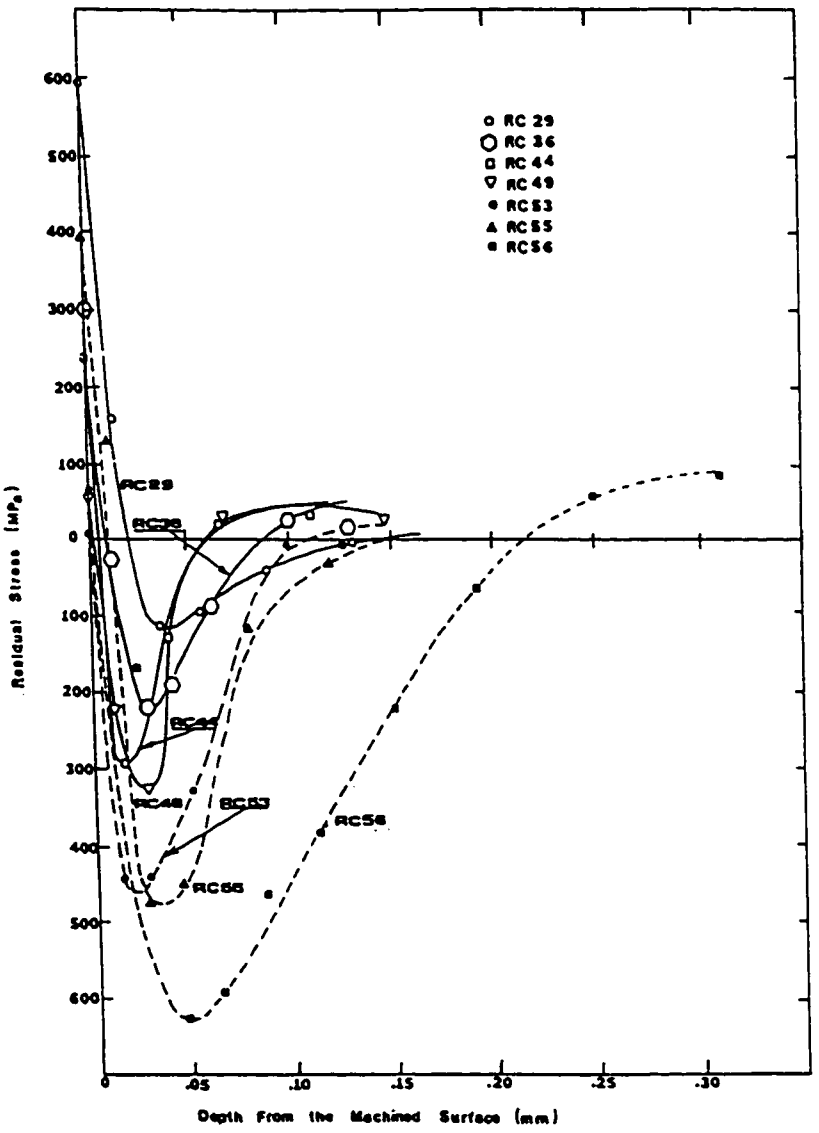

Fig. 2.10 Effect of material hardness on residual stress distribution (Matsumoto et al., 1986)

(1982) reported that cutting with a small depth of cut does not necessarily produce low sub-surface stresses. Therefore, they concluded that from the surface integrity point of view, grinding is not an ideal finishing operation. In addition, since the heat generated during machining is a major source of machined surface damage, Abráo et al. (1995) stated that grinding is a less efficient process than single point cutting where most of the generated heat flows into the chips and not into the workpiece.

Only a few attempts were made to investigate the effect of cutting speed, feed rate, depth of cut, tool geometry and the use of lubricant on the residual stresses generated during hard machining(Okushima and Kakino, 1971; Schreiber and Schlicht, 1986; Tönshoff, et al., 1995a). Kono et al. (1980) reported that the residual stress level on the surface layer generated by hard turning shows remarkable changes depending upon cutting conditions. It increases with the cutting speed, but does not change with the depth of cut. These results contradict those obtained when machining soft steel, where increasing the depth of cut increases the residual stresses induced on the surface (El-Khabeery and Fatouh, 1989).

Sadat and Bailey (1987) studied the effect of feed rate on residual stresses. They concluded that the effect of feed rate on residual stresses is complex where at low cutting speed an increase in feed rate results in an increase in the magnitude of tensile residual stress. However, at high cutting speed an increase in feed produces a compressive residual stress. Sadat (1990) stated that the machined surface quality improved significantly when the cutting speed was increased. However, prolonged use of the cutting edge at high speed machining leads to severe damage due to rapid tool wear. The effect of cutting speed on residual

stresses during machining of hardened steel was investigated by Schreiber and Schlicht (1986). It has been shown that when turning 100Cr6 steel, an increase in cutting speed increases the magnitude of tensile residual stress on the machined surface. On the contrary, when machining 42CrMo4 steel, an increase in the cutting speed alters the tensile residual stress on the machined surface to compressive stress. This observation reveals the complexity of the nature of residual stresses and its dependence upon the workpiece material.

The effect of various cutting speeds during the machining of case hardened steel was investigated by Tönshoff et al. (1995a). The results presented in this study were obtained at a fixed time of seven minutes. Various cutting speeds were employed ranging from 40 m/min to 315 m/min. By fixing the cutting time, the residual stresses were influenced by both the cutting speed and the tool wear magnitude, since increasing the cutting speed will accelerate the tool wear. In the same investigation (Tönshoff et al. 1995a) and that of König et al. (1993), it was shown that the residual stresses are almost doubled when the tool wear is 0.2 mm (cutting with a worn tool results in a thicker stressed surface layer, and higher tensile residual stress at the outer surface). Hence, the effect of cutting speed on the magnitude and distribution of the residual stresses cannot be justified with these results. In general, increasing the cutting speed will increase the residual stresses due to the high thermal load generated. Since the yield strength of the sub-surface layers will be reduced with the increase in the cutting temperature, plastic deformation will increase and affect the residual stress pattern obtained by the mechanical loading. The results obtained by Schreiber and Schicht (1986) confirmed that the mechanical properties of the machined

material have a great influence on the magnitude and distribution of the residual stresses.

Few analytical studies were performed to predict the residual stresses during hard machining. In general, the mechanics of the cutting process have been extensively examined using two fundamental approaches: minimum energy principle (Palmer and Oxley, 1959) and slip line field theory (Lee and Shaffer, 1951). The development of the minimum energy principle approach has been well summarized by Shaw (1984). It establishes the shear angle concept and the relation between forces and velocities during machining. However, this approach necessitates the simplification of material deformation behaviour and relies explicitly on experiments.

Barash and Schoech (1970) predicted the residual stresses in the sub-surface layers of the produced workpiece by using slip line field. The variation of the yield stress which extended below the machined surface is considered in their model to account for the depth of the deformed layer. In this investigation, it was found that the shear plane (instead of the ploughing force or anything else) is the major cause of the surface and sub-surface deformation. In spite of the advances in the slip line field model, some empirical constants in the model have to be obtained by examining the chip sections from "quick stop" specimens.

A quantitative approach has been used by Wu and Matsumoto (1990) to study the effect of workpiece hardness on the pattern of residual stresses induced in the workpiece surface. In this study, it was found that the combined effect of the workpiece hardness, the shear angle, the cutting temperature, the yield strength, and the average stress ratio in the

primary deformation zone determine the behaviour of the residual stresses. The results show a trend of agreement with the experimental data; however, there was no actual prediction for the residual stresses under different cutting conditions.

2.5 Applications of the finite element technique in machining

Continuum mechanics problems have infinite degrees of freedom and complicated boundary conditions and are very difficult to be analysed mathematically. The finite element method is one of the numerical methods available which discretize a system into a finite number of degrees of freedom. It is a powerful tool and has been successfully used in the machining area.

The finite element method was used by different investigators to predict the residual stresses. Lajczok (1980) developed a simplified model of orthogonal cutting . In his study, the geometry and tool forces were measured experimentally, and then applied to the workpiece surface while neglecting the chip. The plastic deformation zone and residual stress pattern below the workpiece surface were calculated and were then shown to compare favourably with experimental results. A similar model was used by Natarajan and Jeelani (1983) to determine residual stresses in the workpiece. They used a visco-plastic model, which allowed strain rates to be computed. In addition, they included the effect of cutting temperature in their model. Again, the tool load was simulated by moving the point load along the workpiece surface. No experimental verification was presented.

The ploughing forces and the temperature distribution were considered as the main

causes of residual stresses by Okushima and Kakina (1971). However, the calculated results did not quite agree with the experimental results. A detailed review of the finite element simulation of orthogonal cutting has been conducted by Wang et al. (1988). They concluded that the numerical simulation of metal cutting processes requires proper modelling of material properties.

More advanced finite element models of orthogonal cutting have been reported by others (Liu and Lin, 1985; Mishra and Prasad, 1985; Lin et al., 1991; Shih and Yang, 1993; Shih, 1995). Some of the special features of these models, such as the formulation method, state of the simulation, chip separation, modelling of material behaviour, temperature effects, chip-tool interaction, and experimental comparison have been summarized by Zhang and Bagchi (1994). Most recently, the elastic-visco-plastic and thermal finite element formulations were proposed by Shih (1993). In these cases, orthogonal cutting using a sharp tool was assumed to predict the residual stresses, and the predicted results were in agreement with the experimental verification. The effect of tool wear on the residual stresses cannot be ignored, since the experimental results obtained earlier by König et al. (1993) indicate that the worn tool tip had a great influence on the type, magnitude, and distribution of residual stresses.

Most of the above mentioned studies dealt with soft steel. For hardened materials and/or high cutting speed, which is the case of the present study, the "saw toothed" chip formation process is predominant and considered worthy of further investigation. Very recently, a finite element modelling procedure was developed to establish the analytical

methods needed for predicting discontinuous chips and it was applied to the serrated chip formation during orthogonal cutting of a titanium alloy (Obikawa and Usui, 1996). In orthogonal cutting, it is assumed that the chip is produced in a nearly plane-strain condition, since the width of cut is at least five times larger than the depth of cut. This assumption cannot be applied in the case of bar turning of hardened steel because the usual ratio between the width of cut to the chip thickness does not exceed 2 to 3. Hence, using a two dimensional analysis model for determining the residual stresses in hard machining can produce inaccurate results. Also, the high cutting temperature, usually generated during dry hard machining, will affect the pattern of the residual stresses distribution. A proper finite element model in hard turning should predict the temperature distribution during cutting along the workpiece surface and sub-surface.

CHAPTER 3

CHIP FORMATION

3.1 Introduction

Segmented chips are formed through a variety of mechanisms and can be categorized into four types: the wavy chip, the catastrophic shear chip, the segmented chip, and the discontinuous chip (Komanduri and Brown, 1981). In addition, the saw toothed chips are normally formed and represent an essential feature of hard turning. This type of chip is defined as a continuous chip with a periodic variation in thickness. This feature is desirable from the viewpoint of chip disposal but it is the source of cutting force fluctuations that represent a high dynamic load on the cutting tool. The study of chip formation is important since it affects the thermal and mechanical loads that alter the surface integrity of the machined surface. It is also useful for cutting force prediction. Moreover, since trailing

edge wear is typically attributed to chip edge serration (Tönshoff and Bartsch, 1988; Hogson and Trendler, 1981), an understanding of chip morphology is essential for tool wear studies.

In this chapter, a mechanistic model is presented to explain the mechanism of saw toothed chip formation. In addition, an attempt is made to clarify the effect of cutting parameters on chip morphology during hard turning. Different cutting tool configurations including sharp, honed, and chamfered cutting edges with different angles of approach and nose radii are utilized. The effect of the cutting tool wear on the chip morphology is also studied.

3.2 Experimental procedure

Dry hard turning tests have been conducted in order to study the chip morphology during machining of hardened steel. In this investigation, both orthogonal and oblique cutting conditions were utilized. The machining tests were performed on a 10 HP CNC lathe machine. Bars of AISI 1550 steel (58-60 Rc) with a case hardened layer of 4 mm, 25 mm diameter, and 200 mm length were used for oblique cutting tests. Orthogonal cutting tests were performed on tubes made from the same material and having 25 mm outside diameter, 4 mm wall thickness. All cutting tests were conducted using TNG (70 % Al_2O_3, 30% TiC) ceramic indexable tips with zero degree clearance angle. Three different nose radii 1.2, 2.4, and 3.6 mm and both honed and chamfered tools were utilized to study the effect of the nose radius and cutting tool conditions on the chips produced. Two different angles of approach 0 and 30 degrees, and -6 degree rake angle were used in this investigation. The cutting

speeds and feeds varied over a range of (90-200) m/min and (0.01-0.2) mm/rev, respectively. The cutting forces were measured using a piezoelectric dynamometer. Since the chip segmentation occurs at high frequency, a high sampling frequency (27 KHz) was used by the data acquisition system in order to track chip segmentation in the force signal. All cutting tests were carried out such that the cutting time was as short as possible in order to eliminate the effect of tool wear. On the other hand, the cutting time was sufficient to ensure steady state conditions. Before each cutting test, the cutting tool edge condition was examined using a tool maker's microscope.

During the experiments, chips were collected at different cutting conditions. The chips collected were mounted in cold epoxy mount containing aluminum oxide filler to retain the chip edge roundness during further processing. The chips mounted were ground, polished, and etched using a 2 % nital solution. The cross sections of the mounted chips were examined using an optical microscope at magnification of 100X to 1000X. Scanning Electron Microscope (SEM) was also employed to examine the chips collected. No chip preparations were performed on the chips examined by SEM to avoid introducing any deformation.

Microhardness tests were also carried out using a Buehler microhardness tester to determine the effect of cutting parameters on the microhardness of the chips cross sections. Chips were collected randomly at different cutting conditions, then mounted, ground and polished for examination using the microhardness tester. Because of compression stress in and around an indentation, any new indentation made near another could cause inaccurate

results. Thus, a separation distance between indentations of four times that of the diagonal was used. Also, a distance of at least 2.5 times the distance of the diagonal is maintained between the indentation and the edge of the sample. In addition, any indentation which was made and did not appear to be within the required distance from another impression or the edge of the specimen was excluded from the test. To ensure the repeatability of the results obtained, the microhardness tests were repeated on chips collected after the same cutting conditions. The variations in microhardness were used to map out different deformation zones through the chip cross section. Also, the effect of different combinations of cutting speeds and feeds were investigated.

3.3 Mechanistic model for chip formation

Hardened steels are sensitive to their surface topography during machining. The surface of the machined workpiece includes microscopic ridges and cracks. Figure 3.1 represents a general configuration of chip formation during hard turning. When the cutting tool advances it generates a compressive stress field in front of it. The compressive stress in front of cutting tool leads to a crack initiation at the free surface owing to material brittleness (Elbestawi et al., 1996 and König et al., 1993). The irregularities of the free surface play a major role in crack initiation. With further advancement of the cutting tool, the initiated crack propagates towards the cutting edge. However, it ceases before reaching the cutting edge where severe plastic deformation exists due to the high compressive strain field and temperature in the vicinity of the cutting edge. The aforementioned crack serves

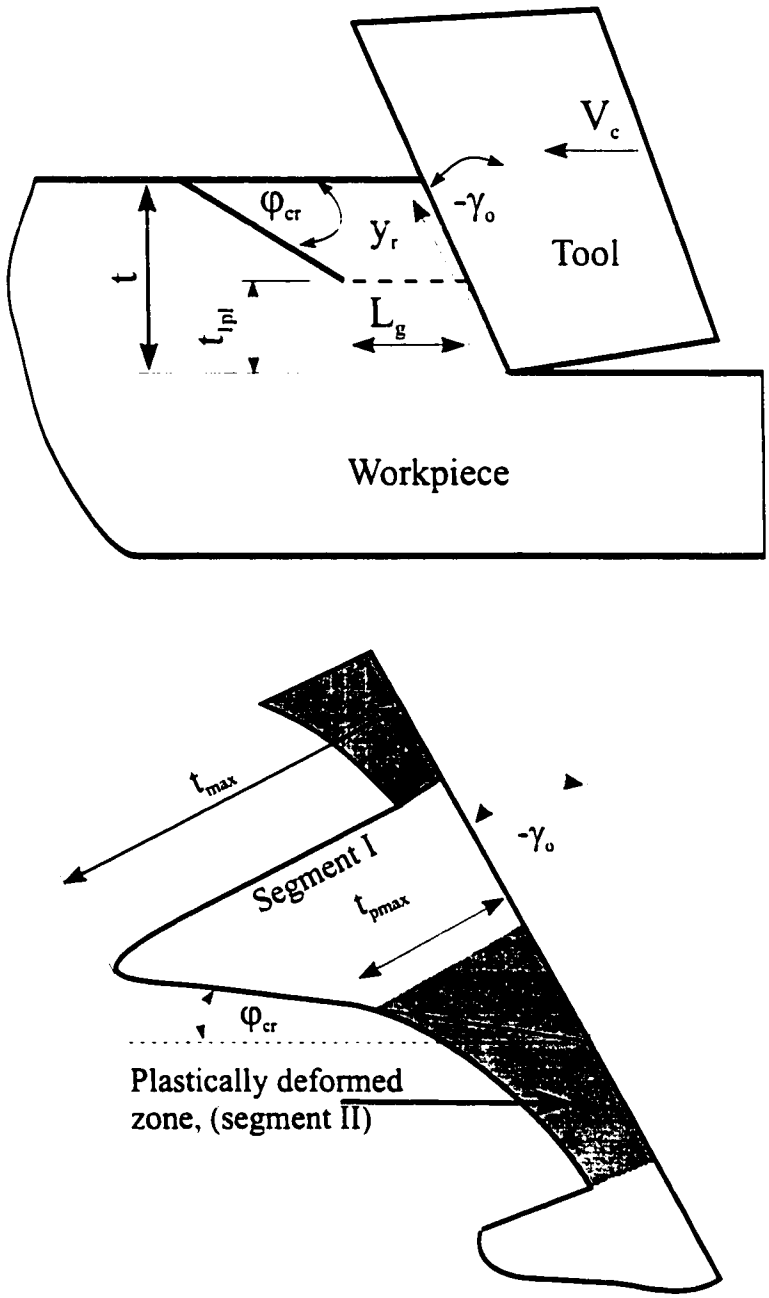

Fig. 3.1 Schematic diagram for chip formation in hard turning

as a sliding plane for the fractured material segment (segment I) which is caught up between the tool rake face and the crack. With further advance of the cutting tool, the plastically deformed region in the chip (segment II) is extruded through the gap between the tool rake face and the crack base.

3.3.1 Kinematics of chip formation

In order to analyse the chip formation, it is convenient to consider the chip as consisting of two segments. Segment I is the chip segment that is caught up between the tool rake face and the crack. Segment II is the plastically deformed region of the chip which is just below the base of the crack. During the chip formation, it is assumed that segment I is pushed up parallel to the tool rake face without deformation, while segment II is extruded through the gap between the tool rake face and the crack base. Let t and t_{lpl} be the undeformed chip thickness and the length of the plastically deformed zone respectively. The extrusion of the plastically deformed material through the gap can be expressed in the following differential form:

$$\frac{dt_{pl}}{dy_r} = - \frac{\cos(-\gamma_o)}{t_{lpl}} t_{pl} \qquad (3.1)$$

at time $t = 0$, $y_r = 0$ and $t_{max} = t_{lpl} \cos(\gamma_o - \varphi_{cr})/\sin(\varphi_{cr})$, where y_r is the travelling distance of the chip along the rake face and t_{pmax} is the maximum plastically deformed chip thickness. By solving the differential equation (3.1) using the initial condition the contour of the

plastically deformed segment is given by:

$$t_{pl} = \frac{t_{1pl}\cos(\gamma_o - \varphi_{cr})}{\sin(\varphi_{cr})}\, e^{\left(\frac{-\cos(-\gamma_o)}{t_{1pl}} y_r\right)} \tag{3.2}$$

where φ_{cr} represents the crack propagation angle. The initial gap length L_g is given by : $L_g = t_{pmax} / \cos(\gamma_o)$. From the geometrical relations and by using the initial condition at time t = 0, the initial gap length is given by:

$$L_g = t_{1pl}\left[\frac{\cos(\gamma_o - \varphi_{cr})}{\sin(\varphi_{cr})\cos(-\gamma_o)}\right] \tag{3.3}$$

Using equations (3.2) and (3.3), the displacement of the chip along the tool rake face is given by:

$$y_r = \frac{t_{1pl}}{\cos(-\gamma_o)} \ln\left(\frac{L}{L_g}\right) \tag{3.4}$$

The velocity of the plastically deformed material along the tool rake face is given by:

$$V_p = \frac{dy_r}{dt} = \frac{t_{1pl}}{[L_o - V_c t]\cos(-\gamma_o)} V_c \tag{3.5}$$

As the chip starts to move parallel to the rake face, the velocities of the two chip segments

are the same. Thus, at time t = 0 the chip velocity is given by:

$$V_P = V_R = \frac{t_{1pl}}{L_g \cos(-\gamma)} V_c \qquad (3.6)$$

where V_R and V_P are the velocities of segment I and segment II, respectively. According to the above mentioned chip formation theory, the maximum deformed chip thickness (t_{max}) decreases linearly to the maximum plastically deformed chip (t_{pmax}). In the plastically deformed segment of the chip, the plastically deformed chip thickness t_{pl} decreases exponentially according to equation (3.2). The deformed chip thickness (t_{pl}) eventually approaches zero, resulting in discontinuous chip segments. However, in reality, another crack develops just before the gap between the rake face and the crack base is closed. Thus, the chip segments that are formed become connected and the saw tooth shape is created.

3.3.2 Plastic deformation zone

The workpiece material in the plastically deformed zone (segment II) is subjected to a high compressive stress such that the material exceeds the elastic limits and plastic flow occurs. The plastic deformation is facilitated by the high temperature generated during machining. It has been shown that the equivalent stress in the cutting zone correlates to the equivalent stress obtained from a material test at the same strain rate (Lapsley et al., 1950). The correlation between the static material properties and the dynamic behaviour in machining is good in spite of extreme differences in strain rate and temperature (Park et

al., 1993). In fact, the effect of thermal softening induced by a temperature rise in the cutting zone is offset by the high strain rate (Thomsen, 1966).

In order to locate the point at which the crack ceases, it is assumed that:

a- The boundary of plastic deformation is represented by an arc with a radius (r). This assumption is based on the estimated shape of the plastic deformation zone ahead of the cutting tool as shown in Fig. 3.2 (Usui, E. and Shirakashi, T., 1984). In addition, a negative rake angle is normally used to reduce chipping of the cutting tool in hard turning. Thus, it is expected that the plastic deformation is mainly located ahead of the cutting tool.

b- For simplicity, it is assumed that the plastic strain inside the plastically deformed zone varies linearly. It starts with a minimum value of plastic strain at the contour of the plastic zone and increased linearly towards the cutting edge.

c- The total specific cutting energy is dissipated in the cutting zone where the plastifiction occurs. Thus the total specific cutting energy (E_s) is equal to the total specific energy consumed by plastic deformation.

In a compression true stress strain curve, the total specific energy consumed by plastic deformation can be represented by the area under the curve bounded by the strain value at the elastic-plastic boundary (ε_e) and the maximum plastic strain (ε_m). It has been shown that in a machining process, the plastic deformation initiates at ε_e, which experiences about 0.2% of true strain (Black, 1979). The total specific energy consumed by plastic deformation in machining is equivalent to the area under the above mentioned stress strain

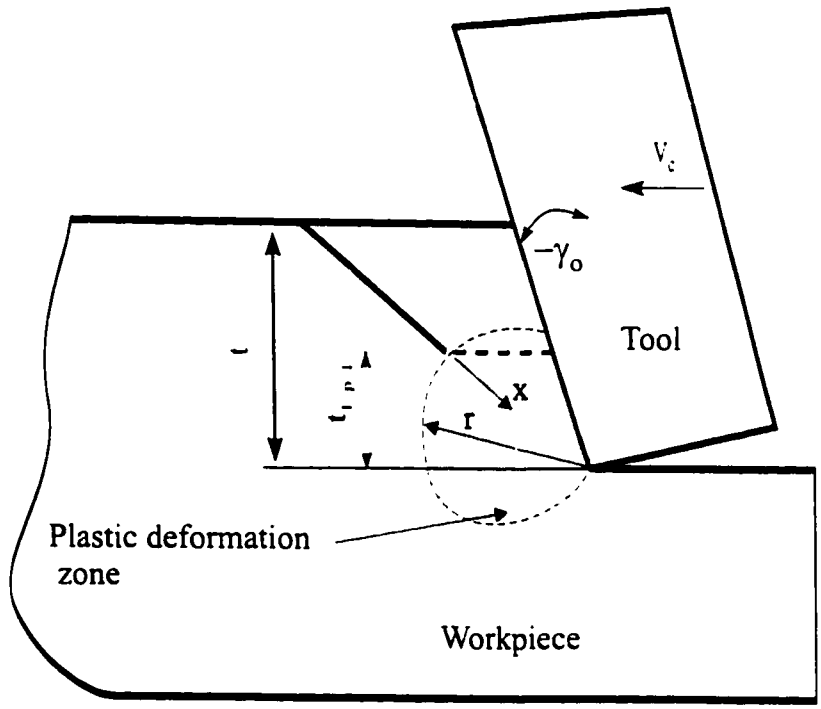

Fig. 3.2 Plastic deformation zone during the chip formation

curve bounded by the strains of ε_e and ε_m (Park et al., 1993).

Thus, the total specific cutting energy is given by:

$$E_s = \int_{\varepsilon_e}^{\varepsilon_m} \sigma \, d\varepsilon \tag{3.7}$$

Different empirical equations have been proposed and used successfully to describe the plastic behaviour of material under different strain rates and temperatures. Johnson and Cook (Meyers, 1994) suggested the following empirical equation:

$$\sigma = (\sigma_o + B\varepsilon^n)\,(1 + C\ln\frac{\dot{\varepsilon}}{\dot{\varepsilon}_o})\,[1 - (T^*)^m] \tag{3.8}$$

It is assumed that the plastic strain distribution has a linear relationship given by:

$$\varepsilon = Ax + B \tag{3.9}$$

where A and B are constants and x is the distance measured from the elastic-plastic boundary to the cutting tip. Given the boundary conditions

$$at \;\; x = 0 \qquad \varepsilon = \varepsilon_e \qquad ; \qquad at \;\; x = r \qquad \varepsilon = \varepsilon_m$$

solving equation (3.7) using the proposed constitutive equation and the available boundary conditions yields that:

$$E_s = (A\ \sigma_o + \frac{B}{n+1}((Ar+\varepsilon_e)^{n+1} - \varepsilon_e^{n+1}))C_1C_2 \qquad (3.10)$$

where C_1 and C_2 are the strain hardening and temperature effect terms in the Johnson-Cook equation.

The depth of plastic deformation (t_{1pl}) is calculated by solving equation (3.10). A combination of geometrical relations of the chip formation in Fig. 3.1, as well as numerical iterations techniques are employed in arriving at this solution. The value of the constant A is obtained by calibrating the measured values and calculated values of the ratio R_{max} (Elbestawi et al, 1996). R_{max} is defined as the ratio between the maximum plastically deformed thickness of the chip, in the plastic deformation zone, to the maximum thickness of the chip. A comparison of the measured and predicted values of R_{max} is shown in Fig. 3.3. By using the proposed model, the effect of the cutting temperature on the depth of plastic deformation is obtained. Fig. 3.4 depicts the effect of the cutting temperature on the size of the plastic zone. One can conclude that an increase in the cutting temperature has a direct effect on the plastic deformation. This can be attributed to the thermal softening effect of the cutting temperature.

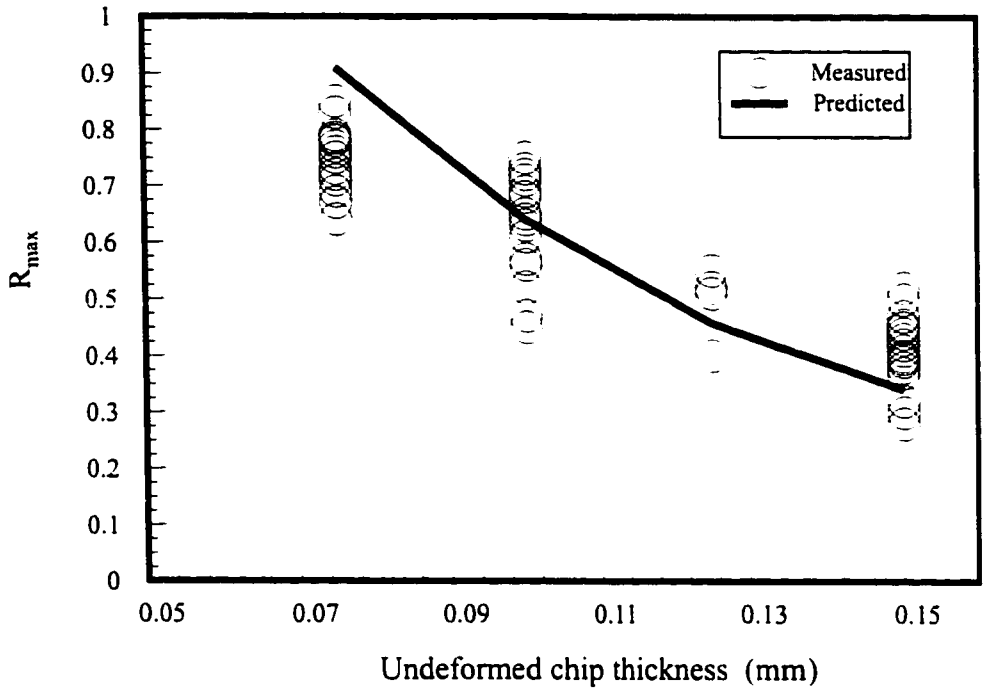

Fig. 3.3 Measured and predicted values of R max

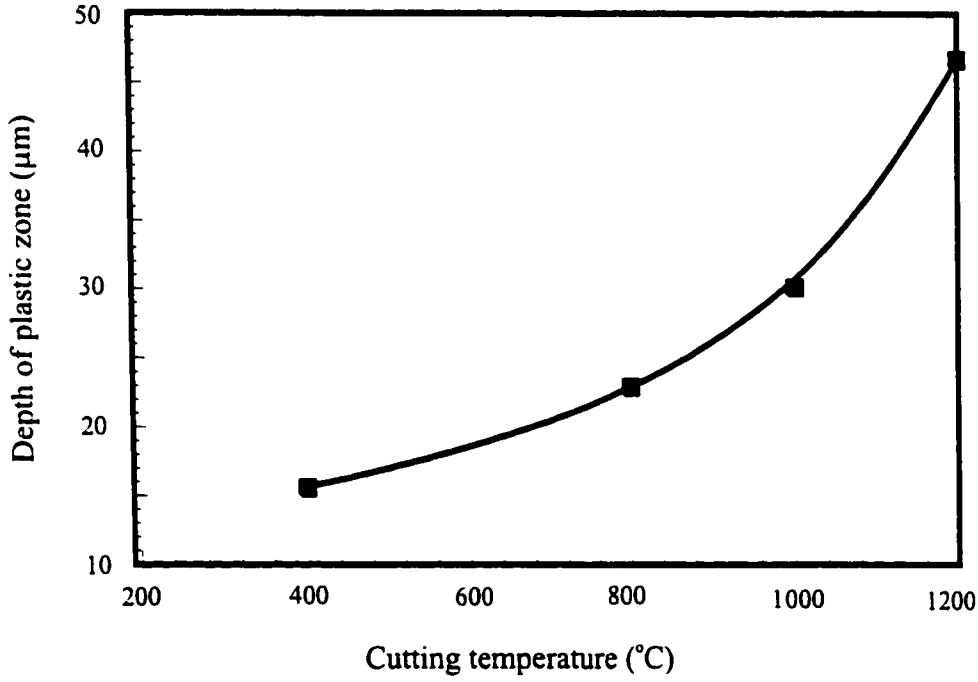

Fig 3.4 Effect of cutting temperature on the deformation zone

3.4 Chip morphology

Figure 3.5 shows an optical microscope image of a saw toothed chip produced during hard turning at 160 m/min cutting speed, 0.15 mm/rev feed, 4 mm depth of cut and -6 degree rake angle. The saw toothed chips were observed during all the cutting conditions used in this investigation. Two different deformation zones are observed through the saw tooth cross section. There is no evidence of plastic deformation in the fractured segment of the chip (segment I). However, severe plastic deformation is observed in segment II. Segment I has the same tempered martensitic structure of the non-deformed basic material, while segment II represents a heavy plastic flow with a fine grain structure.

Figure 3.6 shows a SEM image of the tool/chip interface for the chip edge. Examining the SEM image reveals the existence of chip material side flow. It can be seen that the direction of material flow is perpendicular to the chip velocity. This observation can be attributed to a heavy plastic deformation at the tool/chip interface. Therefore, the plastically deformed material flows at the free edge of the chip. This causes chip side-curling (Nakayama and Arai, 1992). Cutting using a larger angle of approach decreases the material side flow and, hence, eliminates the chip side curling.

3.5 Dynamics of chip formation

Although cutting forces in hard turning are not necessarily high, the periodic chip formation subjects the cutting tool edge to a high dynamic load. The main source of dynamic

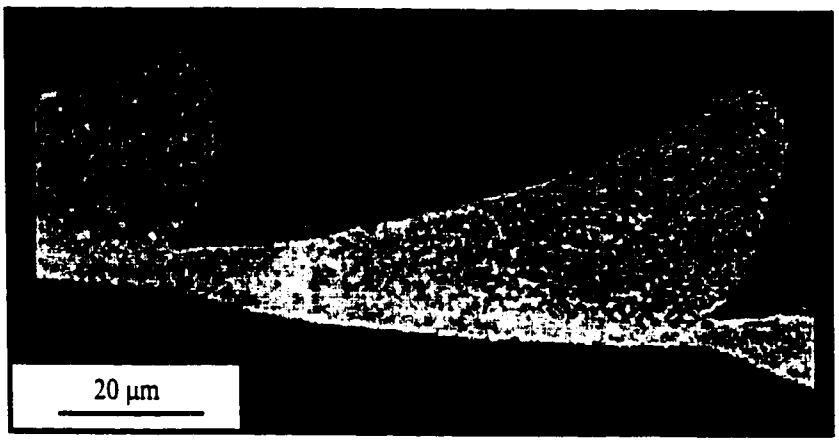

Fig. 3.5 Optical microscopic image showing the structure of saw toothed chip (V = 160 m/min, f = 0.15 mm/rev, d = 4 mm)

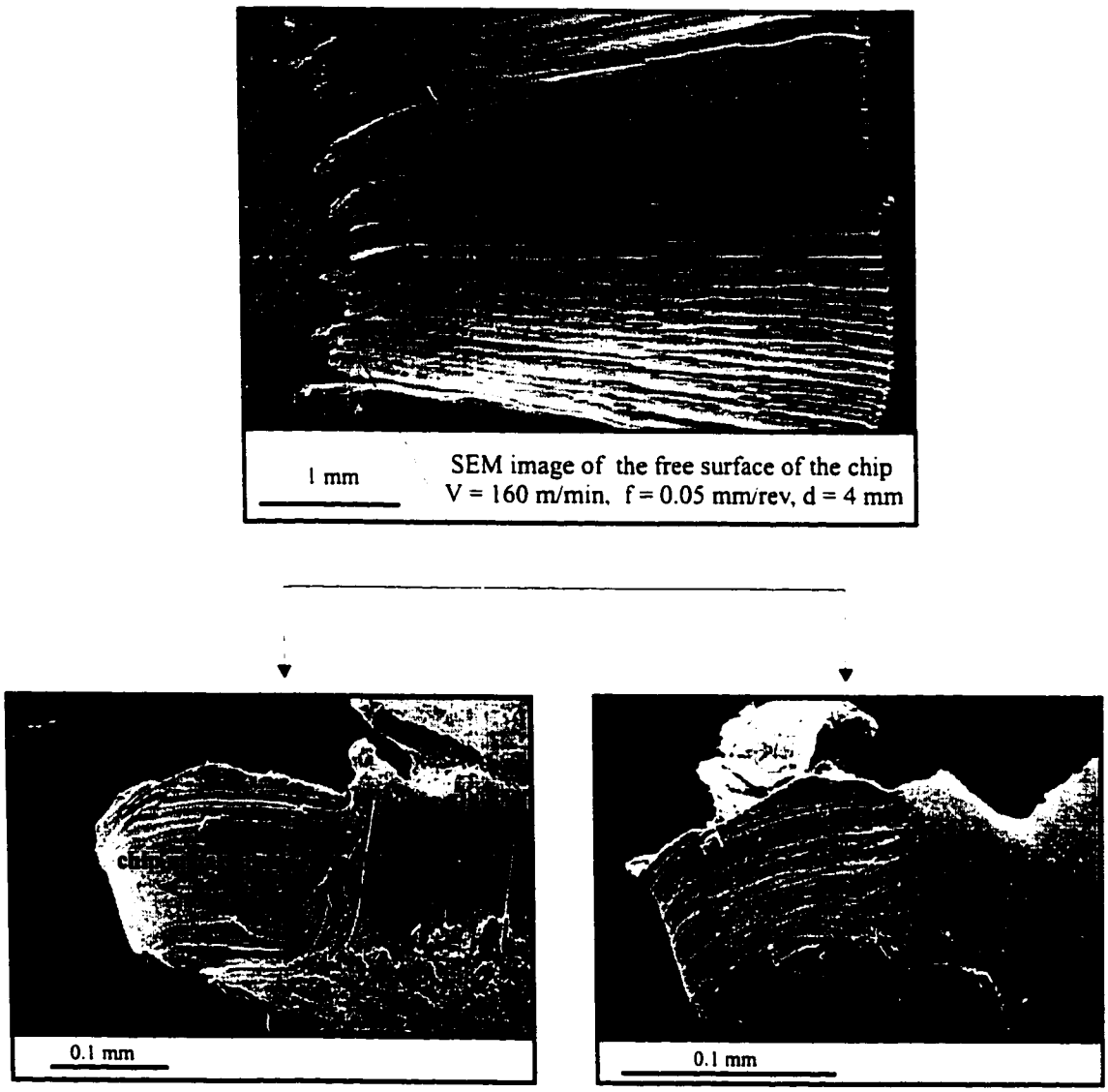

Fig. 3.6 SEM images showing the chip material side flow

load during the chip formation is the chip segmentation. Figure 3.7 shows the dependancy of segmentation distance on undeformed chip thickness. The results obtained seem to be consistent at different values of the cutting speed. The trend of the data plotted is similar to those obtained by Davies et al. (1996). Figure 3.8 shows the effect of the cutting speed on segmentation distance. The general trend of the data suggests that the segmentation distance decreases at higher cutting speeds. The data presented in Fig. 3.8 are consistent with those obtained by Lindberg and Lindstörm (1983). Figure 3.9 shows optical microscope images of chip cross sections obtained at different feeds and cutting speeds. To ensure the reliability of the results presented in Fig. 3.7 and Fig. 3.8, the tests have been repeated on several randomly selected chips.

By using the average values of the segmentation distance, the average chip segmentation frequency is calculated.

$$f_{crack} = \frac{V}{\lambda_c} \tag{3.11}$$

where V is the cutting speed and λ_c is the average value of the crack toothed spacing measured from the chips (Lindberg and Lindstörm, 1983). The frequency values obtained are highly dependant on both the cutting speed and the undeformed chip thickness, as shown in Fig. 3.10. At a high value of undeformed chip thickness, the curve appears to flatten out. At a low undeformed chip thickness, the frequency of the chip segmentation increases exponentially. This observation is consistent with the results reported by König et al. (1993).

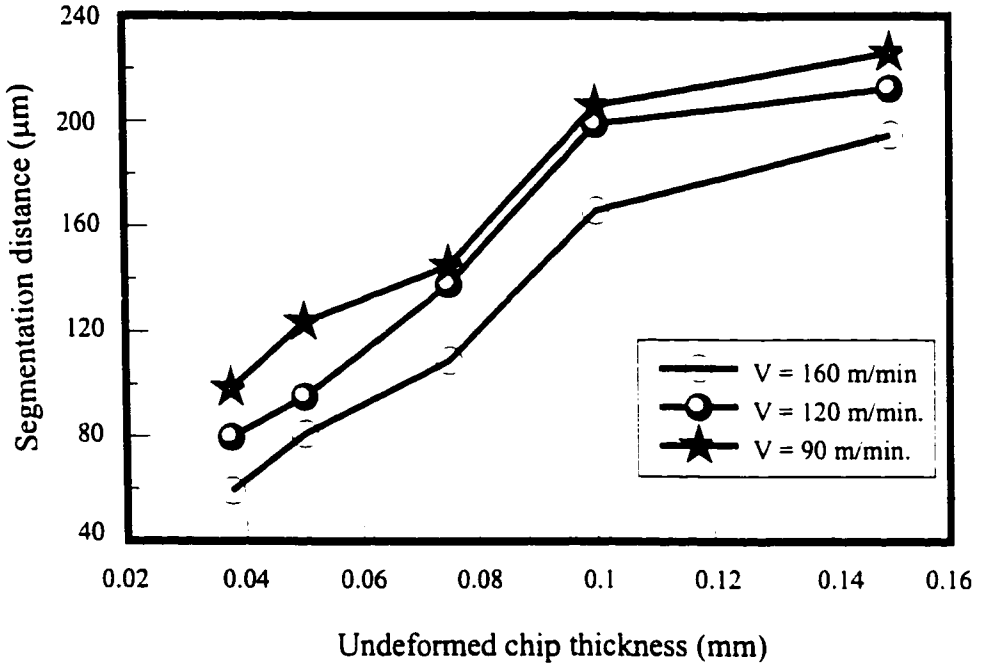

Fig. 3.7 Effect of undeformed chip thickness on segmentation distance

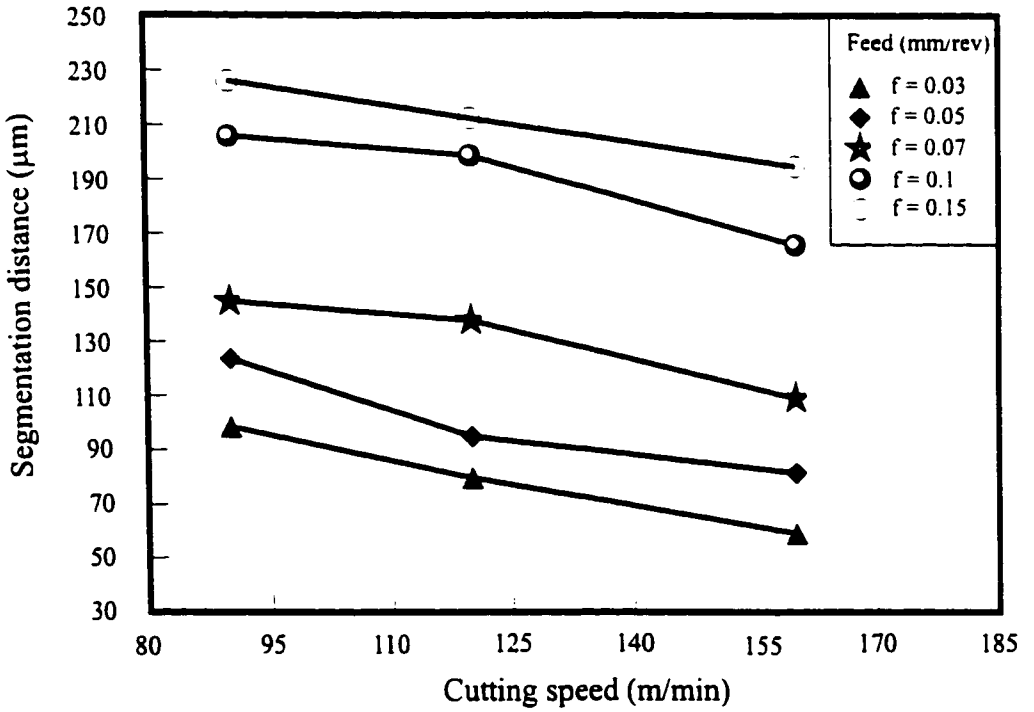

Fig. 3.8 Effect of cutting speed on segmentation distance

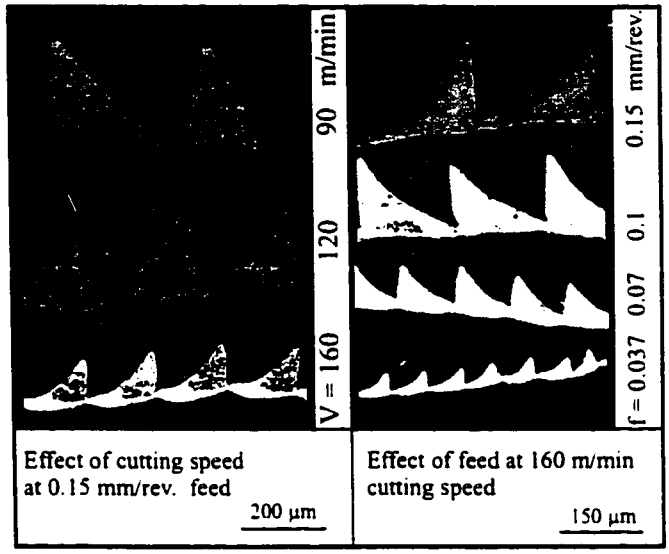

Fig. 3.9 Effect of different cutting parameters on the chip formation

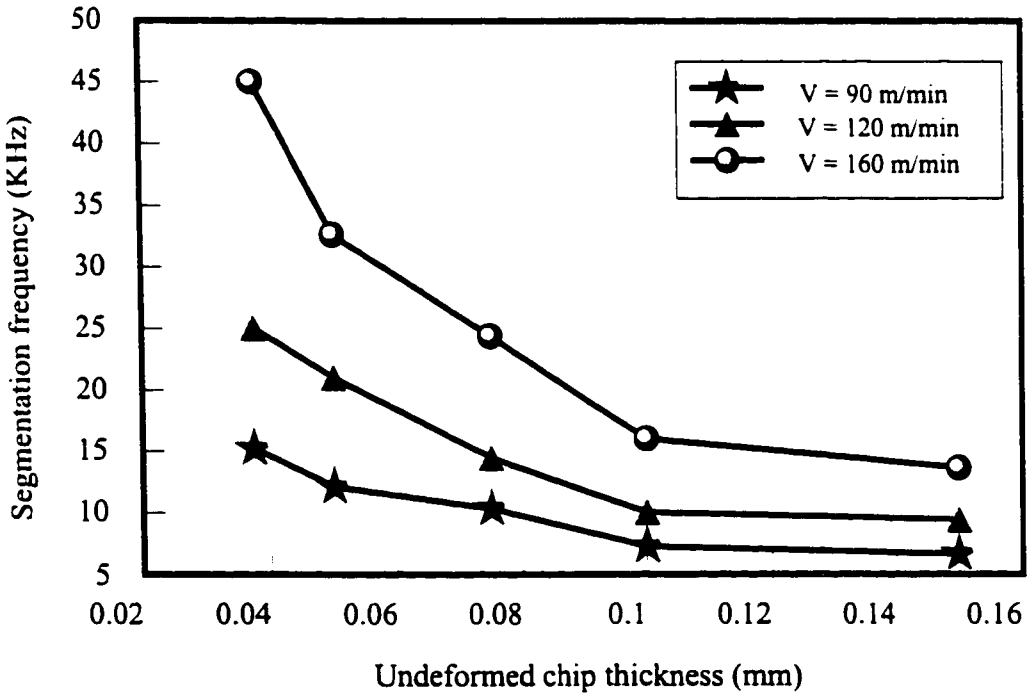

Fig. 3.10 Effect of undeformed chip thickness on segmentation frequency

Increasing the chip segmentation frequency results in the chip cross section being similar to that of a continuous chip, especially at high cutting speeds and low feeds. Meanwhile, the results obtained are in agreement with the fact that the fracture angle is almost constant regardless of the cutting conditions (Elbestawi et al., 1996). From the geometry in Fig. 3.1, one can realize that with a constant fracture angle increasing the undeformed chip thickness increases the chip segmentation distance, as shown in Fig. 3.7. Figure 3.11 is a typical force signal measured during hard turning at 90 m/min cutting speed and 0.075 mm/rev feed. The cutting speed was selected small enough so that the chip segmentation frequency could be recorded using the available data acquisition system. The FFT analysis of the recorded signal shows a peak at approximately 9300 Hz. Such a high frequency is not related to the mechanical components of the cutting system. In fact, the fluctuation frequency obtained from the cutting force is in agreement with the frequency data calculated from the average chip segmentation distance as shown in Fig. 3.11. Other small peaks in the power spectrum can be attributed to the fact that the chip segmentation distance is not constant but varies in a certain limits. Nevertheless, the mean value of the chip segmentation frequency is almost identical to the force fluctuation frequency. Therefore, the fluctuation of the cutting forces in hard turning is the result of chip segmentation and not the cause of it.

3.6 Microhardness analysis

Based on the above observations, it is obvious that different deformation patterns exist throughout the chip cross section. These changes in deformation patterns are

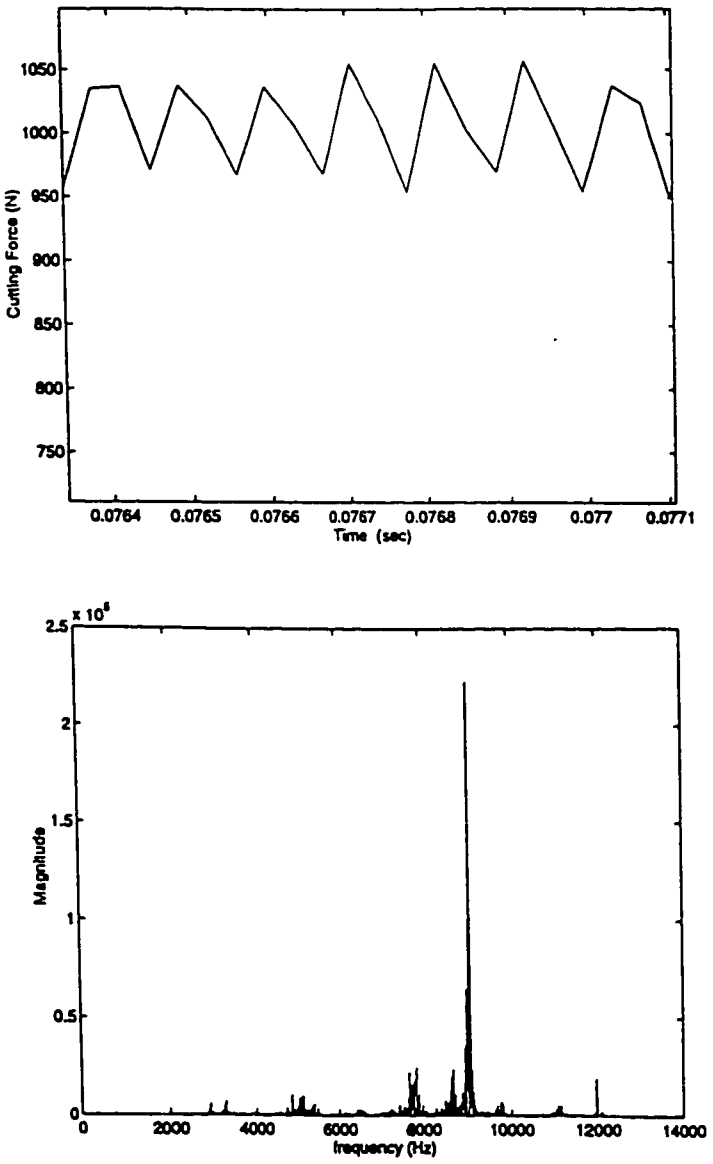

Fig. 3.11 Cutting force component when machining hardened steel
(V = 90 m/min, f = 0.075 mm/rev, d = 4 mm)

accompanied by a grain disturbance that alters the microhardness. Microhardness tests were conducted on chips collected at different cutting conditions. Figure 3.12 presents a typical saw toothed chips showing the change of the indentation size through the chip cross section. In this figure the distance between two indentations is less than the minimum distance and it was done for illustration purpose only. Different patterns of indentation size are observed at different cutting conditions. One zone with a large indentation size (lower hardness) and another zone with a small indentation size (higher hardness) are observed. The zones revealed represent areas that undergo different deformation processes. Figure 3.13-a shows a typical microhardness distribution on a saw toothed chip collected after an orthogonal cutting test performed at 90 m/min cutting speed. 0.15 mm feed and 4 mm depth of cut. The indentations in each figure were obtained from more than one saw toothed to maintain the minimum distance criterion between two successive indentations. The changes in microhardness values were observed and used to map out different zones of deformation. One zone with relatively smaller microhardness values was identified as shown in Fig. 3.13-(a and b). This zone includes segment II of the chip and the chip/tool interface, zone B. Another zone with relatively larger hardness values was observed in segment I of the chip, zone A. Figure 3.13-c represents the microhardness distribution through a chip cross section obtained at 90 m/min and 0.05 mm feed and 4 mm depth of cut. Again, two different zones of microhardness values can be recognized. However, due to the change in feed, the microhardness through the chip cross section is altered significantly. At a low feed, Fig. 3.13-(c and d), zone A has lower hardness values than zone B. Changes of the

a- V = 90 m/min, f = 0.15 mm/rev

b- V = 90 m/min, f = 0.075 mm/rev

Fig. 3.12 Different deformation zones in the chip cross section

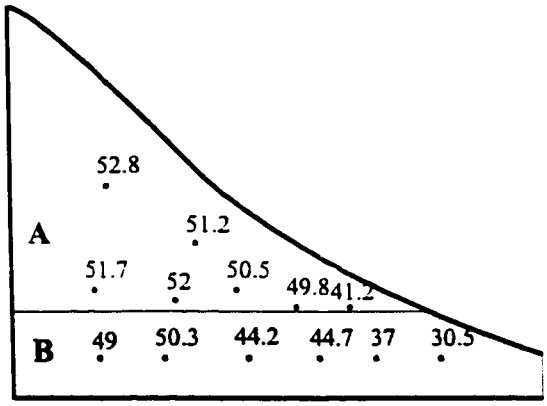

a- V = 90 m/min, d = 4 mm, f = 0.15 mm/rev

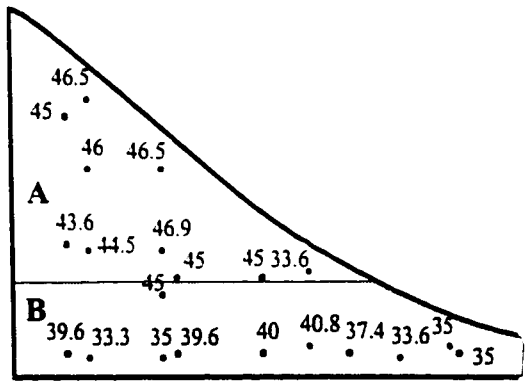

b- V = 90 m/min, d = 4 mm, f = 0.1 mm/rev

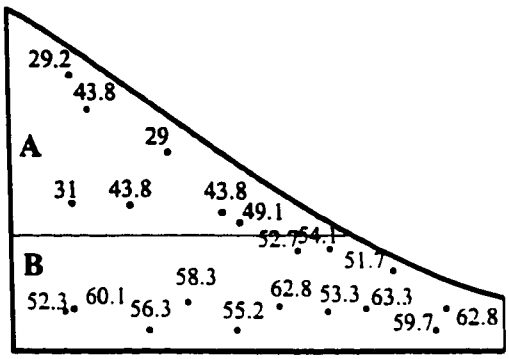

c- V = 90 m/min, d = 4 mm, f = 0.05 mm/rev

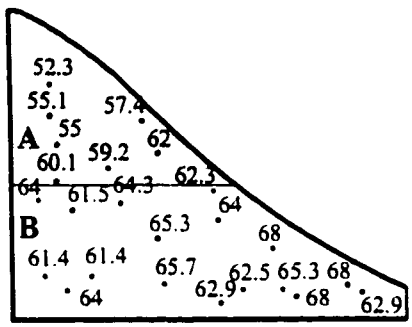

d- V = 90 m/min, d = 4 mm, f = 0.037 mm/rev

Lower average microhardness zone

Higher average microhardness zone

Fig. 3.13 Typical microhardness (Rc) distribution in saw toothed chip at different cutting conditions

microhardness values through the chip cross section can be attributed to a combined effect of both temperature and strain rate. Temperature causes thermal softening while the strain rate causes material hardening.

Figure 3.14 shows the effect of feed on the average microhardness value at different cutting speeds. One can conclude that at low cutting speeds, increasing the feed rate decreases the microhardness values. This can be attributed to the thermal softening of the chip material. An increase in the feed leads to an increase in the cutting temperature. Increasing the cutting temperature causes more tempering of the chip material and, hence, a decrease in the average microhardness value of the chip. At a higher cutting speed, the increase in the cutting temperature is mainly due to the cutting speed. The heat addition caused by increasing the feed in relatively small. Thus, at high cutting speed the contribution of feed in decreasing the microhardness is less.

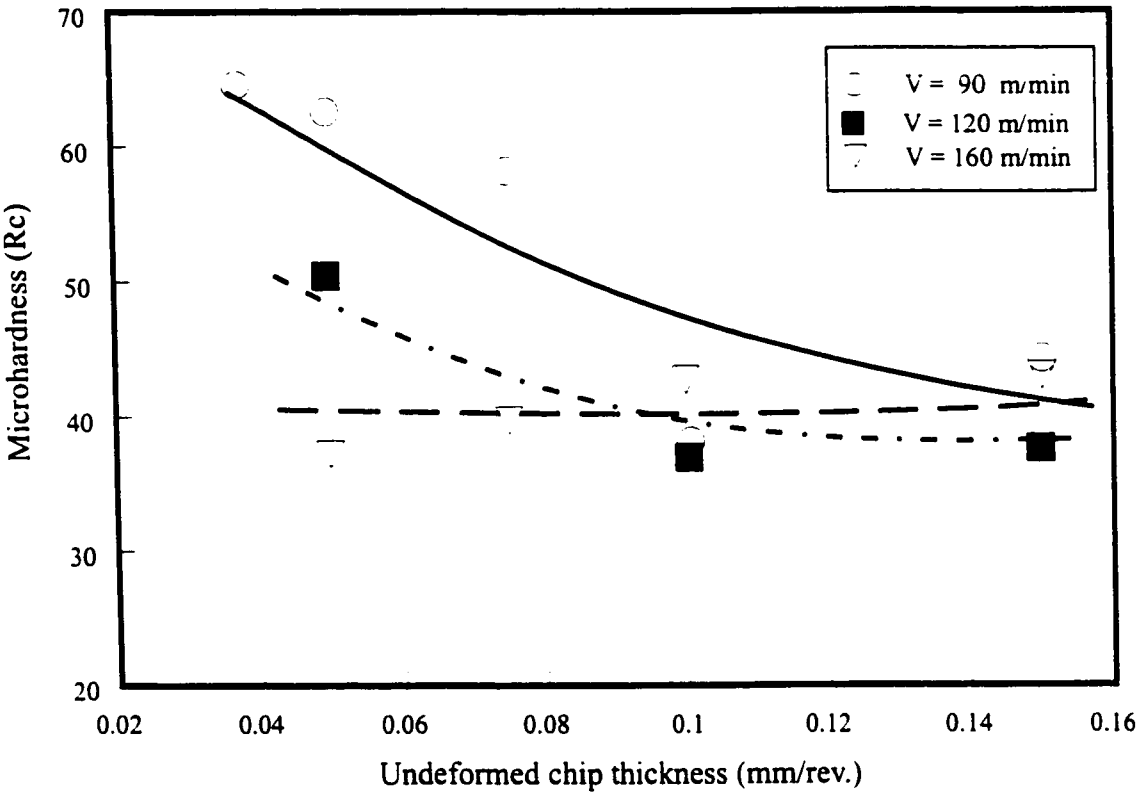

Fig. 3.14 Effect of cutting conditions on average chip microhardness

3.7 Effect of process parameters

3.7.1 Effect of nose radius

Figure 3.15-a shows a SEM image of the free surface of the chip formed during orthogonal machining of hardened steel. The scan electron microscopic analysis shows a strain disturbance along the chip width. This observation was consistent in all the chips examined and can be attributed to the inhomogeneity of the workpiece material. There is no evidence of edge serration through the transverse section of the chips. Figure 3.15-b shows a SEM image of chips collected when cutting with ceramic inserts having 1.2 mm nose radius. Chip serration along the trailing edge of the chip is observed. The same phenomenon was observed in chips collected after tests performed using round inserts as shown in Fig. 3.15-c. Note that the chip serration is observed only along the trailing edge. In fact, cutting using round inserts causes a differential loading along the chip cross section (El-wardany et al., 1995). The thickness varies along the chip width with zero value at the trailing edge. The mechanism of the trailing edge serration of the chip is explained in Fig. 3.16. The change of chip thickness along A-B causes stress concentration at point A where the chip thickness is almost zero. Moreover, the velocity of the chip particle varies across the chip thickness. The variation in chip particle velocities facilitates the nonuniform displacement along the chip width. In orthogonal machining, the effect of nose radius is eliminated and the chips obtained have a uniform chip thickness. Thus, there is no evidence of the stress concentration that leads to the trailing edge serration. This type of chip serration is of great importance since it causes the trailing edge wear of cutting tools.

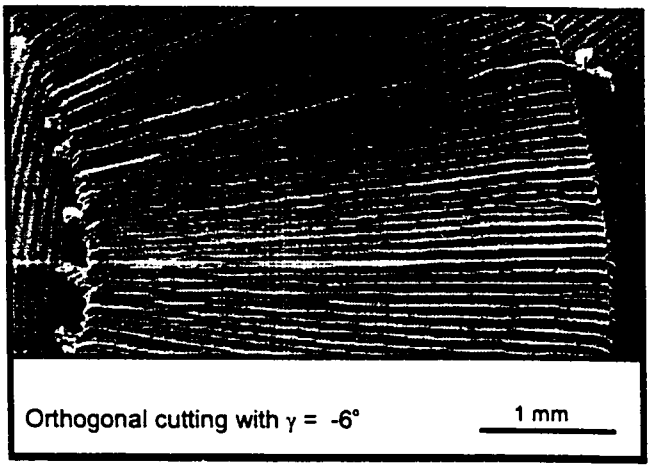

(a)

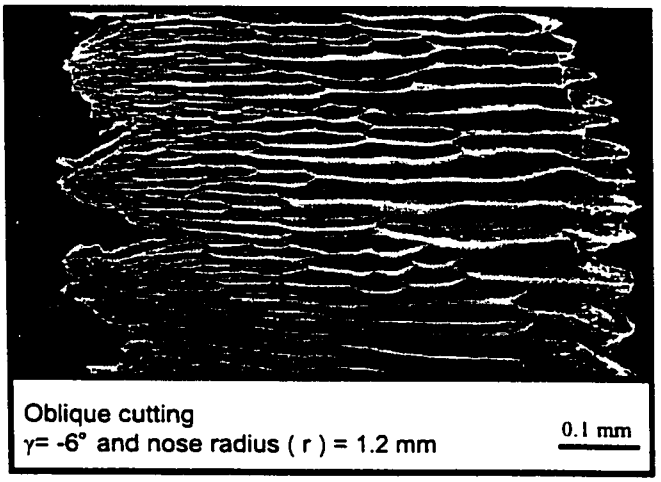

(b)

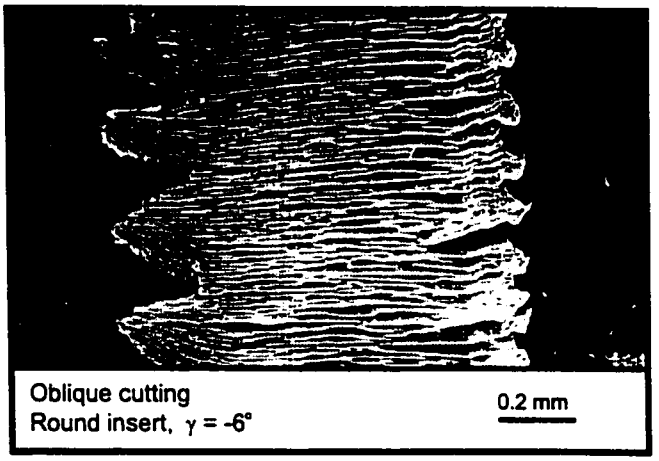

(c)

Fig. 3.15 SEM images for the free surface of chips obtained using different tools

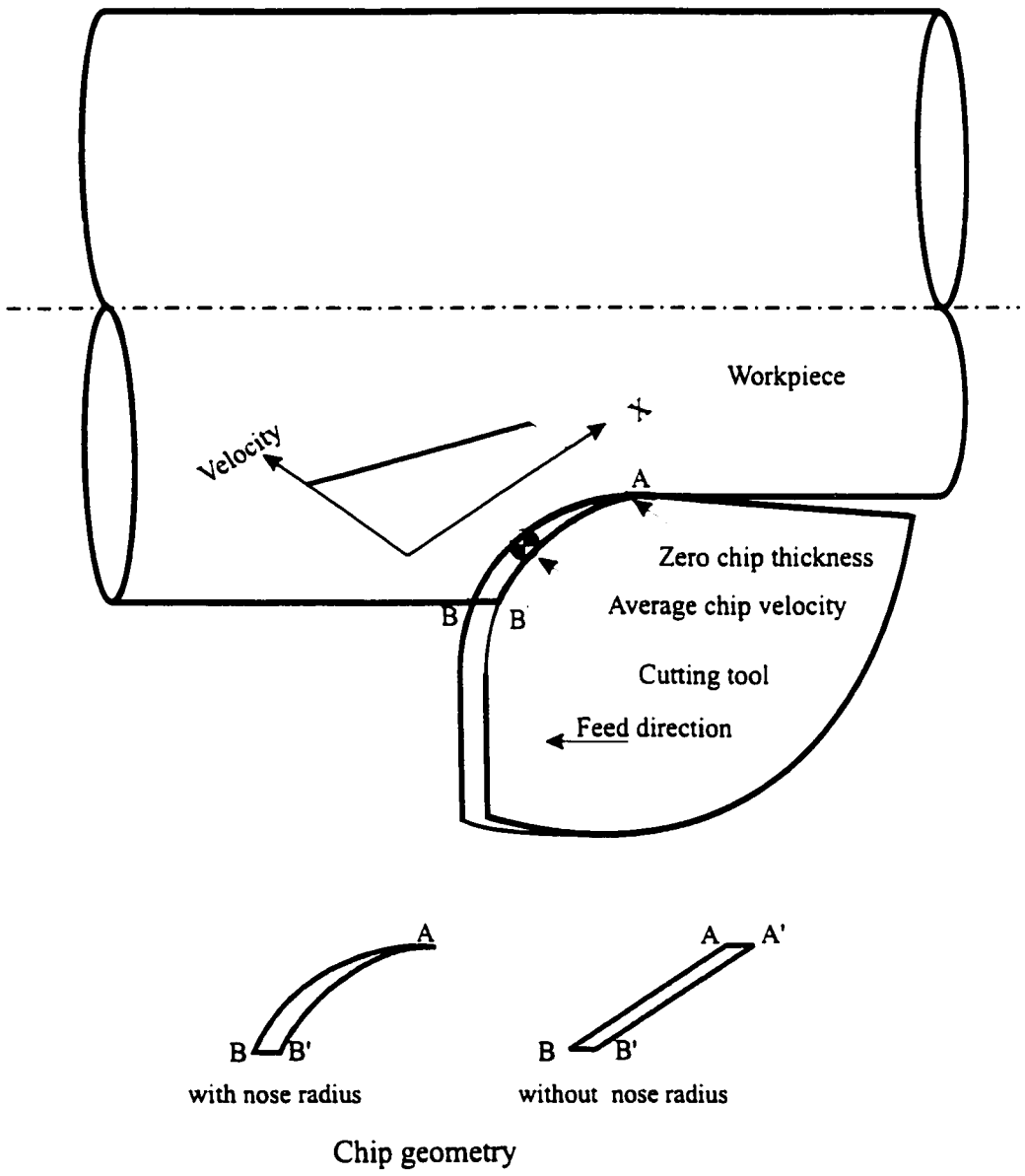

Fig. 3.16 Effect of nose radius on chip morphology

3.7.2 Effect of tool wear

Figure 3.17 shows an optical microscopic image of two saw toothed chips collected after the same cutting conditions using a sharp tool and a worn tool. Cutting with a worn tool leads to smaller saw toothed chips with cross sections similar to those of continuous chips. This can be attributed to the increase of thermal and mechanical loads due to tool wear. Increasing the thermal and mechanical loads increases the penetration of the plastic deformation through the chip thickness. Thus, the crack developed at the free surface of the chip ceases due to the plastic deformation that covers a large area of the chip.

3.7.3 Effect of edge preparation

The effect of tool edge chamfer on the chip morphology is illustrated in Fig. 3.18. A comparison between two chips obtained under the same cutting conditions shows that while serrations exist on the trailing edge of the chip when cutting with a sharp tool, they exist on both edges of the chip when cutting with a chamfered tool. As previously mentioned in section 3.7.1, the roundness of the cutting edge causes differential loading that leads to inhomogeneity of the strain distribution along the chip width, causing tearing on the weakest edge of the chip. The chamfering of the cutting edge increases the effective rake angle and causes severe stress on the chip. Consequently, the stress values at both edges of the chip exceed the ultimate tearing stress and cause serration on both edges of the chip. In this case, the existence of the chip edge serration not only facilitates the trailing edge wear, but also facilitates the depth of cut notch when cutting with a large depth of cut.

a- Sharp tool

b- Worn tool

Fig. 3.17 Effect of tool wear on chip morphology
nose radius = 3.2 mm, rake angle = -6°, angle of approach = 0°
(V = 120 m/min, f = 0.1 mm/rev, d = 0.25 mm)

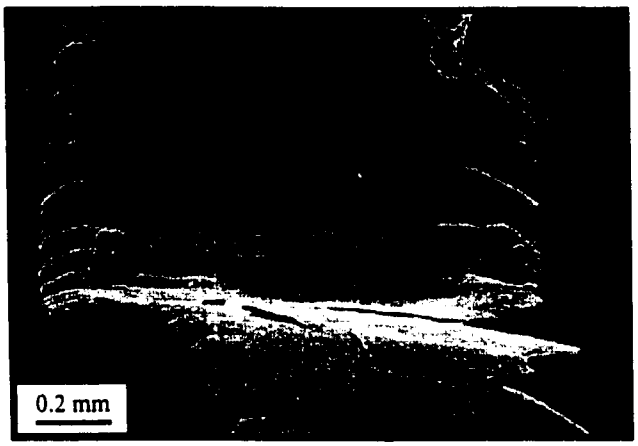

a- Sharp cutting tool

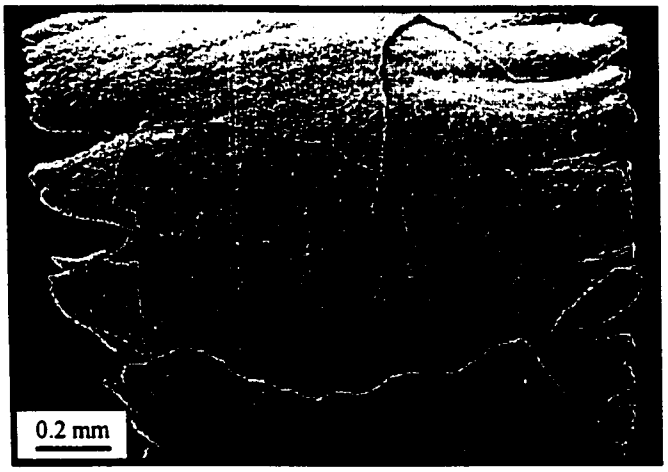

b- Chamfered cutting tool

Fig. 3.18 Effect of edge preparation on chip morphology

The significant difference in notch wear patterns of chamfered and sharp edge inserts was reported by Hodgson and Trendler (1981). The same observations of the chip edge serration were obtained when cutting with 0° and 30° angles of approach, as can be seen in Fig. 3.19. Again, this can be attributed to the change of the state of stress across the chip due to the change in the angle of approach.

3.7.4 Effect of feed

Figure 3.20 shows a comparison between saw toothed chips obtained at two different feeds. In both cases, the crack developed at the free surface of the chip is observed. However, when cutting with a small feed, the cross section is approximately similar to those of continuous chips. The same observation was reported without explanation by König et al. (1993). This observation can be attributed to the fact that the cracks initiated at the free surface were terminated due to plastic deformation that covered a large area of the chip cross section (Shaw, 1995). Figure 3.21 depicts the ratio of the maximum plastically deformed chip thickness (t_{pmax}) to the maximum saw toothed chip thickness (t_{max})as a function of the undeformed chip thickness. At very small undeformed chip thickness, the plastic deformation is increased and causes early ceasing of the crack. When cutting with very small undeformed chip thickness, the tool tip radius is considerably larger than the undeformed chip thickness. This leads to an increase of the effective rake angle. Therefore, an extensive compressive stress exists through a larger area of the chip cross section where plastic deformation develops.

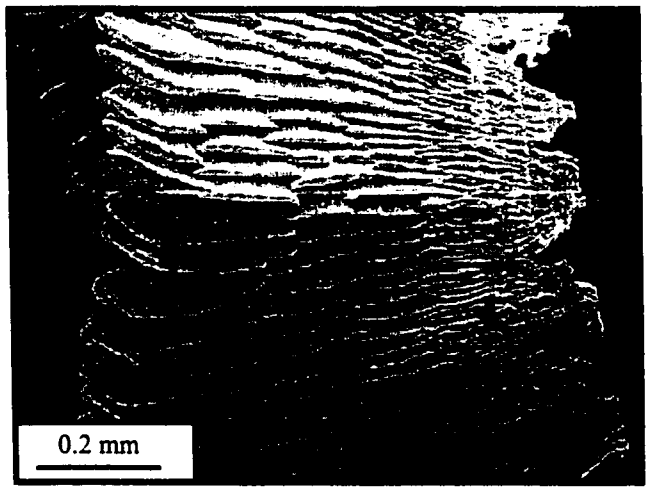

a- Zero angle of approach

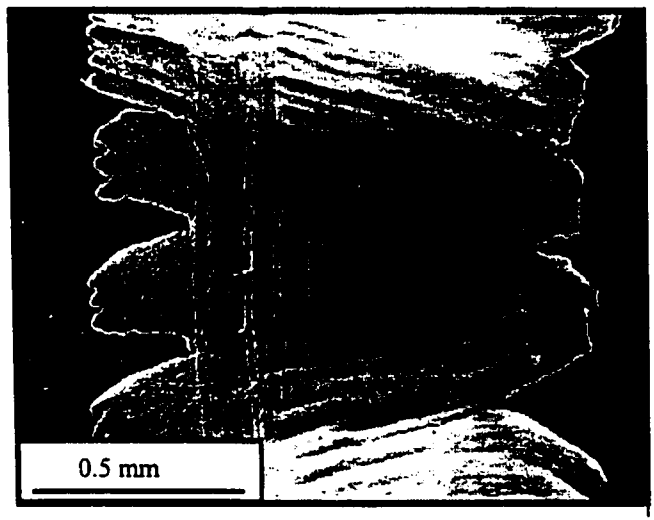

b- 30 degree angle of approach

Fig. 3.19 Effect of angle of approach on chip morphology
(V = 120 m/min, f = 0.1 mm/rev, d = 0.2 mm)

a- Small feed f = 0.01 mm/rev

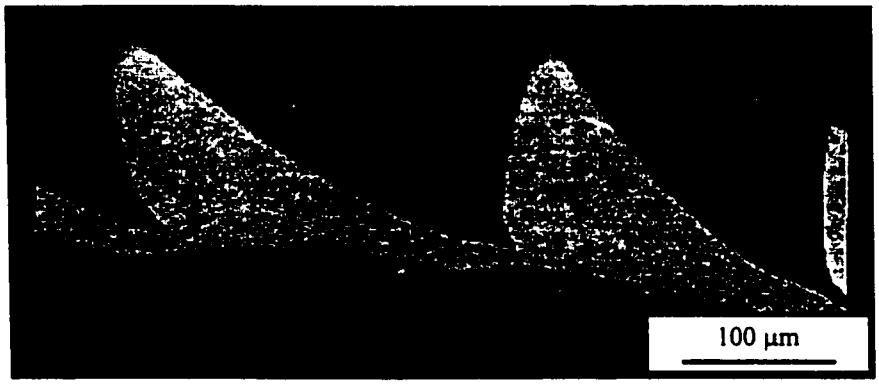

b- Large feed f = 0.15 mm/rev

Fig. 3.20 Effect of feed on chip morphology
(V = 90 m/min, d = 4 mm)

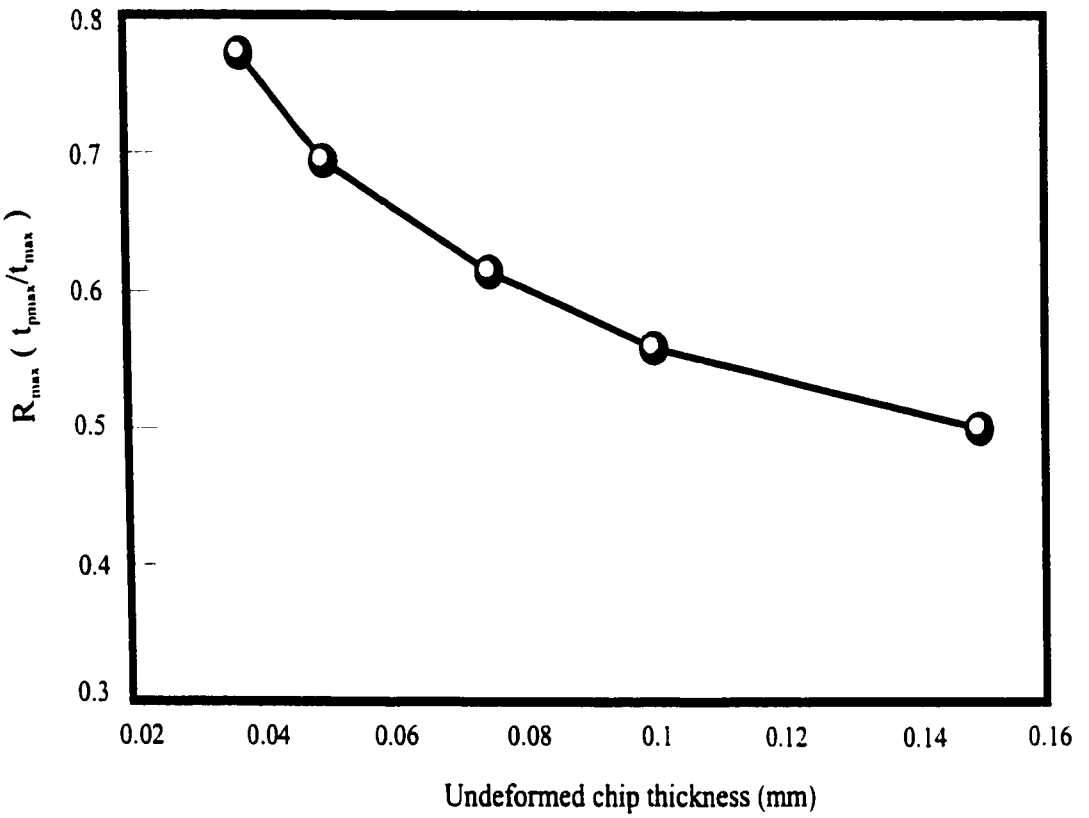

Fig. 3.21 Effect of undeformed chip thickness on R_{max}

Figure 3.22 shows SEM images of the free surface of the chip as well as the tool/chip interface surface. A comparison between the segmentation distances reveals the direct proportionality between the segmentation distance and the feed . The results obtained are in good agreement with the results reported in section 3.5 and those reported by Davies et al. (1996).

3.7.5 Effect of cutting speed

Figure 3.23 shows optical microscope images of two chip cross sections obtained at two different cutting speeds. One can conclude that cutting speed (within the used range) does not have a significant effect on the chip morphology. Saw toothed chips were obtained at all the cutting speeds used in this investigation. Figure 3.24 represents the effect of cutting speed on the segmentation distance. It is found that increasing the cutting speed decreases the segmentation distance. This observation is in contradiction with the data presented by Davies et al. (1996). However, it seems consistent with the results reported by Lindberg and Lindstörm (1983). The decrease in the segmentation distance is attributed to the high frequency of cracks initiated in front of the cutting tool at high cutting speeds. A detailed explanation of the effect of cutting speed on the chip segmentation is given in section 3.5.

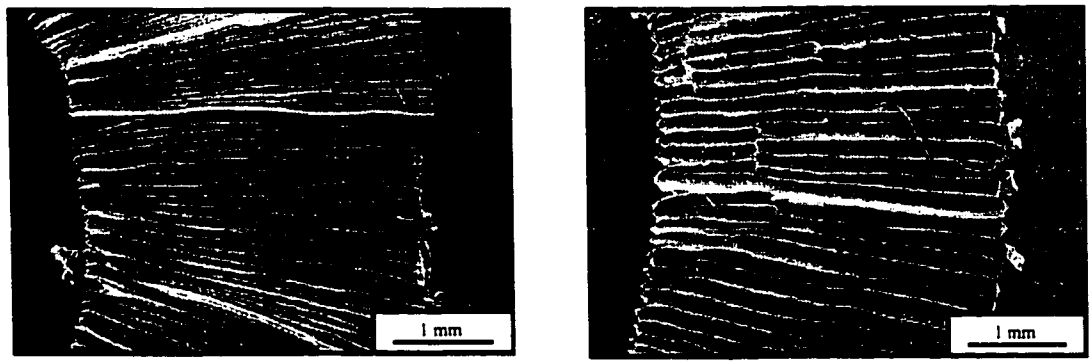

f = 0.05 mm/rev f = 0.15 mm/rev

a- Chip free surface

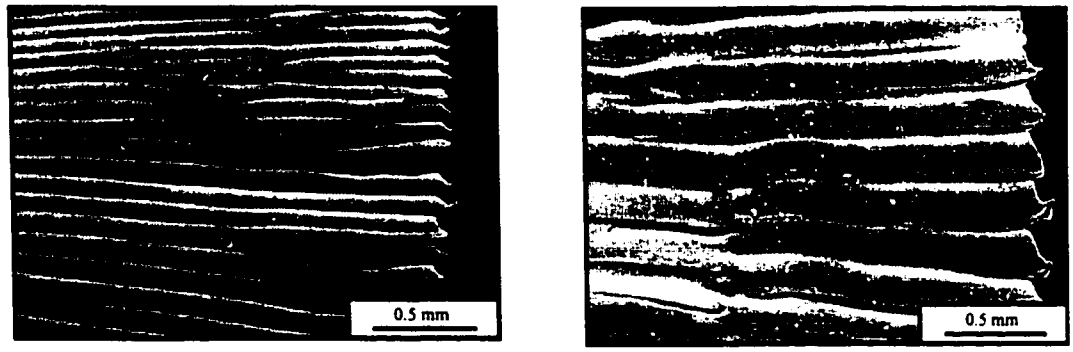

f = 0.05 mm/rev f = 0.15 mm/rev

b- Chip tool contact surface

Fig. 3.22 SEM images showing the effect of feed on the chip segmentation distance (V = 120 m/min, d = 4 mm)

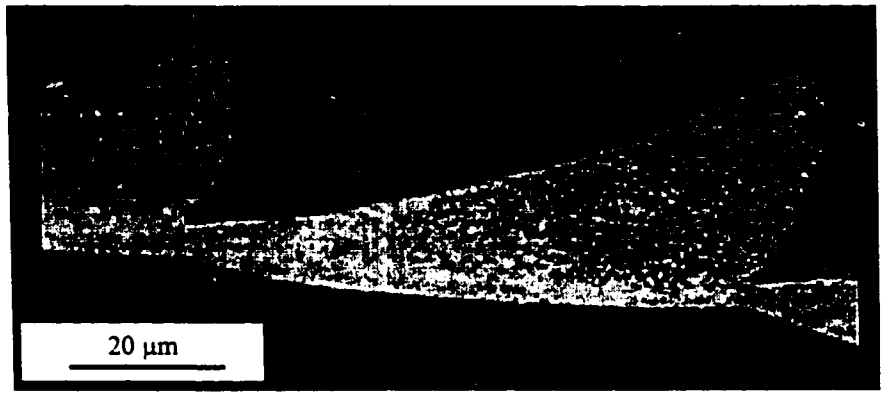

a- Cutting speed V = 160 m/min

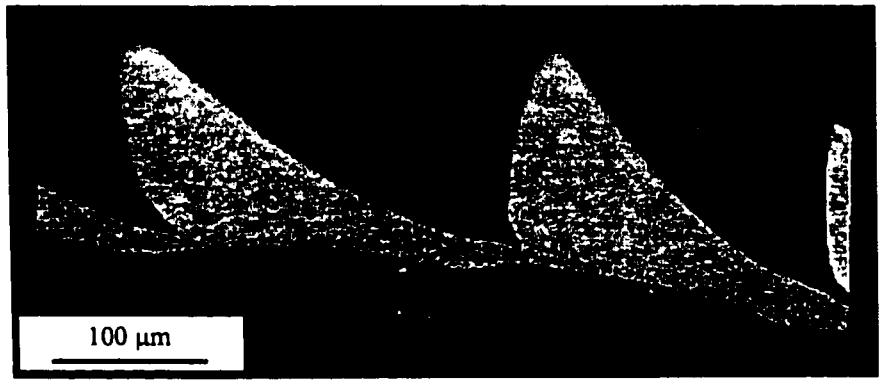

b- Cutting speed V = 90 m/min

Fig. 3.23 SEM images showing the effect of cutting speed on chip morphology (f = 0.15 mm/rev, d = 4 mm)

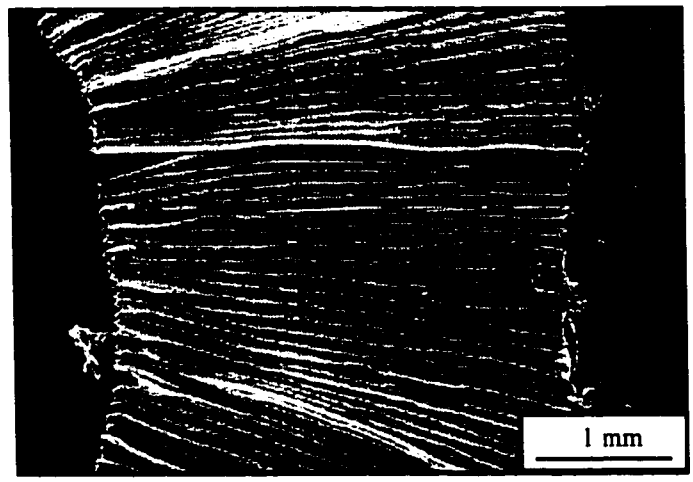

a- Cutting speed, V = 120 m/min

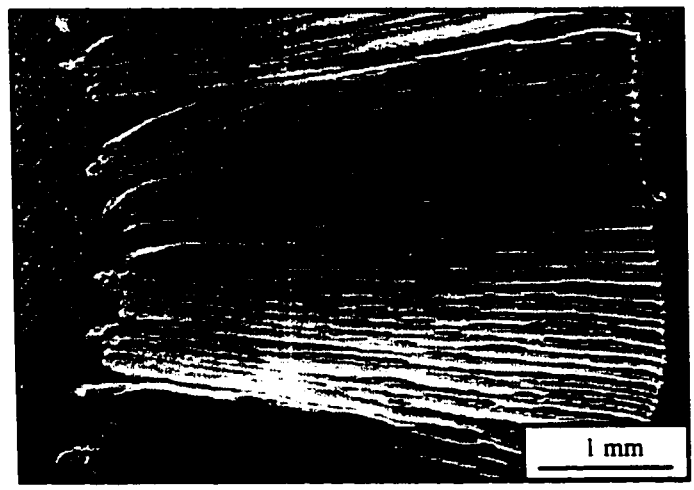

b- Cutting speed, V = 160 m/min

Fig. 3.24 SEM images showing the effect of cutting speed on chip segmentation (f = 0.05 mm/rev, d = 4 mm)

CHAPTER 4

RESIDUAL STRESSES: EXPERIMENTAL INVESTIGATION

4.1 Introduction

The fatigue performance of a mechanical component as well as its dimensional stability are directly influenced by the residual stresses generated during Machining. The final distribution of these stresses beneath the machined surface must satisfy the compatibility and equilibrium conditions. The evaluation of residual stresses is an important factor for the prediction of the long term failure of mechanical components, and their resistance to brittle crack propagation. Unfortunately, residual stresses cannot be measured directly in the manner used to determine ordinary stresses. Residual stresses can only be

determined by measuring the strains which exist in the part that is residually stressed.

In this chapter, an experimental investigation is presented to study the effect of different process parameters such as edge preparation, nose radius, cutting speed, feed, and depth of cut on the residual stress distribution beneath the machined surface.

4.2 The x-ray diffraction technique

X- ray diffraction is one of the well developed techniques used for residual stress measurements. It is simple, accurate, and has been used previously by several investigators to study the machined surface. The basic principle of the x-ray technique is based on the determination of the interplaner spacing of metallic materials using Bragg's equation:

$$n\lambda = 2d \sin(\theta_p) \tag{4.1}$$

where n is the natural number, λ is the wave length, d is the interplaner spacing, and θ_p is the peak angle. The peak angle is determined by using the diffractometer, which scans along an arc to measure the density of the diffracted x-rays, as shown in Fig. 4.1.

Figure 4.2 represents a machined surface subjected to a plane stress condition ($\sigma_3 = 0$) at the surface. Although the plane stress condition is considered in this figure, there is lateral contraction due to Poison's ratio and the third strain component (ε_3) exists and is given by:

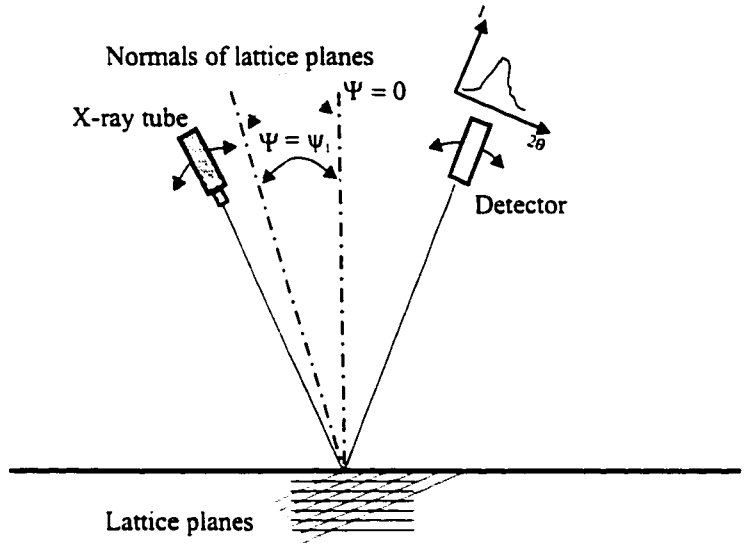

Fig. 4.1 X-ray stress measurement

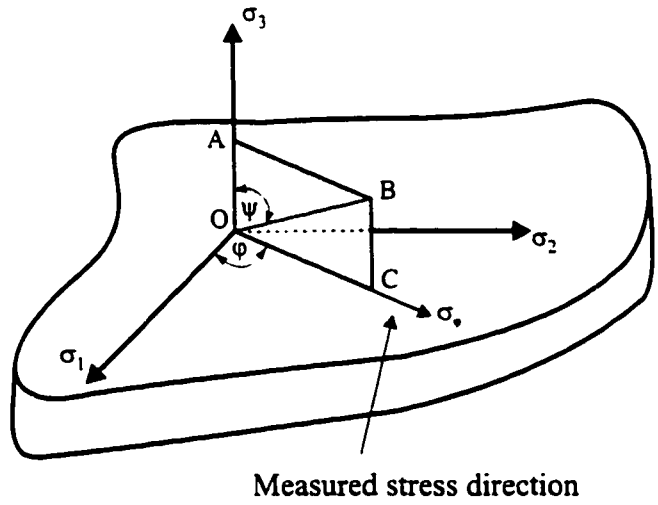

Fig. 4.2 Stress at a point on machined surface

$$\varepsilon_3 = -\nu(\sigma_1 + \sigma_2) \tag{4.2}$$

where ε_3 is calculated as a function of the interplaner spacing, d_o is the spacing of the planes perpendicular to the third direction of the stress free body, and d_n is the planes spacing of the stressed body. Equation (4.2) can be rewritten as :

$$\frac{d_n - d_o}{d_o} = -\nu(\sigma_1 + \sigma_2) \tag{4.3}$$

To determine the value of σ_φ in Fig. 4.2, two successive measurements are required. One is d_n for a set of planes whose surface normal is along ε_3, and the second is d_ψ for the same set of planes lying at some angle relative to the surface normal as shown in Fig. 4.3 From the elasticity theory for isotropic solids, the strain along the inclined line OB is given by:

$$\varepsilon_\psi = \frac{1}{E}[\sigma_\varphi(1+\nu)\sin^2\psi - \nu(\sigma_1 + \sigma_2)] \tag{4.4}$$

From equations (4.2) and (4.4):

$$\varepsilon_\psi - \varepsilon_3 = \frac{\sigma_\varphi}{E}(1+\nu)\sin^2\psi \tag{4.5}$$

In this equation, the difference between two strains is equal to the stress acting in the plane of these strains. Since d_o and d_n are almost equal, the value of d_o can be replaced by

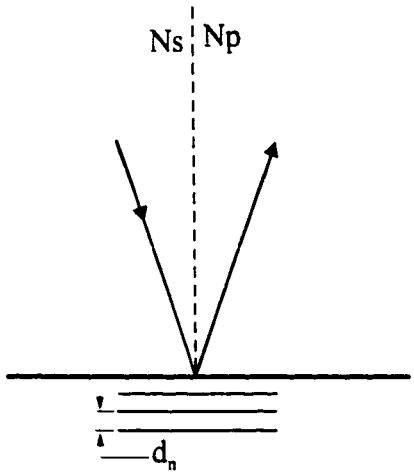

a- Measurement of d_n

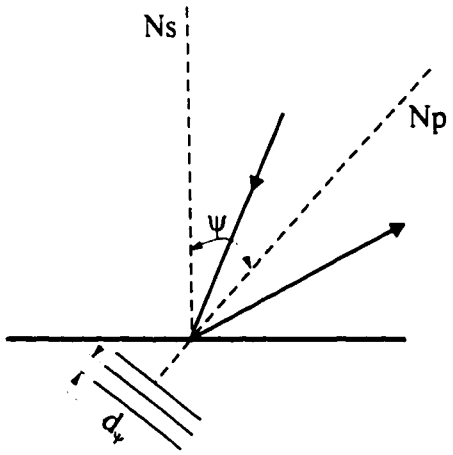

b- Measurement of d_ψ

Fig. 4.3 Orientation of x-ray beams relative to specimen
Ns = Normal to specimen surface
Np = Normal to reflecting planes

d_n and equation (4.5) can be written in this form (Cullity, 1978):

$$\sigma_\varphi = \frac{E}{(1-\nu)\sin^2\psi}\left\{\frac{d_\psi - d_n}{d_n}\right\} \tag{4.6}$$

In equation (4.6), residual stress can be calculated without knowing the stress free lattice spacing. Since the values measured during the experiment are the diffraction angles, it is easier to write equation (4.6) as a function of the diffraction angles:

$$\sigma_\varphi = K\,(2\theta_n - 2\theta_\psi)$$

$$\textit{where} \tag{4.7}$$

$$K = \frac{E\cot\theta}{2[1+\nu]\sin^2\psi}$$

Since the x-ray measurements depend on the determination of the change in the interplaner spacing of a particular set of planes, the mechanically measured elastic constants are not appropriate for x-ray measurements. The appropriate elastic constants can be obtained from shifts in the (d) spacing for a series of applied loads. Fortunately, the mechanically determined elastic constant values for steel can be used for x-ray diffraction when using chromium radiation (Hilly et al., 1980).

4.3 Experimental procedure

In this experimental investigation, workpieces of D2 tool steel material were used. The workpieces were received in the form of bars having 70 to 100 mm diameter and 150 to 200 mm length. The material has a fine tempered martensite microstructure with a hardness of 60 to 62 HRc. Dry bar turning was performed using PCBN cutting tools (BZN 8100) with -6 degree rake angle on a CNC standard modern lathe with a 10 HP spindle motor and 1600 rpm spindle speed. The cutting conditions and tool specifications are given in Table 4.1.

Table 4.1 Cutting conditions and tool specifications for residual stress investigation

Process Parameters	Cutting Range			
Cutting speed, V m/min	140	270	350	500
Depth of cut, d mm	0.2	0.4	0.6	--
Feed, f mm/rev	0.05	0.1	0.2	--
Tool nose radius r mm	0.8	1.2	1.6	--
Edge preparation	Sharp	Chamfered (20°/0.1 mm)	Honed (0.0125 mm)	--

Sharp and worn tools were used. Tests were performed starting with a new tool and then allowing continuous cutting until nose wear reached 0.5 mm. Cutting forces were measured using a piezoelectric three force component dynamometer. Tool wear was measured using a tool maker's microscope.

Measurements of residual stresses were performed using an x-ray diffraction

technique. The measurements were performed using a two angle sine squared psi technique, in accordance with GE specification 4013195-991 and SAE J784a, employing the diffraction of chromium K-alpha radiation from the (211) planes of the D2 tool steel. Details of the diffractometer fixturing are outlined below:

Incident Beam Divergence:	0.5 deg.
Detector:	Si(Li) set for 90% acceptance of the chromium K-alpha energy.
Psi Rotation:	10 deg. and 50 deg.
Irradiated Area:	2.5 mm x 2.5 mm.

X-ray diffraction residual stress measurements were performed at nominal depths of 5, 15, 35, 50, and 90 x 10^{-3} mm. All of the measurements were performed in the circumferential direction. The value of the x-ray elastic constant, E/(1+ν), required to calculate the macroscopic residual stress from the strain measured normal to the (211) planes was obtained from Prevey (1986) in accordance with ASTM E1426-91. Material was removed electrolytically for sub-surface measurement, minimizing any possible alteration of the sub-surface residual stress distribution as a result of material removal. All data obtained as a function of depth were corrected for the penetration of radiation employed for residual stress measurement into the sub-surface stress gradient (Koistinen and Maburger, 1959). Corrections for sectioning stress relaxation and for stress relaxation caused by layer removal (Moore and Evans, 1958) were applied appropriately.

4.4 Machining residual stresses

In machining with geometrically defined cutting edges, the heat absorbed in the workpiece is around 10-15% of the total cutting energy, and the penetration depth of the heat is much less due to the higher workpiece speed compared to that of the grinding process. During dry cutting, the thermal stresses on the surface layer are capable of producing tensile residual stresses. This is because during dry cutting, the material layer near the surface is heated and elongated more than the bulk material of the workpiece. Therefore, the surface layer expands and experiences a compressive stress resulting from the bulk material beneath it. If this compressive stress exceeds the yield stress, then tensile residual stress will remain in the surface element after cooling. The deformation of the surface layer due to the applied mechanical load may produce both tensile and compressive residual stresses. The existence of tensile or compressive residual stress as the cutting speeds increase will depend to a great extent on the depth of the permanent plastic deformation zone which penetrates into the machined surface. This zone depends on the stresses generated by the mechanical and thermal loads which exist during cutting. If these stresses do not reach the material yielding point, the residual stress will not exist on the workpiece surface.

4.5 Effect of process parameters on residual stresses

4.5.1 Effect of cutting speed

Cutting speed has a significant influence on the residual stresses generated during machining because of its effect on the cutting temperature. The effect of the cutting speed

on the induced residual stress depends, to a great extent, on the type of material and the cutting tool used during machining. The dependance of the magnitude of residual stresses on the mechanical properties of the workpiece material can be found in the paper published by Schreiber and Schlicht (1986). The effect of the cutting speed is usually related to the amount of heat generated during cutting. The higher the cutting speed, the higher the cutting temperature generated. Figure 4.4 shows the effect of cutting speed on the residual stresses distribution beneath the machined surface. Three cutting speeds are used in this comparison with a depth of cut d = 0.2 mm, a feed f = 0.1 mm/rev., and a sharp PCBN cutting tool having -6° rake angle and 1.2 mm nose radius. Although increasing the cutting speed generates more heat, the magnitude of unfavourable generated tensile residual stress on the machined surface is reduced. Similar results were obtained by Liu and Barash(1982) during the machining of low carbon steel where higher values of tensile residual stresses were obtained at a low cutting speed. During machining, around 10-15% of the heat generated flows into the workpiece. Therefore, when machining at a high cutting speed, the amount of heat going into the workpiece is of lesser proportion due to the high rotational speed of the workpiece. In addition, an increase in the cutting speed increases the temperature in the primary cutting zone, which leads to thermal softening and to a decrease in the cutting forces. Thus, increasing the cutting speed not only produces less tensile residual stress in the machined surface but also decreases the peak of compressive residual stresses beneath the machined surface which is caused by the mechanical load as shown in Fig. 4.4.

Figure 4.5 depicts the effect of cutting speed on the thickness of a residually

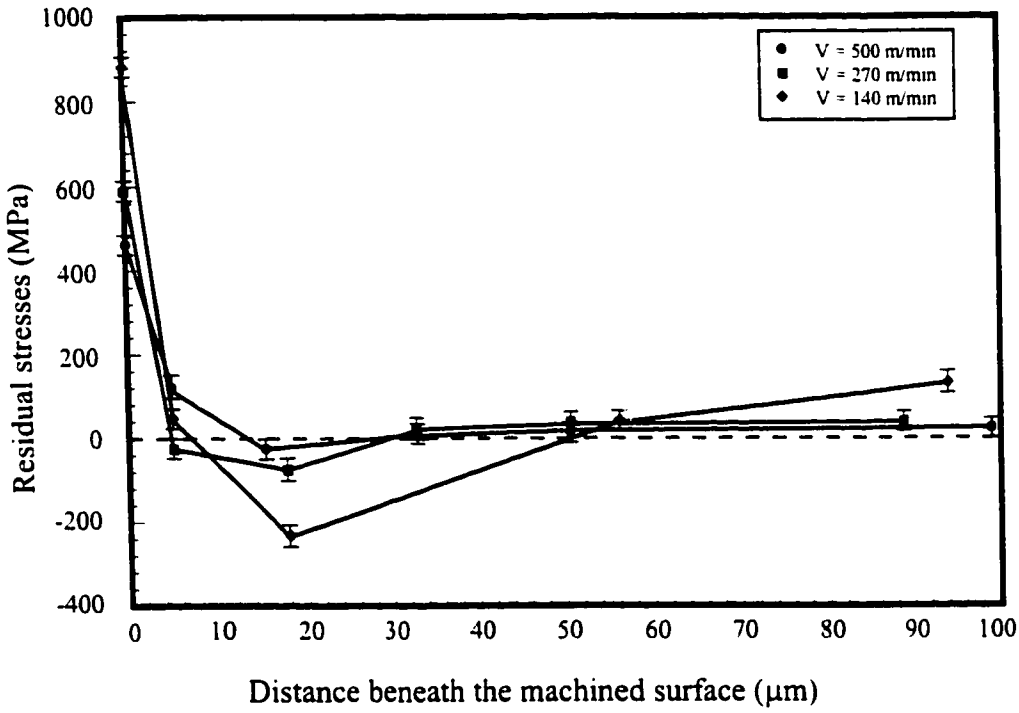

Fig. 4.4 Effect of cutting speed on residual stresses distribution
(f= 0.1 mm/rev, d = 0.2 mm, r = 1.2 mm, sharp cutting edge)

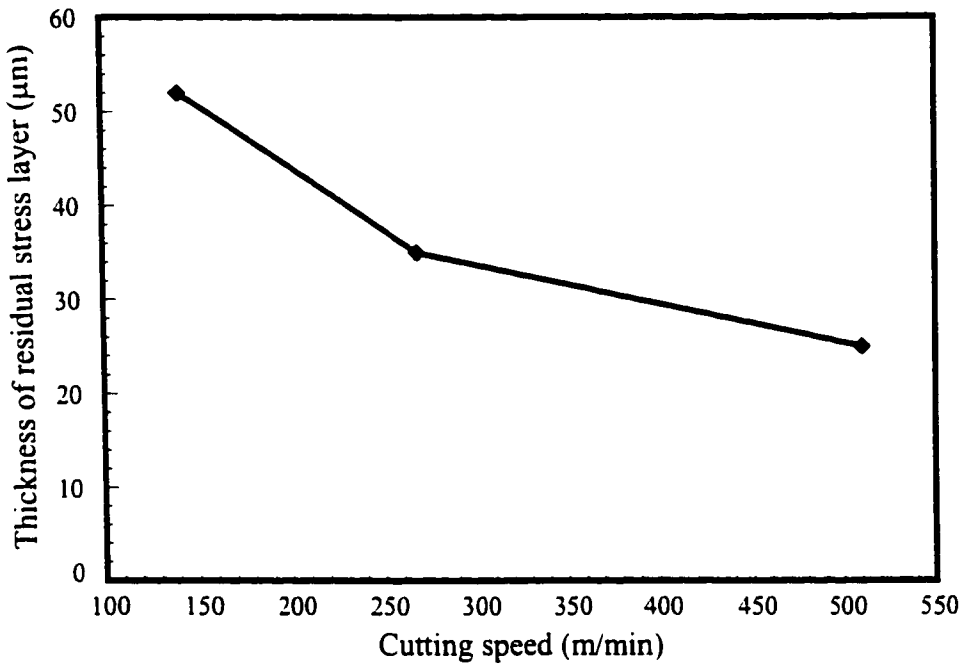

Fig. 4.5 Effect of cutting speed on the thickness of residual stress layer
(f= 0.1 mm/rev, d = 0.2 mm, r = 1.2 mm, sharp cutting edge)

stressed layer in the machined surface. As expected, an increase in the cutting speed reduces the thickness of this layer. Again, this can be attributed to the fact that most of the heat generated goes into the chips resulting in shallower heat penetration into the machined surface. In addition, the mechanical load is reduced due to the effect of thermal softening at high cutting speed. Hence, as a result of thermal softening, the depth of residual stresses in the machined surface is reduced. Thus, it can be concluded that with respect to residual stresses, machining at high cutting speed is considered beneficial.

4.5.2 Effect of feed

The residual stress level on the surface layer generated by hard turning shows remarkable changes depending upon the cutting conditions, as shown in Figs. 4.6 (a and b). An increase in the feed, even if the cutting process is performed with an artificially worn tool of 0.2 mm, changes the residual stress on the workpiece machined surface from tensile (65 MPa at a feed of 0.05 mm/rev) to compressive stresses (-78 MPa at a feed of 0.2 mm/rev), as seen in Fig. 4.6-a. The thermal energy generated during hard turning of D2 tool steel (in excess of 1000 °C at the cutting edge) only acts on the very thin outermost surface layer. This is due to the fact that the majority of the heat is dissipated by the chips. Increasing the chip thickness allows for more heat dissipation through the chips. This, obviously, reduces the internal tensile stresses generated by the thermal load and allows the mechanically induced residual compressive stress to reach its maximum value below the surface at greater depths. This explains the change in the state of the residual stress from

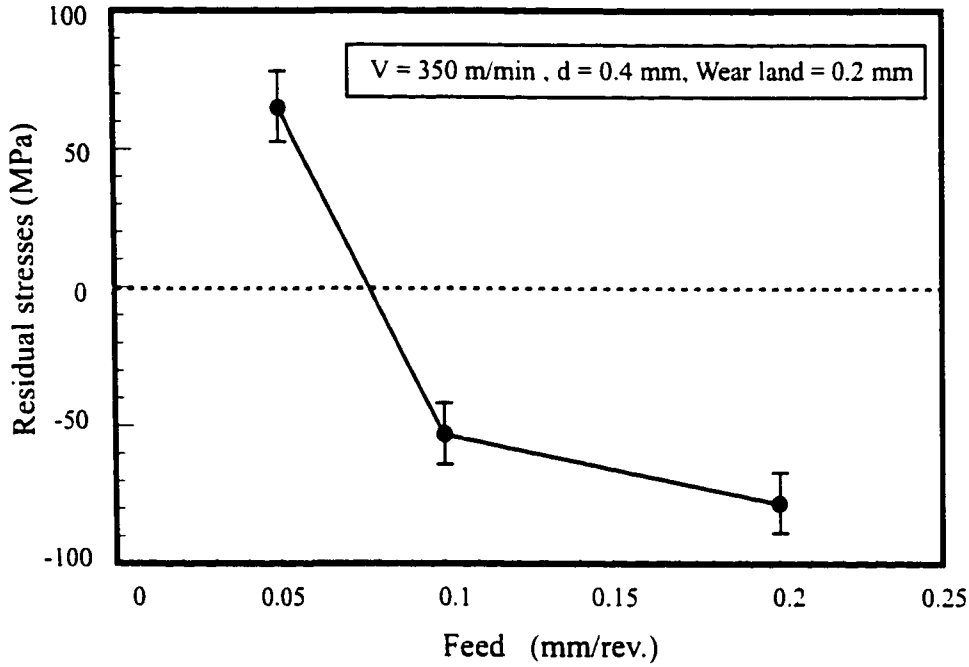

a- Residual stresses at different feeds (worn tool)

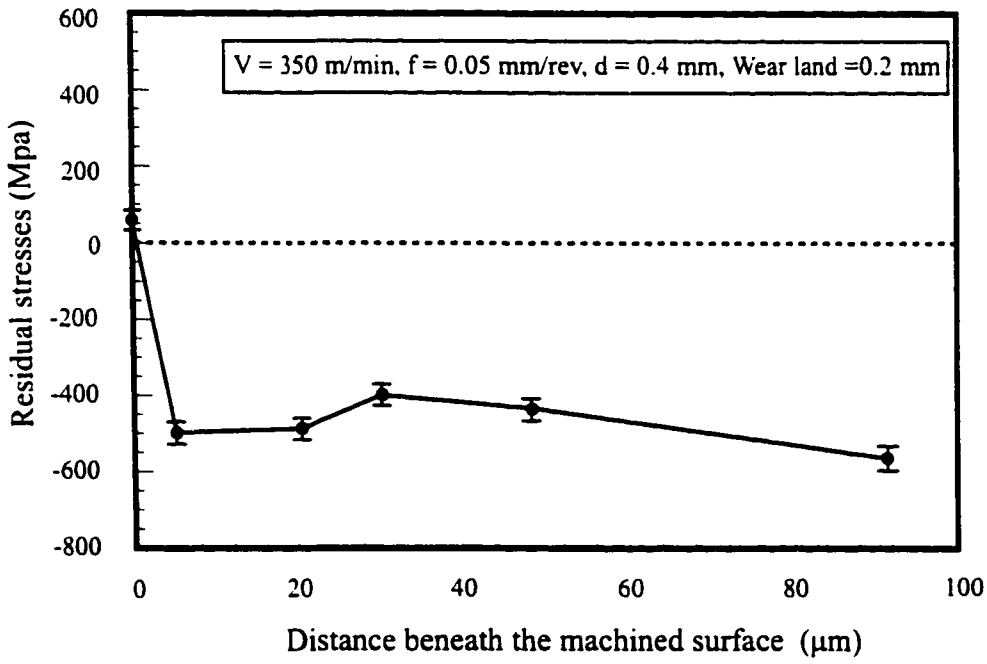

b- Distribution of residual stresses at low feed

Fig. 4.6 Effect of feed on residual stresses

tensile to compressive as the feed increases. Figure 4.6-b shows the residual stress distribution in the machined surface measured in circumferential direction when a feed of 0.05 mm/rev is used and the tool flank wear is 0.2 mm, keeping all the other cutting conditions of Fig. 4.6-a the same. As can be seen from this figure, a small amount of tensile residual stress existed on the surface and a large amount of compressive stress existed at a distance between 7.6 μm and 91μm beneath the surface.

4.5.3 Effect of depth of cut

Figure 4.7 shows that, for the same cutting speed and using a tool with an artificial flank wear of 0.2 mm, no residual stress is induced on the workpiece surface when the depth of cut was 0.6 mm. This is significantly different from the direct comparison to the high tensile residual stress induced on the workpiece surface when the depth of cut was 0.2 mm. The same figure also illustrates that increasing the depth of cut affects, to a great extent, the distribution of the residual stress. The maximum compressive stress occurs at a distance of 7.6 μm beneath the surface when the depth of cut was 0.6 mm, compared to 30 μm when a 0.2 mm depth of cut is used. Also, the compressive stress penetrates deeper into the surface layer when the depth of cut is 0.2 mm. This indicates high sub-surface softening and the existence of a tempered surface when the smaller depth of cut is used.

The results presented in this section indicate that by selecting specific cutting conditions, a surface free of residual stress can be obtained even if a considerably high speed is used. Eliminating or minimizing the residual stresses in the surface layers of a machined

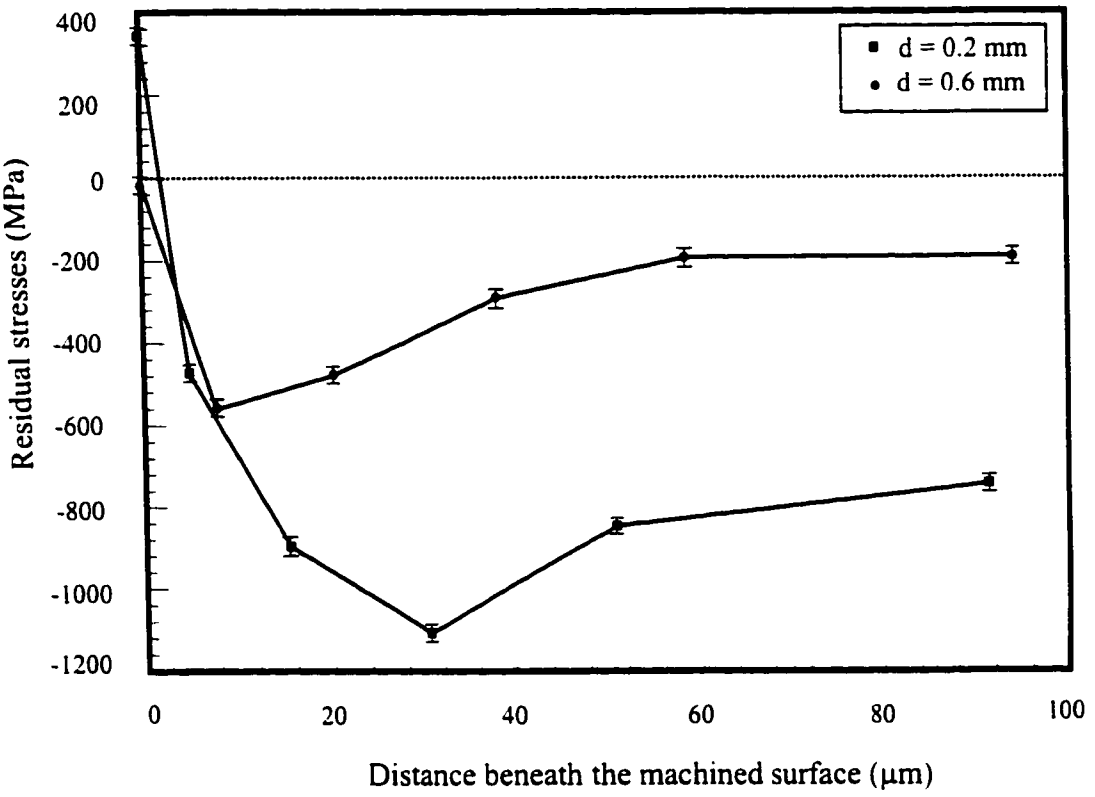

Fig. 4.7 Effect of depth of cut on residual stresses distribution
(f = 0.1 mm/rev, V = 350 m/min, Wear land = 0.2 mm)

component can improve the static and dynamic strength, as well as the magnetic and chemical properties of the surface.

4.5.4 Effect of tool wear

Figure 4.8-a shows the residual stress distribution in the machined surface measured in circumferential direction. The cutting conditions used are cutting speed, V=350 m/min, feed, f = 0.1 mm/rev, and depth of cut, d = 0.4 mm. A PCBN cutting tool with a nose radius of 1.2 mm, the rake angle = -6° and 20°/0.1 mm chamfered with a 0.0125 mm honed radius is used. No artificial flank wear is induced on the cutting edge in this case. As can be seen in Fig. 4.8-a, the residual stresses lie within the favourable compressive range of -259 MPa at the surface and reaches a maximum negative stress of -677 MPa at a distance of 7.6 μm beneath the surface. When tool nose wear reaches 0.2 mm, compressive residual stress in the surface layer is -59 MPa. The compressive residual stress is converted to tensile stress, which tends to penetrate deeper beneath the surface as the flank wear continues to increase (Fig. 4.8-b). These results are expected based on the fact that, in hard turning, chip formation produces high restoring forces and induces a compressive residual stress state in the workpiece surface zone due to high mechanical stress. However, tool wear and, consequently, the friction induce temperature rise resulting in a tensile residual stress on the workpiece surface. PCBN tools with a low fraction percentage, such as those used in this investigation, have a lower thermal conductivity so that the cutting temperature can reach

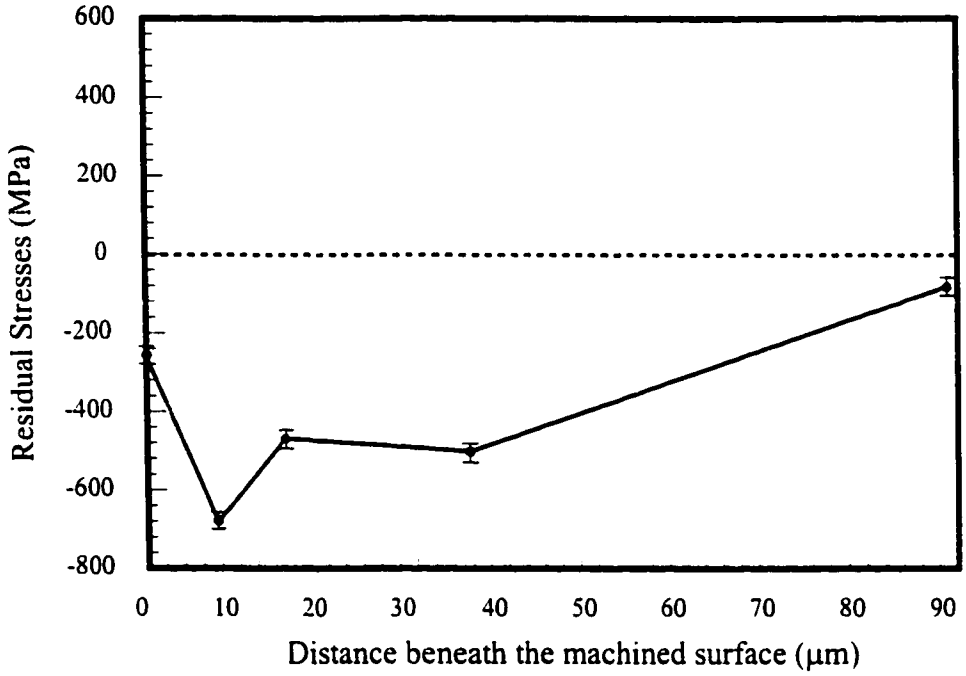

a- Sharp tool

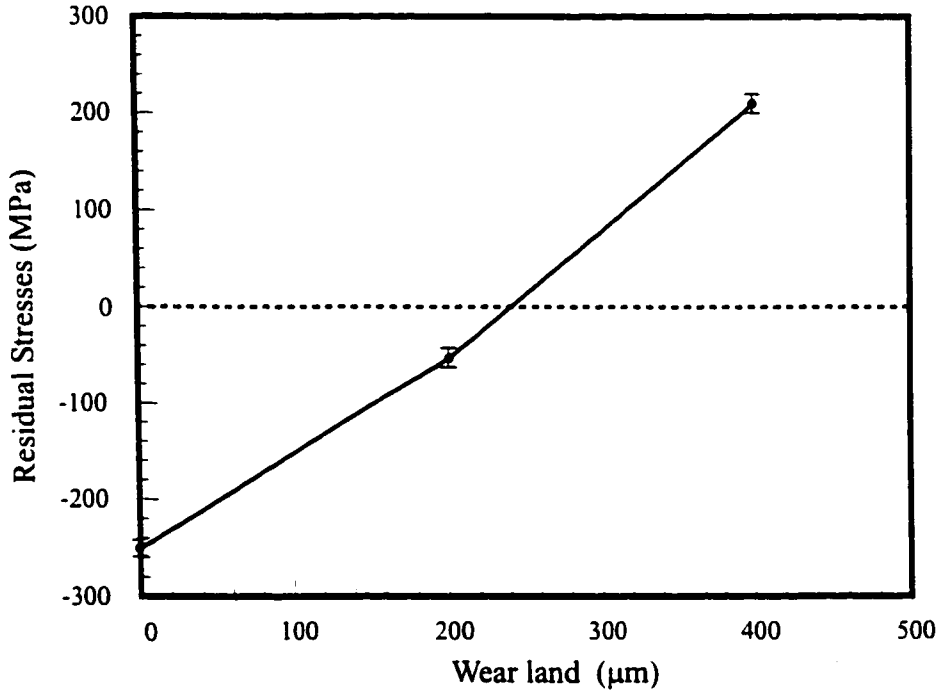

b- Worn tool

Fig. 4.8 Effect of tool wear on residual stresses
(V = 350 m/min, f = 0.1 mm/rev, d = 0.4 mm)

a higher level which will increase the residual tensile stress on the workpiece surface, as can be seen in Fig. 4.8-b.

4.5.5 Effect of edge preparation

Figure 4.9 shows the effect of nose radius on the surface residual stress of a machined component. Sharp cutting tools with two nose radii (1.2 and 1.6 mm) and three cutting speeds (140, 270 and 500 m/min) with feed, f = 0.1 mm, and depth of cut, d = 0.2 mm, are used. The obtained results show that increasing the nose radius reduces the tensile residual stress in the machined surface for all of the cutting speeds used. However, a reverse effect of tool nose radius is observed when using a honed cutting edge. Figure 4.10 shows the reverse effect of the nose radius when honed cutting tools with two radii (0.8 and 1.6 mm) were used. The cutting conditions are, cutting speed, V = 270 m/min, feed, f = 0.05 mm/rev, and depth of cut, d = 0.2 mm. When using a honed cutting edge the resultant effective rake angle increases. During machining of hardened steel with a high negative rake angle, the cutting temperature increases (El-wardany et al., 1996). In addition, increasing the nose radius decreases the resultant cutting temperature. This is attributed to the fact that for a small nose radius, the tool tip area available for heat conduction is decreased, promoting a local temperature rise. Hence, at the same cutting speed and nose radius, more tensile residual stress is generated at the machined surface when using a honed cutting tool. In turn, the reverse effect of the nose radius when using a honed cutting edge can be attributed to the combined effect of the nose radius and the rake angle on cutting temperature.

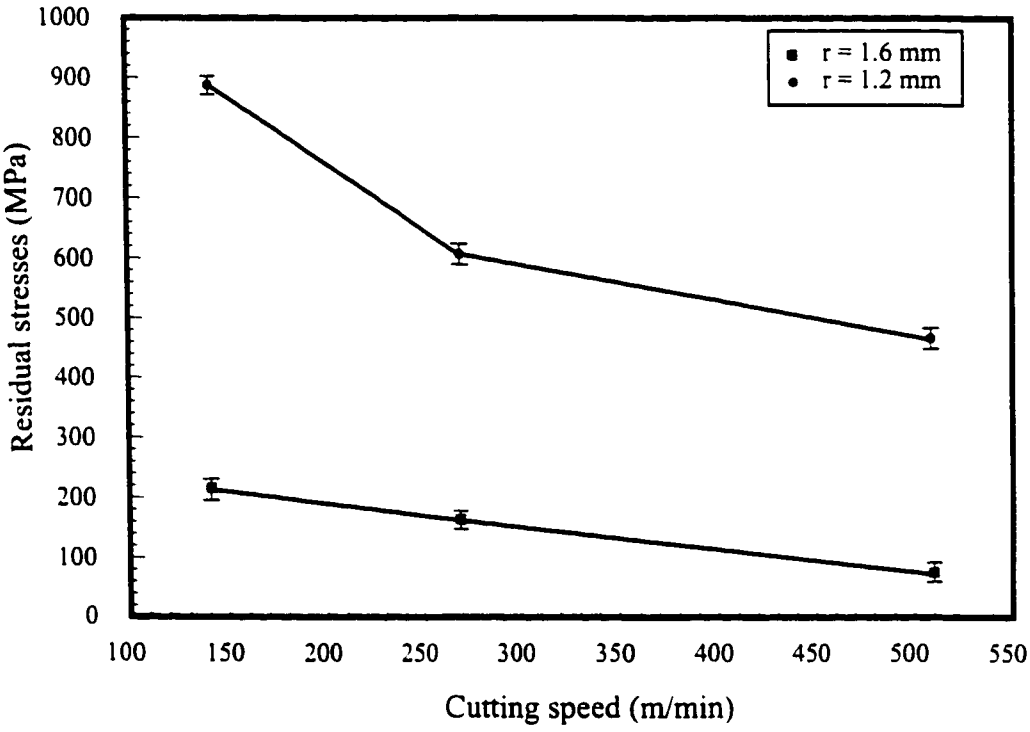

Fig. 4.9 Effect of cutting speed on surface residual stresses
(f = 0.1 mm/rev, d = 0.2 mm, sharp cutting edge)

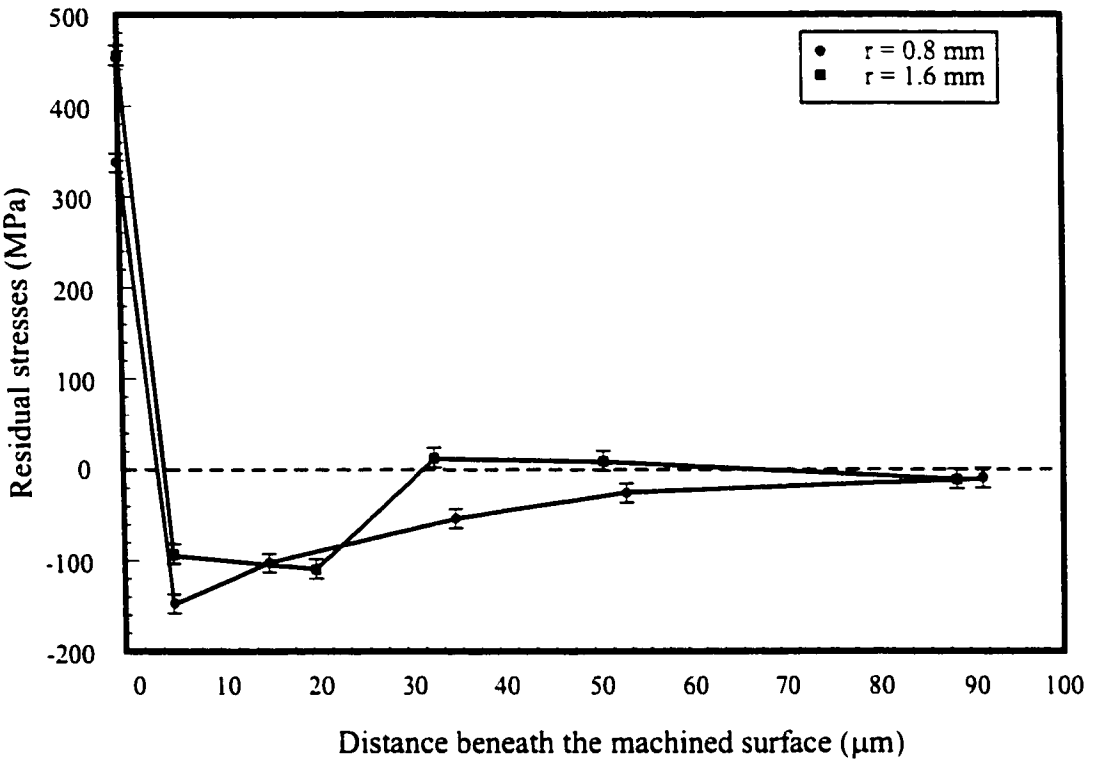

Fig. 4.10 Effect of nose radius on residual stresses distribution
(V = 270 m/min, f = 0.05 mm/rev, d = 0.2 mm, honed cutting edge)

CHAPTER 5

RESIDUAL STRESSES: FINITE ELEMENT ANALYSIS

5.1 Introduction

In the hard turning process, residual stresses can be generated by mechanical, thermal, and phase transformation changes. In practice, these sources combine together in different ways and, thus, generate a wide range of residual stress distributions beneath the machined surface.

The mechanisms creating residual stresses are rather complicated. The effect of different process parameters on residual stresses distribution beneath the machined surface are studied in chapter four. In this chapter, the aim is to investigate the influence of various

loading conditions on the residual stresses as well as the interaction between different loading types. A three dimensional finite element model is developed to predict the residual stresses distribution beneath the machined surface during hard turning. The finite element solution of the model is performed using a commercially available general purpose finite element program (Algor). In this model, the effect of cutting temperature on residual stresses distribution is included.

To include the thermal effect in the stress analysis, thermo-elasto-plastic analysis is required. Two analyses can be performed separately where the relevant results are transferred from the heat flow analysis to the thermo-elasto-plastic stress analysis. The stresses computed take into account the changes in material properties at elevated temperatures. The thermal regime is updated at all instances of time and the thermal strains are then introduced as loads for the stress analysis which exhibit either elastic or elasto-plastic behaviour for each time step.

5.2 Non-linear analysis

In a linear analysis, it is assumed that the displacements are infinitesimally small, the boundary conditions remain unchanged during loading, and the material is linearly elastic. In a non-linear stress analysis, the forces do not have a linear relation with displacement. In practice, the need for non-linear analysis arises from three major causes of non-linear behaviour as follow:

5.2.1 Material non-linearity

This type of non-linearity is considered when the material does not exhibit a linear stress strain relationship. In the machining process, plastic deformation is an example of the material non-linearity.

5.2.2 Geometric non-linearity

The problem of geometric non-linearity arises when a large deformation or strain exists during the analysis. The machining process is a typical example of a large deformation problem.

5.2.3 Boundary condition non-linearity

This non-linearity problem is considered in a situation where the stiffness matrix of an element changes as a function of some specified variable. An example of this type of problem is the gap element, which can be used to model the contact between two different surfaces. When the two surfaces are in contact, the stiffness matrix is positive and the forces are transferred through the gap element. When the surfaces are not in contact, the stiffness matrix of the gap element is zero and no forces are transferred.

In a typical finite element analysis, it is necessary to decide whether the problem falls into a linear or non-linear category. This will dictate which formulation will be used to describe the actual physical problem. Generally, using the most general large strain

formulation will give a correct answer. However, the use of a more restrictive formulation may be computationally more effective. In a typical machining process, material and geometric non-linearity are the most common sources of non-linearity. The non-linear nature of the relationship between stress and strain in the plastic deformation regime can be solved using an iterative process which solves a series of elastic problems (Bathe, 1996).

5.3 Thermo-elasto-plastic analysis

In elasto-plastic analysis the total strain can be divided into elastic and plastic components such that:

$$d\varepsilon_{ij} = d\varepsilon^{e}_{ij} + d\varepsilon^{P}_{ij} \qquad (5.1)$$

where $d\varepsilon_{ij}^{e}$ and $d\varepsilon_{ij}^{p}$ are the elastic and the plastic strain increment, respectively (Liu and Lin, 1985). In a thermo-elasto-plastic analysis, the effect of the elasto-plastic response due to the thermal loading is determined. The effect of temperature on the material properties is also included. The temperature field is calculated using the heat transfer module. Thus, the temperature value at each node is obtained. The thermal strains are then calculated at each node:

$$\varepsilon_{ii}^{th} = \alpha\,(T - T_R) \qquad (5.2)$$

where ε_{ii}^{th} are the normal strains, α is the thermal expansion coefficient, T is the nodal temperature, and T_R is the reference temperature. The computed thermal strains are added to the mechanical strains and, hence, the corresponding stresses are computed. The formulation of the thermo-elasto-plastic analysis is explained in Bathe (1996).

5.4 General description of the model

The finite element method was used as a tool to examine and predict the residual stresses which exist on the workpiece surface during hard turning of D2 tool steel. The main feature of the developed model can be summarized as follows:

5.4.1 Finite element mesh

A three dimensional finite element mesh is generated as shown in Fig. 5.1. The major features and assumptions of the model are:

1- The workpiece was modelled as a three dimensional structure. The diameter of the workpiece varied between 70 and 100 mm, while the length of the bar was 150 mm.

2- In this representation of the bar turning process, the chip was assumed to be already formed when the finite element network was drawn. The geometry of the chip formation was controlled by the existing conditions of the strain and the temperature which were, in turn, controlled by the cutting conditions.

3- A total of 7072 isoparametric, eight-node brick type elements were used to model the chip and the workpiece. The size of the element was based on a criterion such that

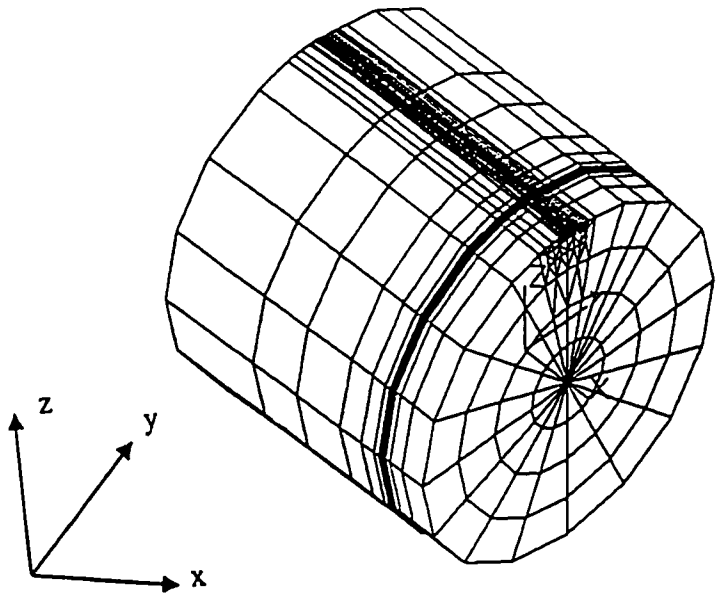

Fig. 5.1 Mesh for the workpiece and the chip

the aspect ratio of the largest dimension in one direction to the smallest dimension in the other direction of an element should not exceed a fixed upper limit.

4- Amongst the 7072 elements, the area of concern was on the workpiece surface near the tool path. Therefore, the model consisted of a variable mesh with the greatest net density in the region of the tool-workpiece interface. Finer meshes were necessary in this area to take into account the surface deformation during the cutting, and the anticipated large stress and strain gradients as shown in Fig. 5.2

5- The cutting tool material is much harder than that of the workpiece. Therefore, it is reasonable to consider the cutting tool as a rigid body and remove it from the model. However, the contact conditions between the tool, the chip, and the workpiece were included as boundary conditions.

5.4.2 Loading

Both mechanical and thermal loads are very important in understanding the mechanism of residual stresses during machining. Therefore, in this model, both the mechanical loading and the thermal loading were considered as the main causes of residual stresses during machining. The developed model takes into consideration the effect of the variation of the tool geometry along the active part of the tool. This variation involves changing the area of force and temperature application and their distribution on the chip/tool/workpiece interface.

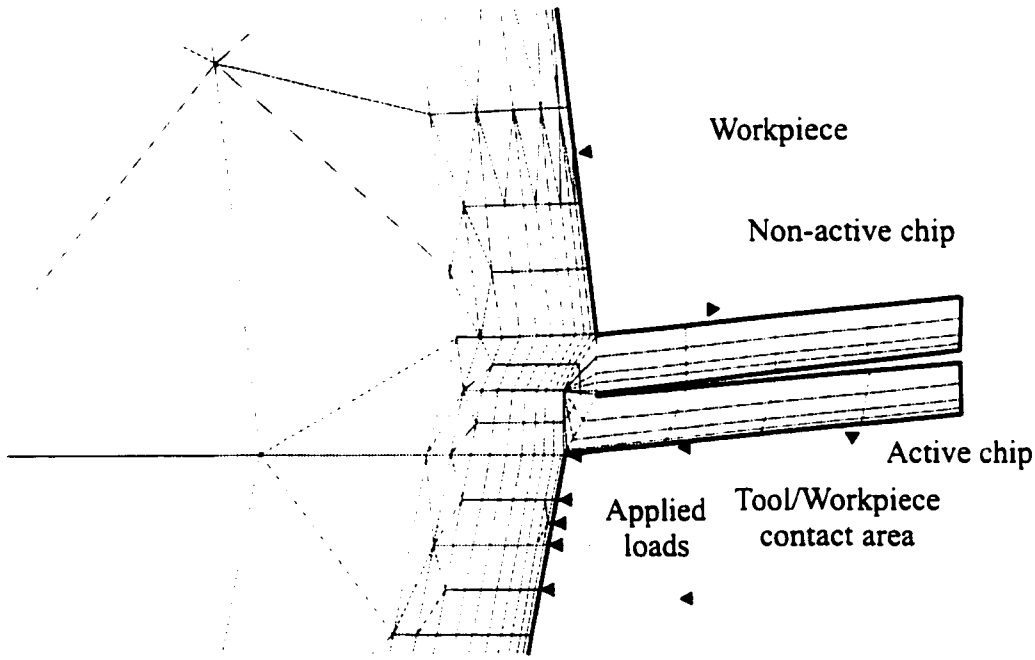

Fig. 5.2 Mesh in the vicinity of cutting

5.4.2.1 Mechanical loading

As a consequence of the properties of the high speed machining of hardened steel, distinct wear types exist on the PCBN tool. Because of the low depth of cut used in this investigation (see chapter 4) and the large nose radius of 1.2 mm, it is expected that all changes in tool conditions take place at the tool nose. Therefore, the loading distribution will be concentrated on the active part of the cutting edge at the interface zone between the chip/tool/workpiece. The external loads were the measured force components. Figure 5.3-a shows the local configuration of the cutting tool and the tool-workpiece interface. Figure 5.3-b shows the arrangement in the interference zone with wear land and nose wear on the tool during steady state turning. The cutting force distribution in the X, Y, and Z directions are assumed to be a function of the variation of the undeformed chip thickness on each plane along the active cutting edge. The force distribution is applied to the workpiece at the nodes representing the contact area between the tool and the workpiece.

5.4.2.2 Thermal loading

The temperature effect cannot be ignored in the case of calculating residual stresses. It has been observed in this study that the temperature gradients inside the workpiece significantly affect the distribution of the residual stresses underneath the workpiece surface. The temperature distribution along the chip/workpiece surfaces was first calculated (using a heat transfer finite element module) and it was then used for the thermo-elasto-plastic stress analysis. It should be noted here that using a semi-infinite model for the workpiece gives an

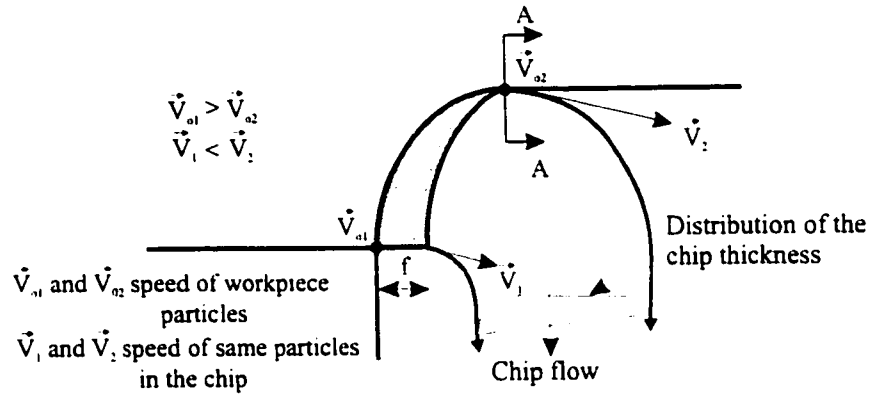

a- Local configuration of the tool and its interface with the workpiece

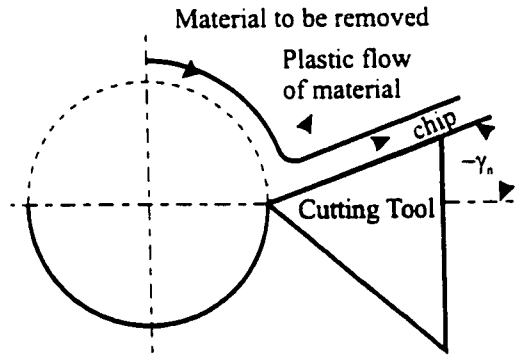

Section A-A for sharp tool

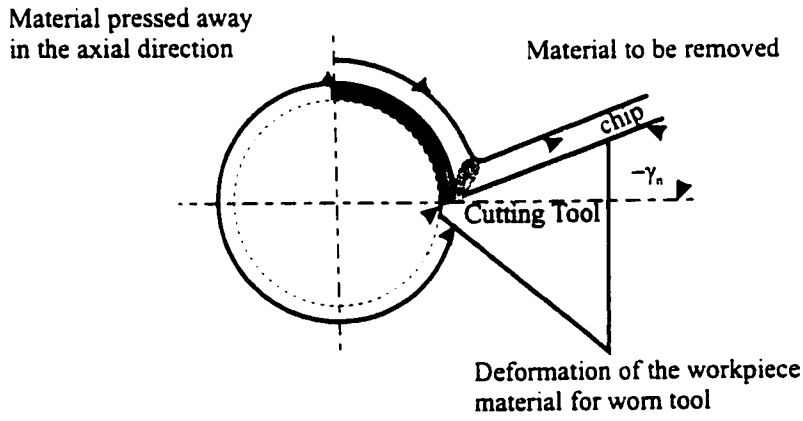

Section A-A for worn tool

b- Interface zone and workpiece

Fig. 5.3 Effect of tool wear on the tool workpiece interface

inaccurate result for the predicted residual stresses, because of incorrect estimations of the temperature gradients.

The heat flux entering the workpiece and the chip was estimated based on the measured cutting forces. Because of the large plastic deformation involved in machining, it can be assumed that all of the energy required to deform the material is converted into heat. As shown in Fig. 5.4-a, heat energy may enter the workpiece from two areas of the cutting zone. Plastic deformation and friction on tool flank-machined workpiece interfaces are the main heat sources during the cutting process. At any instant, it is assumed that the temperature along the shear plane T_{sh} is uniform:

$$T_{sh} = \frac{A_s F_s V_s}{\rho c V f d} \tag{5.3}$$

where F_s and V_s are the shearing force and velocity, respectively, A_s is the percentage of the energy which is converted into heat (0.85 to 0.95), ρc is the volumetric specific heat, V is the cutting speed, f is the feed, and d is the depth of cut (Maekawa et al., 1996). If the tool has some wear land, a second heat source results from friction between the tool flank face and the workpiece is added. The heat flux on the flank face can be expressed in the following way:

$$q_{fw} = 2\mu \; m \; F_t \; V_t \; / \; A_t \tag{5.4}$$

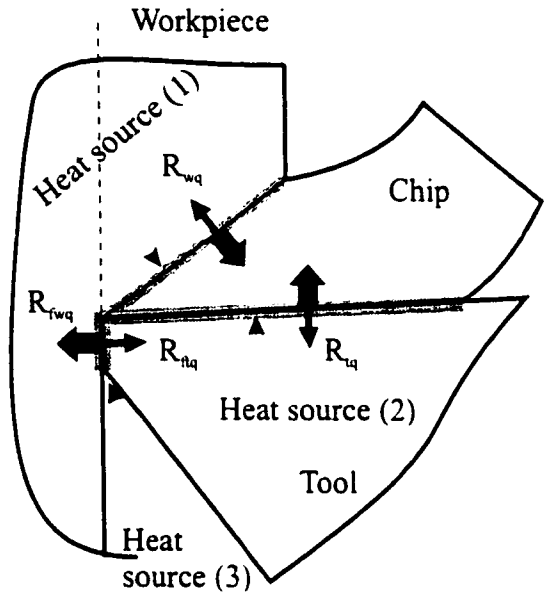

a- Sources of heat generated

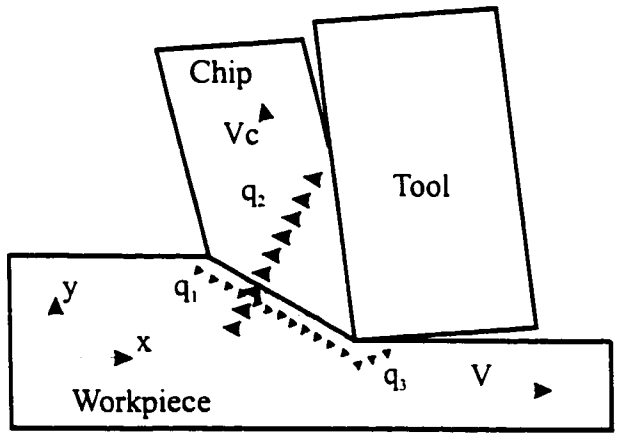

b- Distribution of heat generated

Fig. 5.4 Heat generation during hard turning

where F_t and V_t are the radial force and the velocity along the flank face, respectively, μ is the coefficient of friction on the flank face, m is a heat partition coefficient between the tool and the workpiece, and A_t is the wear land area. From Fig. 5.4-a, the main heat source due to friction is generated at the chip/tool interface. The heat flux of the friction heat source q_f is determined as follows:

$$q_f = F_f \, V \tan\varphi \, / \, A_f \qquad (5.5)$$

where F_f and V are the feed force and the cutting speed, respectively, φ is the shear angle and A_f is the actual tool-chip contact area (Trent, 1991). Figure 5.4-b shows the assumed distribution of the heat flow rate along the shear plane (Maekawa et al., 1996), and the chip-tool and tool-workpiece interfaces (Tlusty and Masood, 1978; Maekawa et al., 1996). Since in hard turning "saw toothed" chips are produced partly by crack initiation and propagation, as well as plastic deformation, the temperature T_{sh} was distributed uniformly only along the portion corresponding to the plastic deformation along the shear plane. The value of this portion depends on where the crack ceases during the chip formation process (Elbestawi, et al., 1996). This value was determined experimentally and was found to be approximately 0.4 of the undeformed chip thickness. The temperature and heat flux were applied on each plane along the active cutting edge.

5.4.3 Boundary conditions

1- The workpiece surface, which was fixed by the chuck, was constrained in all six degrees of freedom, while the other side of the workpiece, which was fixed by the live centre, was constrained against the three rotational and longitudinal motions.

2- At both ends of the workpiece, the elements were at room temperature. The mechanical properties of the workpiece were included in the model as temperature dependent.

3- The effect of tool conditions (i.e, sharp or worn) on the generated residual stresses has been included in the model by changing the area of force and temperature application and their distribution on the chip/tool/workpiece interface as a function of tool wear (Maekawa, et al., 1996).

4- Convection heat loss from the part on the surface (at positions other than the chip/tool/workpiece contact area) was estimated using the empirical formulas for rotating cylinders obtained by Mills (1992). His formula gives only an approximate average value for the entire surface, which is found to be 10 $W/m^2\,^{\circ}C$. The heat transfer coefficient depends primarily on the diameter of the workpiece and the rotational speed. The convection fluid was air.

5- The model was constructed to utilize the concept of the historical strain field by deactivating the elements in the model that do not, in reality, exist. These deactivated elements were constrained at room temperature through the finite element analysis and a very low yield stress. In the next step, the chip elements

which have been active will be deactivated and so on. The output from the previous run will then be used as a preload in the next step for predicting the loading history on each node.

5.4.4 Material properties

In modelling residual stresses, the effect of plastic flow on the cutting process must be considered. The workpiece material property includes information beyond the elastic region which is also necessary for the non-linear finite element analysis. In addition, the effect of the temperature on the mechanical properties is included. The variations in material properties with temperature considered for both the ASTM 5115 steel and D2 tool steel are presented in Table 5.1.

Table 5.1 Property variations of D2 tool steel and case hardened steel ASTM 5115 with temperature increases

Properties	Case hardened ASTM 5115 steel			D2 Tool Steel		
Temperature	20	500	1000	20	500	1000
Thermal conductivity k (W/m °C)	51.5	43	27	20	23	26
Specific heat J/kg °C	485	-	-	460	-	-
Coefficient of thermal expansion	-	11.2	12	-	10.8	10.2
Density (gm/cm^3)	7.8	7.72	7.68	7.74	7.6	7.4
Young modulus E (GPa)	206	180	130	193	173	120
Yield stress Y (MPa)	490	280	150	150	110	50
Work hardening modulus H (GPa)	2.06	1.8	1.3	1.82	1.67	1.19

The maximum temperature reached during high speed hard turning of D2 tool steel can be over 1000 °C. The incorporation of temperature dependant material properties leads to a highly non-linear thermal problem which requires efficient incremental iterative numerical procedures.

5.5 Finite element solution

A commercially available general purpose finite element program (Algor) is used to perform the solution for the presented model. The main characteristics of the finite element modelling and analysis are as follows:

1- An updated lagrangian type of formulation is chosen for this analysis since it is more suitable for solving the large strain analysis of elastic-plastic deformation.

2- The concept of historical strain field was used to calculate the residual stresses in the machined workpiece. Using the thermo-elasto-plastic finite element, the instantaneous strain field of the workpiece was obtained. During machining, the mechanical and thermal loads moved along with the tool. This meant that the strain field that was produced by cutting moved progressively along with the tool. Figure 5.5 represents a schematic diagram for the concept of historical strain field. During machining, a particle (A) at a certain depth beneath the machined surface is considered. This particle will experience all strain field components at the same depth throughout its path. The historical strain field of each point differs from the

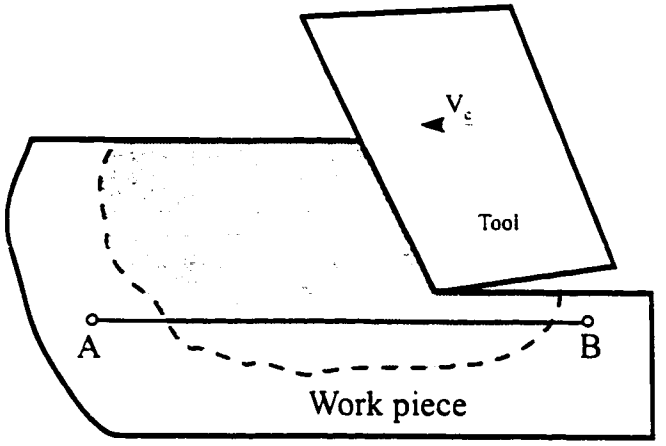

a- Instantaneous strain field around the cutting edge

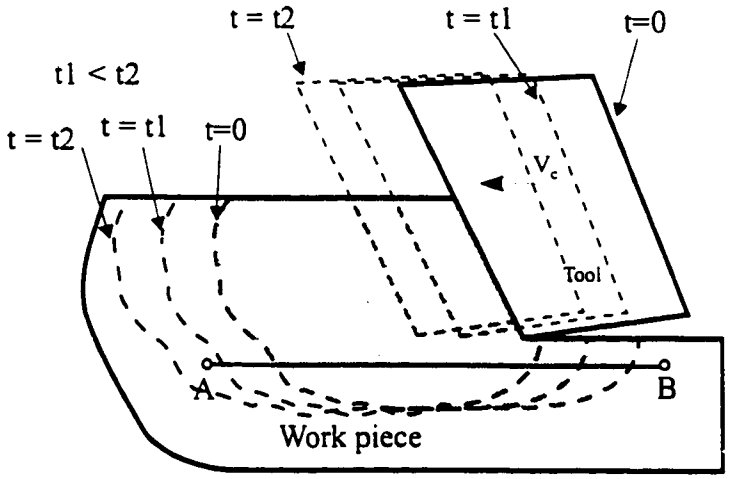

b- Time dependent strain field around the cutting edge

Fig. 5.5 Historical load during machining

instantaneous strain field produced by static loads and is determined from the instantaneous strain field using step by step loading (Lin et al., 1991).

3- Displacements were determined at all nodal points, and the Lagrangian strain components were calculated. Stress components, as well as the principal stresses, the maximum shear stresses, and the principal stress directions at the integration points, were then determined.

4- One hundred iterations were allowed to meet a given convergence criterion.

5- The cutting process was represented by fifty incremental loading steps, with the last loading step being the experimentally determined steady state tool force. Another fifty incremental steps were used for the unloading process (releasing the cutting forces and cooling the workpiece to the room temperature) to predict the residual stresses distribution.

During the finite element solution of the model the sensitive time step required for accurate and stable convergence cannot be easily identified because of the high non-linearity problem. A solution to this problem is to use a single, small time/load step for the entire time history. However, this solution is computationally not efficient to accommodate this problem. The restart analysis can be used to continue an unsuccessfully terminated job from the time/load step before the execution is terminated. If the job stops prematurely at time t_n or load P_n, the restart analysis with another time/load step from time t_{n-1} or load P_{n-1} is performed using a reasonably smaller time step.

5.6 Model verification

To insure the validity of the developed model, the predicted results are compared with the experimental results for two different kinds of hardened steel, namely, case hardened steel and tool steel.

5.6.1 Case hardened steel

The modelling technique is verified by comparing the predicted residual stresses with those obtained experimentally and presented by Tönshoff et al.(1995a, and b) as shown in Fig. 5.6. The material used in this set of tests was case hardened 16 Mn Cr (ASTM 5115) steel of 60-62 HRc. PCBN tools were used for machining. The cutting conditions were: cutting speed V = 200 m/min, feed f = 0.1 mm/rev, depth of cut d = 0.2 mm and tool nose radius r = 1.2 mm. The magnitude of the cutting forces used in the model is obtained from the same publication (Tönshoff et al., 1995-a). The cutting temperature is calculated as a function of the cutting conditions. Two cases are investigated. The first case is concerned with residual stresses induced on the surface during hard turning with a tool having 0.05 mm nose wear, (Fig. 5.6-a), and the second case involved a worn tool having 0.15 mm nose wear, (Fig. 5.6-b). A comparison of the theoretical and experimental results indicates that the proposed model can predict within an error of 12% the values of the residual stresses on the workpiece surface. It also shows the position and magnitude of the maximum compressive stress beneath the surface. The predicted and measured residual stresses show the existence of tensile stresses on the workpiece surface. The x-ray diffraction

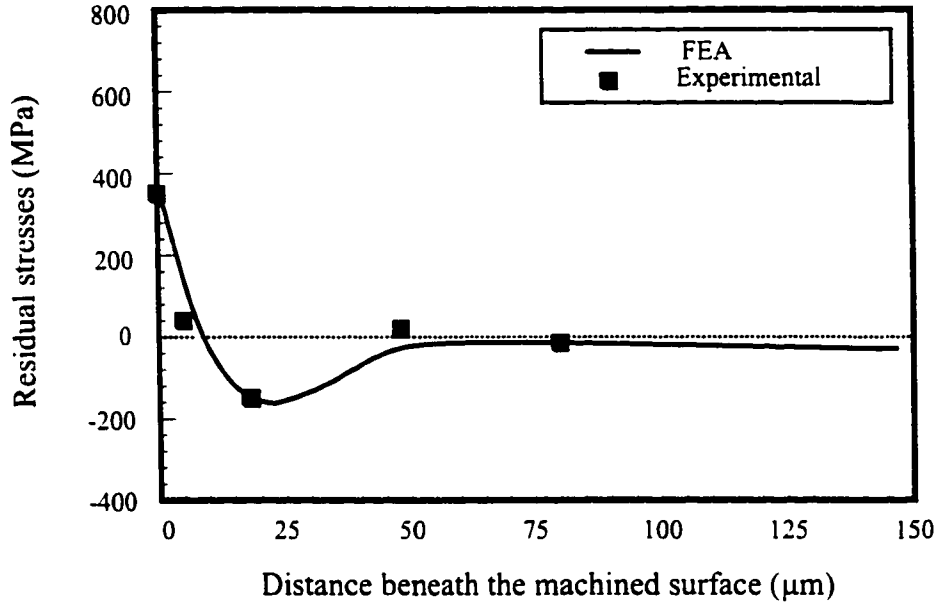

a- 0.05 mm nose wear

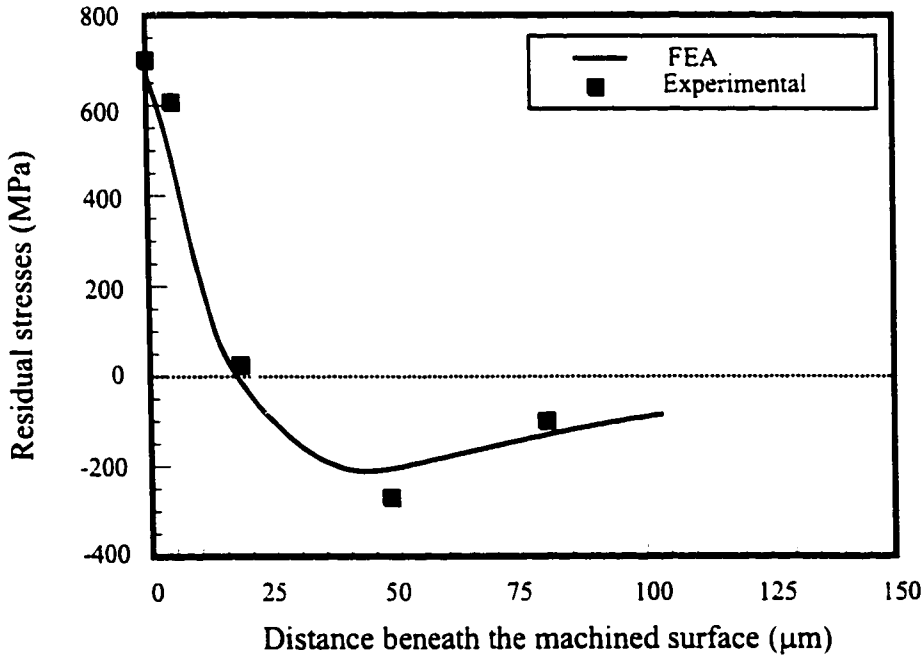

b- 0.20 mm nose wear

Fig. 5.6 Effect of tool wear on distribution of residual stresses
(V = 220 m/min, f = 0.1 mm/rev, d = 0.2 mm)

measurements show that tensile residual stresses with a magnitude of 360 MPa and 670 MPa are produced on the surface when tools having 0.05 mm and 0.2 mm nose wear, respectively, were used. The predicted values of these residual stresses are 400 and 600 MPa respectively. Figure 5.7 shows a comparison between two residual stresses distributions obtained using tools having different levels of nose wear. As can be seen in Fig. 5.7, tool wear has a great effect on the distribution of residual stress beneath the surface. The high temperature generated during cutting with a worn tool is the main reason for the increase in the tensile residual stress on the surface and sub-surface of the workpiece.

5.6.2 Tool steel

Finite element analysis is also performed in order to simulate the process under cutting conditions identical to those used in the experimental work presented in chapter four. The residual stresses were predicted for two different cutting conditions. The workpiece material is D2 tool steel. The cutting speed V = 350 m/min, feed f = 0.1 mm/rev, tool nose radius r = 1.2 mm, and artificial nose wear on the tool was 0.2 mm. Two depths of cut were implemented (0.2 and 0.6 mm). The magnitudes of the cutting forces applied in the model were determined experimentally, and the heat generated was calculated. The measured cutting force components were as follows; for a depth of cut 0.2 mm, Fx = 70 N, Fy = 200 N and Fz = 124 N, for a depth of cut of 0.6 mm, Fx = 100 N, Fy = 250 N, Fz = 185 N. The heat transfer module was first run to determine the temperature isotherms in the workpiece.

Figure 5.8 shows the effect of an increase in the depth of cut on the temperature

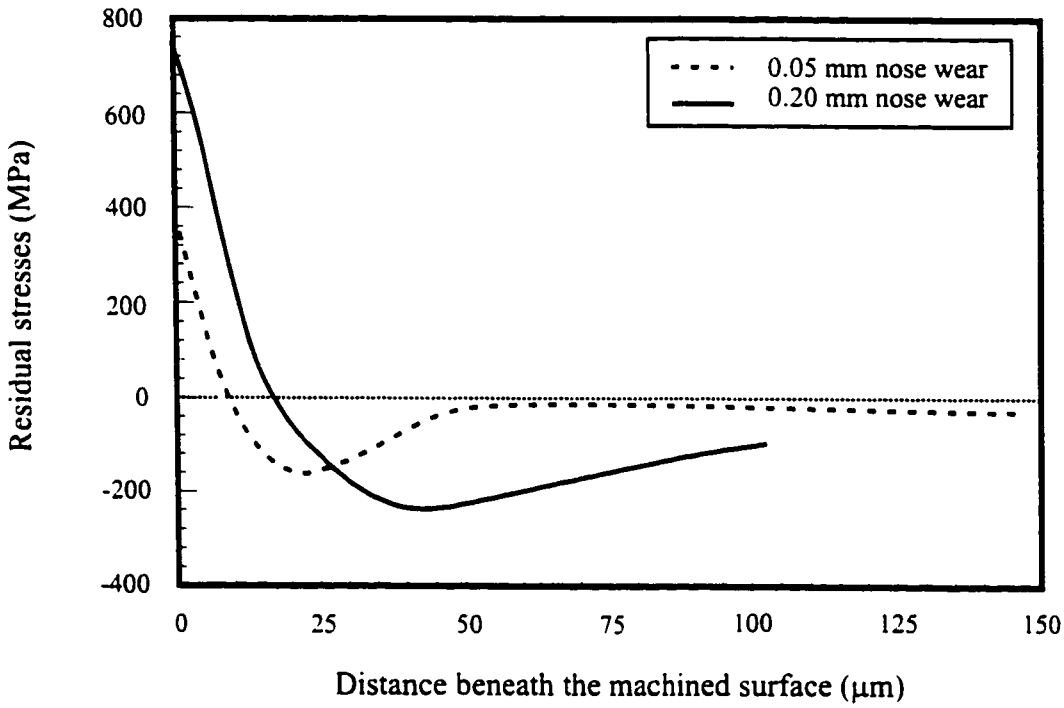

Fig. 5.7 Effect of tool wear on the predicted distribution of residual stresses
(V = 220 m/min, f = 0.1 mm/rev, d = 0.2 mm)

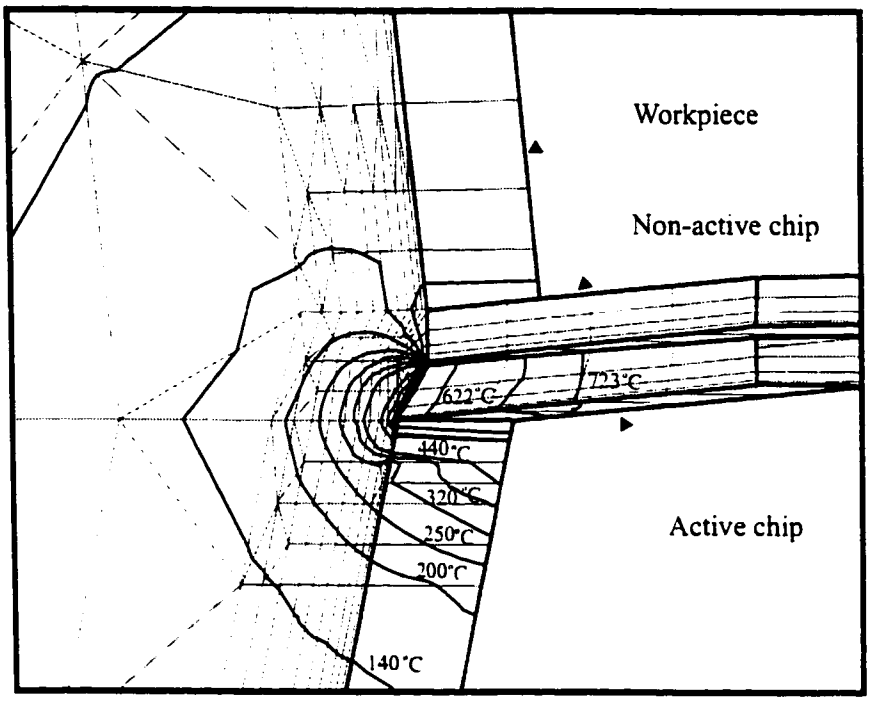

a- Temperature isotherms at d = 0.2 mm

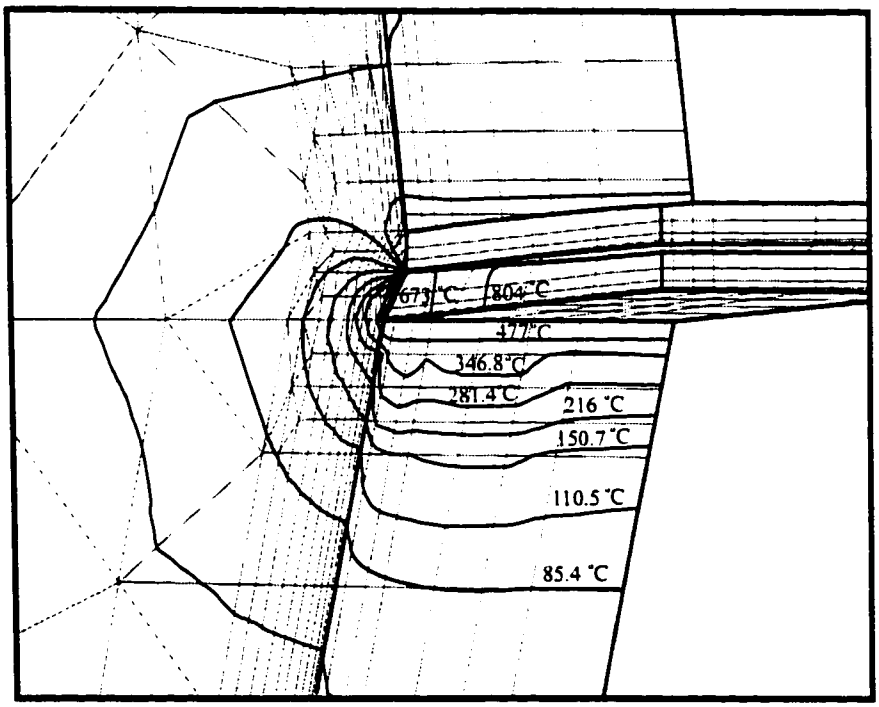

b- Temperature isotherms at d = 0.6 mm

Fig. 5.8 Effect of depth of cut on temperature distribution

isotherms during the steady-state cutting process. Figure 5.8-a shows the contours of temperature distribution during the steady-state cutting process when the depth of cut was 0.2 mm. The region with the highest temperature occurs at the area of contact between the tool and the chip. However, it is more concentrated at the tool nose in the vicinity of cutting. The highest temperature calculated for the cutting conditions illustrated in the figure was 746 °C. Also, a steep temperature gradient is observed around the zone near the tool tip. Figure 5.8-b shows the contour of temperature distribution during the steady-state cutting process when the depth of cut was 0.6 mm. The same isothermal distribution as that in Fig. 5.8-a was also observed in this case. However, the temperature gradient in this case was steeper, which is expected to influence the distribution of the residual stresses beneath the machined surface.

Figure 5.9 represents a comparison between the measured and predicted residual stresses in high speed machining of D2 tool steel. Figure 5.9-a represents the case when the depth of cut was 0.2 mm. A fair agreement between the predicted and measured values can be observed. The error in predicting the tensile residual stress on the machined surface was around 10 %. The deviation between the measured and the predicted values of residual stresses beneath the surface can be attributed to the variations between the thermal dependent material properties used in this analysis and the actual values. This variation will affect the temperature gradients. It is worth mentioning here that another source of residual stresses, such as phase transformation, was not considered in the presented model. Figure 5.9-b shows a good agreement between the predicted and measured residual stresses when the

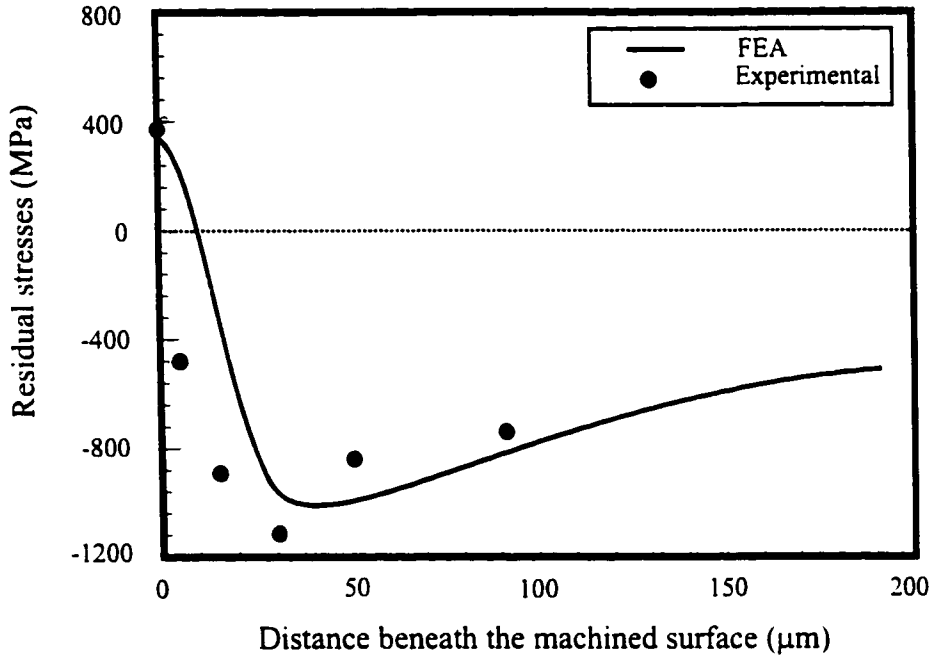

a- Residual stresses distribution at d = 0.2 mm

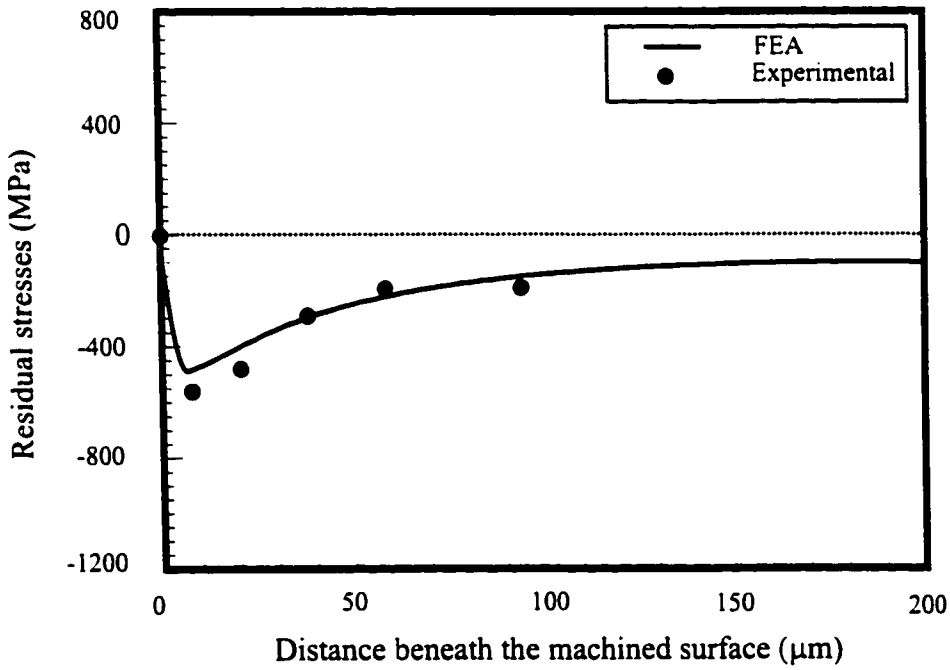

b- Residual stresses distribution at d = 0.6 mm

Fig. 5.9 Effect of depth of cut on residual stresses distribution
(V = 350 m/min, f = 0.1 mm/rev)

depth of cut is 0.6 mm. Figure 5.10 shows a comparison between the predicted residual stresses distributions at two different levels of depth of cut. The effect of depth of cut on residual stress distribution is explained in chapter four.

5.7 Effect of thermal and mechanical loads

Figure 5.11-a shows the residual stresses obtained from finite element analysis by applying different thermal loads in the vicinity of cutting. The cutting temperature generated was in the range of 200 to 1200 °C. The effect of the thermal load on the predicted residual stresses is very pronounced as the cutting temperature increases from 400 to 800 °C. The predicted tensile residual stress seems to increase slightly after 800 °C. This result is attributed to the inclusion of the material properties as a function of the cutting temperature in the model developed. These results show that the cutting temperature has a detrimental effect on the residual stress induced on a surface produced at a high cutting speed in a certain range. Beyond this range, a slight increase in the residual stress can be observed. Figure 5.11-b shows that mechanical load induces compressive stresses on the workpiece surface. A high mechanical load results in higher values of compressive stress.

It is obvious from the previously obtained results that a high cutting temperature induces tensile residual stresses in the surface produced if the mechanical load is small. Mechanical load can be increased by increasing the chip load (i.e, increasing the depth of cut). Thus, selecting specific cutting conditions would lead to a surface free of unfavourable tensile residual stresses.

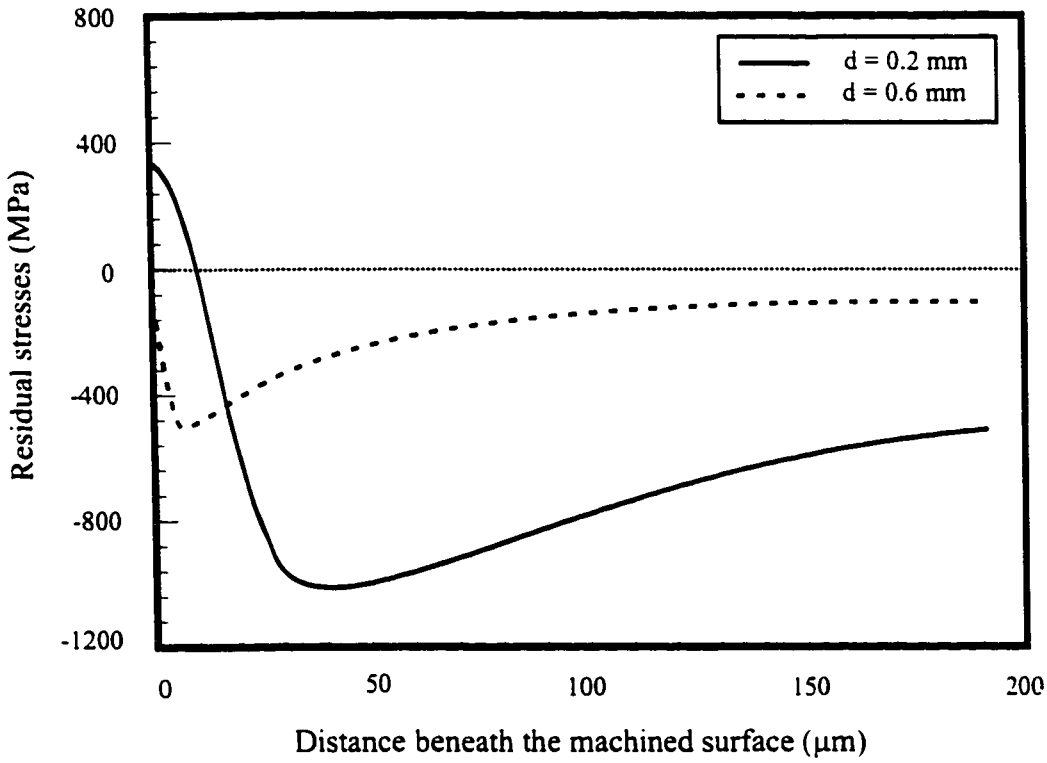

Fig. 5.10 Effect of depth of cut on the predicted residual stresses distribution
(V = 350 m/min, f = 0.1 mm/rev)

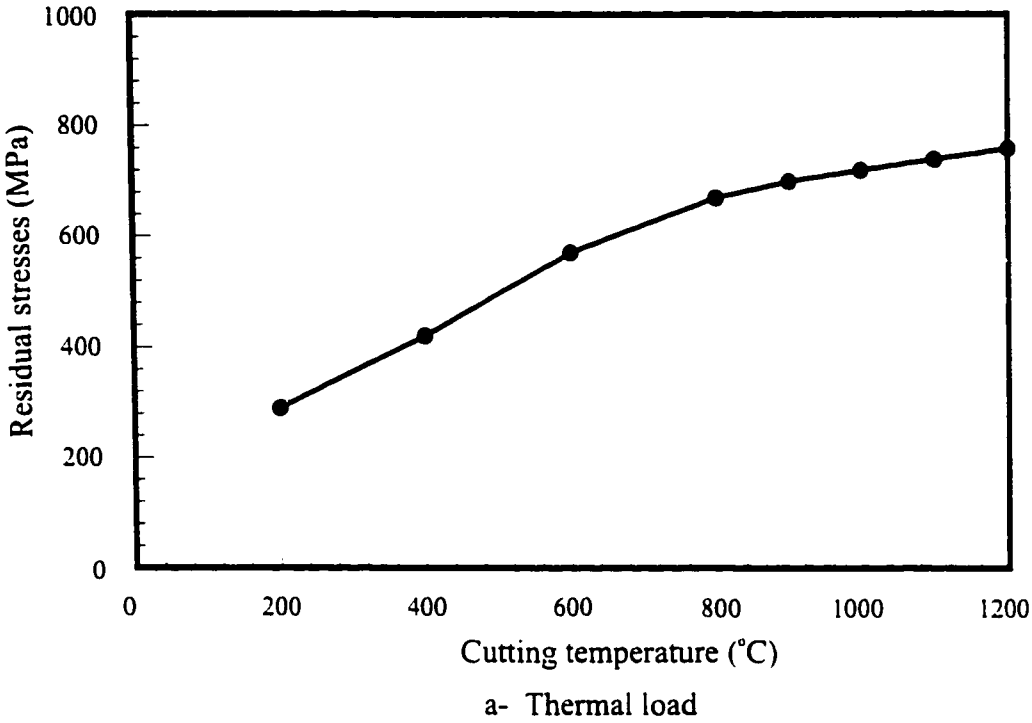

a- Thermal load

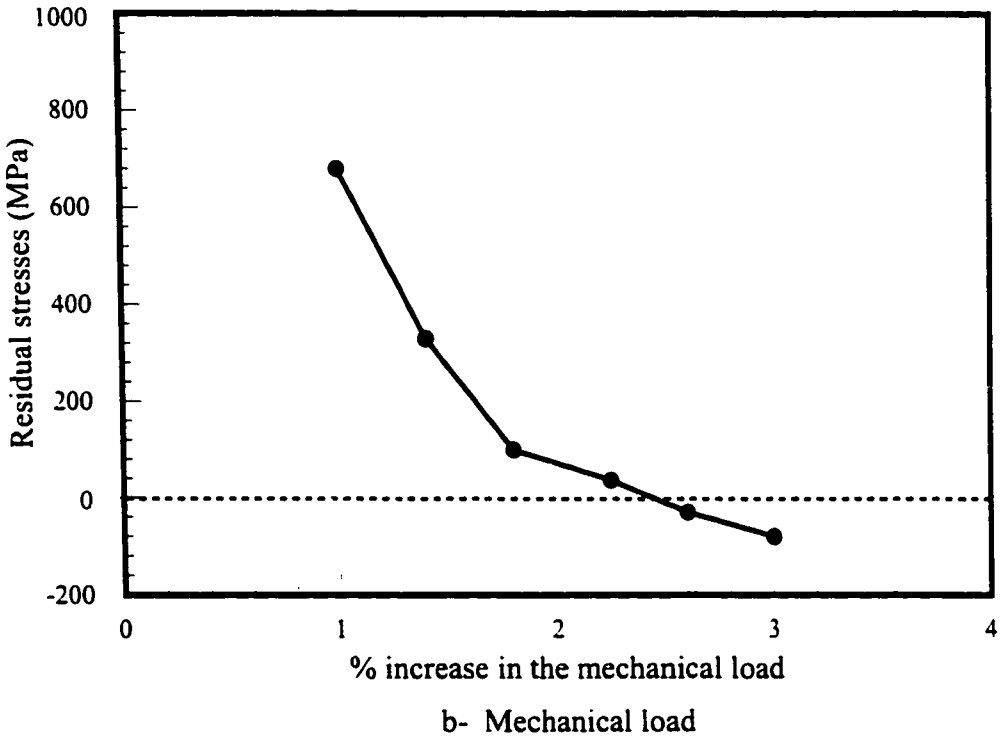

b- Mechanical load

Fig. 5.11 Effect of thermal and mechanical loads on residual stresses
(V = 220 m/min, f = 0.1/rev, d = 0.2 mm)

CHAPTER 6

SURFACE AND SUB-SURFACE DEFORMATION

6.1 Introduction

The basic knowledge of surface and sub-surface conditions could lead to the generation of remedial machining procedures that enhance the component life. Therefore, it is critical to control the surface quality and integrity of the machined component. Several studies were carried out in the area of high speed machining of dies and moulds (Poggie and Wert, 1991; Ikeda et al., 1992; Rigby, 1993; Abráo et al., 1995; Elbestawi et al., 1997), however, systematic evaluation of surface integrity is still required.

In this chapter, the effects of edge preparation and cutting conditions on surface and

sub-surface damages is investigated. The machined surface and sub-surface are examined using optical and scanning electron microscopy. The thermally induced white layer is also investigated under different cutting conditions. Different types of surface and sub-surface damage are also observed.

The phenomenon of material side flow represents an important aspect of machined surface quality during hard turning. In this chapter, an experimental study is also performed to investigate the main features of this phenomenon. Two possible mechanisms for material side flow are investigated. In the first one, the material is squeezed between the tool flank face and the machined surface when chip thickness is less than a minimum value. In the second mechanism, the plastified material in the cutting zone flows through the worn trailing edge to the side of the tool. Both of these mechanisms can exist simultaneously. The results obtained from surface examination show a strong correlation between edge preparation and material side flow. An increase in the tool nose radius results in a remarkable increase of material side flow.

6.2 Experimental procedure

Dry hard turning tests were conducted on a D2 tool steel workpiece. The workpieces were received in the form of bars having a diameters of 70-100 mm, a length of 150-200 mm and a hardness of 62 Rc. Cutting tests were performed using PCBN cutting tools with -6 degree rake angle on a standard modern 10 HP CNC lathe. Table 6.1 shows the chemical composition of the material used.

Table 6.1 Chemical composition of D2 tool steel (wt/%)

C	Mn	Si	Cr	Mo	V	Others
1.5	0.25	0.3	12	0.8	0.9	84.25

Cutting conditions and tool specifications are presented in Table 6.2. The effect of cutting speed, tool wear and different edge preparations on the surface and sub-surface deformation were investigated.

Table 6.2 Cutting conditions and tool specifications for surface integrity investigation

Process Parameters	Cutting Range			
Cutting speed, V (m/min)	140	270	350	500
Depth of cut, d (mm)	0.2	0.4	0.6	---
Feed, f (mm/rev)	0.05	0.1	0.2	---
Tool nose radius, r (mm)	0.8	1.2	1.6	---
Edge preparation	Sharp	Chamfered (20°/0.1mm)	Honed (0.0125 mm)	---

After each cutting test, the cutting edge condition was examined using a tool maker's microscope to measure the level of tool wear. Cutting forces were measured using a three component piezoelectric dynamometer. To examine the machined surface and sub-surface, small specimens of 10x10x30 mm were cut from the workpiece and cleaned using methyl alcohol. The specimens were sectioned from the workpiece in a manner which leads to the least possible distortion or burning. A high speed diamond saw was used. Care

was taken during preparation to protect the edge of the machined surface by preplating the specimens with nickel phosphate. The specimens were mounted in a special mould (mixture of epoxy resin, hardener, and aluminum oxide filler to retain the specimen edge roundness during further processes), ground, polished and etched for 10 seconds in an iron-picric-chloride solution (4 gm picric acid, 2 gm Fe Cl_3 and 5 ml HCl in 120 ml ethanol), then another etchant (2% nital solution) for about 3 seconds. The specimens, surfaces and sub-surfaces were then examined using scanning electron microscopy.

To study the phenomenon of material side flow, an experimental work was conducted to determine the effect of edge preparation, nose radius, feed, and tool wear on surface material side flow during hard turning. Dry hard turning tests were carried out using a 10 HP standard modern CNC lathe. Bars of nitride case hardened steel AISI 4615 (60 Rc), with 49 mm diameter, and 265 mm length were used. All cutting tests were conducted using BZN 8100 PCBN inserts with zero degree clearance angle, and -6 degrees rake angle. Different cutting edge preparations were used including sharp, honed and chamfered with three different nose radii tools. Table 6.3 shows the different levels of the independent cutting parameters used in this investigation. The flank wear level was measured after each cutting path using a tool maker's microscope. In addition, the cutting tool inserts were examined using a Scanning Electron Microscope (SEM). Cutting forces were measured using a three axis piezoelectric dynamometer. Samples of the chips were collected after each cutting test and examined using SEM. Moreover, specimens were cut from each machined surface and examined using SEM.

Table 6.3 Levels of independent parameters used for material side flow investigation

Process Parameters	Cutting Range		
Cutting speed, V (m/min)	250	---	---
Depth of cut, d (mm)	0.125	---	---
Feed, f (mm/rev)	0.05	0.1	---
Tool nose radius, r (mm)	0.4	1.2	3.2
Edge preparation	Sharp	Chamfered (20°/0.1 mm)	Honed (0.0125 mm)

6.3 Surface roughness

The effect of cutting speeds on the surface roughness produced was found to be negligible. These results were confirmed earlier (Oishi, 1995). Figure 6.1-a shows traces of the profile of the finished surface produced at a depth of cut of 0.4 mm and different feeds, when using an artificially worn tool with a wear land of 0.2 mm. As expected, increasing feed results in increasing the resulting surface roughness. The Ra values are found to be 0.3, 0.5, and 1 μm for feeds of 0.05, 0.1 and 0.2 mm/rev, respectively. On the other hand, increasing the depth of cut is found to have no significant effect on the surface roughness produced (Fig. 6.1-b). In general, the measured Ra is between 0.4 and 0.5 μm for the depths of cut ranging between 0.2 to 0.6 mm. The tool wear land in these cases is 0.2 mm.

Figure 6.1-c shows traces of the profile of the finished surface produced at a depth of cut of 0.4 mm, a feed of 0.1 mm/rev, and different tool wear lands. As can be seen, the surface roughness (Ra) produced by a sharp tool is 0.2 μm (Fig. 6.1-c). For a tool wear land

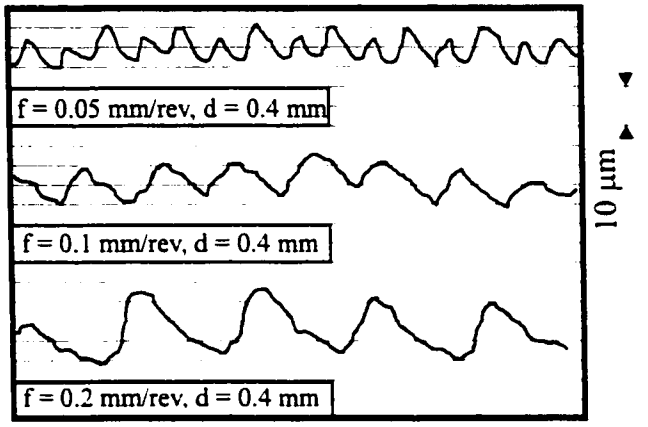

a - Effect of feed

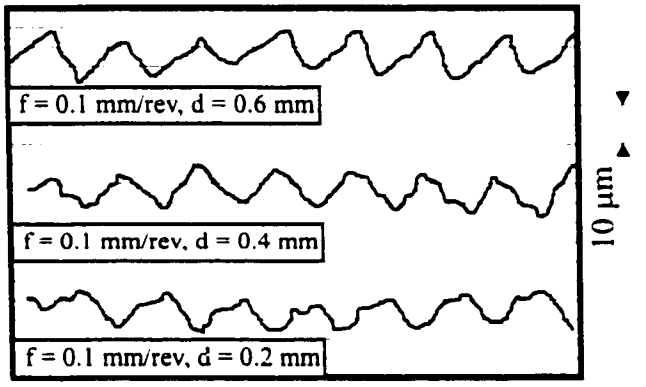

b- Effect of depth of cut

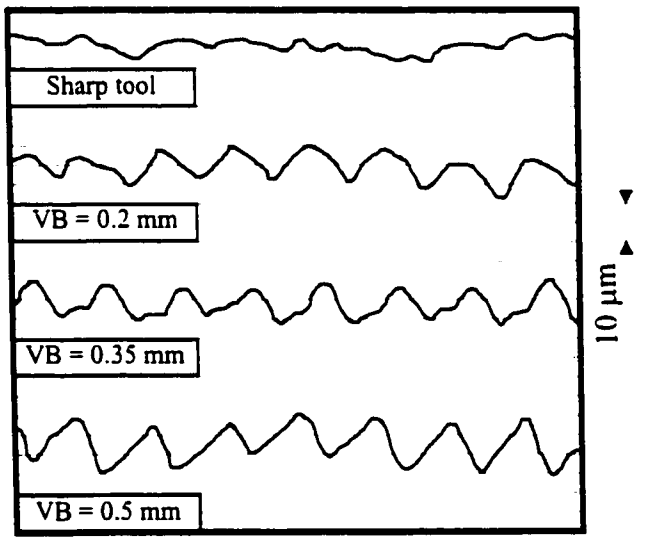

c- Effect of tool wear

Fig. 6.1 Effect of cutting conditions and tool wear on workpiece surface roughness
(V = 350 m/min, r = 1.2 mm, chamfered edge 20°)

of 0.2 mm and 0.35 mm, the variation of surface roughness is negligible and Ra is 0.5 μm. Ra increases to 0.7 μm when the tool wear land increases to 0.5 mm. The increase in the surface roughness with tool wear is attributed to the existence of material side flow on the feed scalps, as will be explained later.

The experimental observations concerning the surface finish produced during high speed machining of D2 tool steel in its hardened conditions show that a "good" surface finish, up to 0.5 μm, can be achieved using different cutting conditions with a tool wear of 0.2 mm. Since surface finish is only one of the parameters which affect the performance and fatigue strength of the product, it is important to continue examining the other parameters of the surface integrity.

6.4 Surface Examination

Despite the fact that a good surface finish was produced using the aforementioned cutting conditions, a closer examination of the machined specimens under the scanning electron microscope (SEM) shows that several distinguishing features can be identified. The main features observed are microcracks, cavities, and material side flow. With the exception of material side flow, these features exist irrespective of the cutting or tool conditions. The considerable variation in the density and appearance of these features, however, depends on cutting speed and tool wear. Figures 6.2, 6.3 and 6.4 show a selection of the surfaces generated under different cutting conditions.

It is observed that when machining with a chamfered (new) cutting tool, a feed of

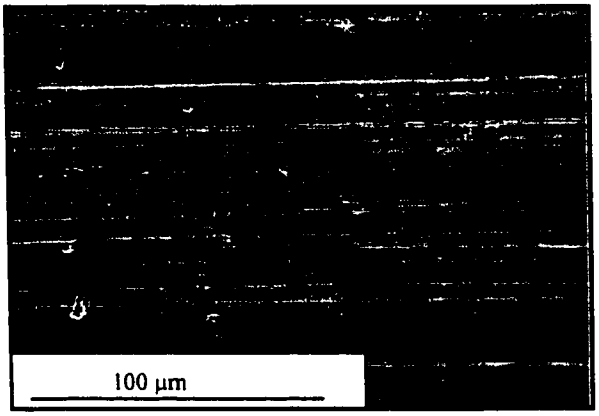

a- Sharp tool

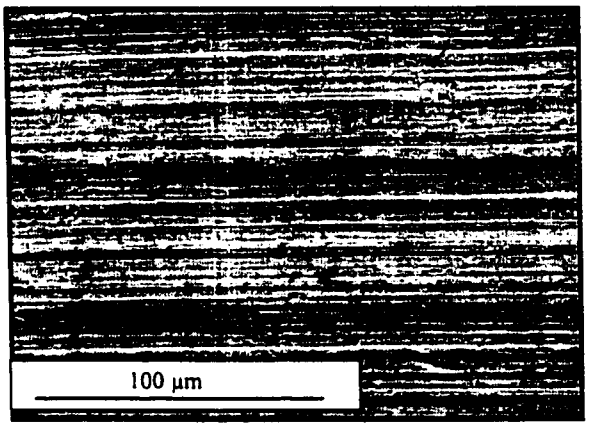

b- Worn tool (Wear land = 0.2 mm)

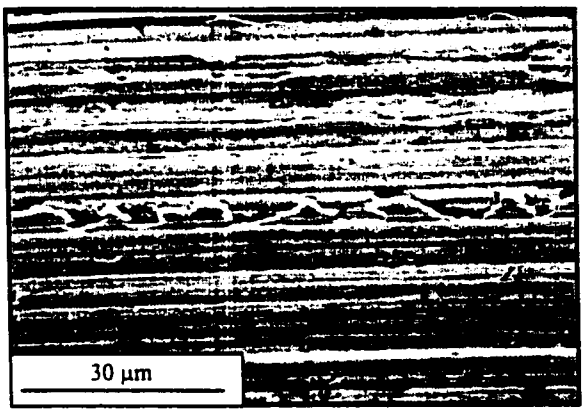

c- Worn tool (Wear land = 0.5 mm)

Fig. 6.2 SEM images of surfaces produced by sharp and worn tools
(V = 350 m/min, f = 0.1 mm/rev, d = 0.4 mm, r = 1.2 mm, chamfered edge 20°)

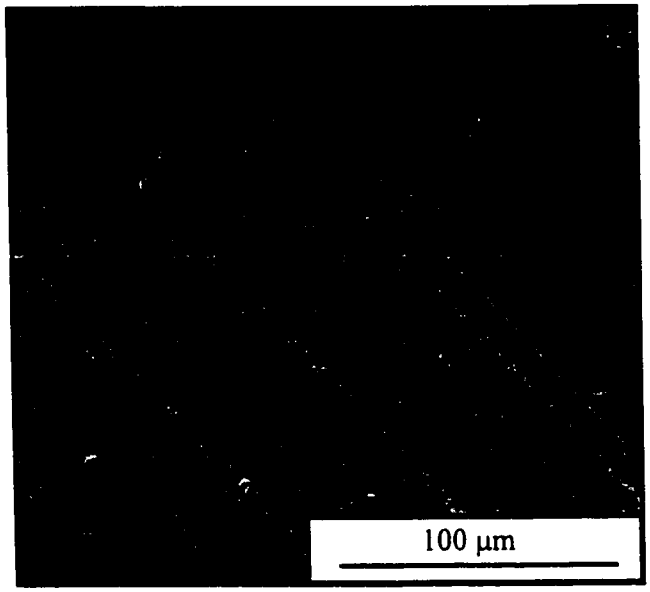

a- Wear land = 0.06 mm

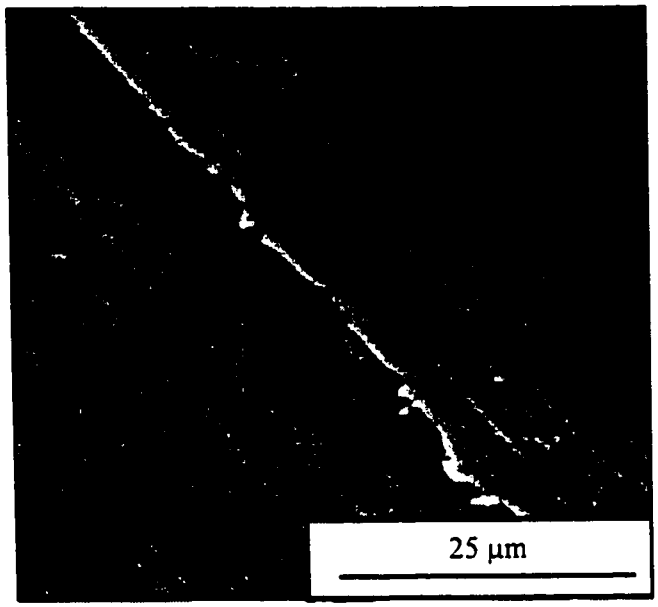

b- Wear land = 0.42 mm

Fig. 6.3 Effect of tool wear on material side flow
(V = 270 m/min, f = 0.05 mm/rev, d = 0.2 mm honed cutting edge with 1.2 mm nose radius)

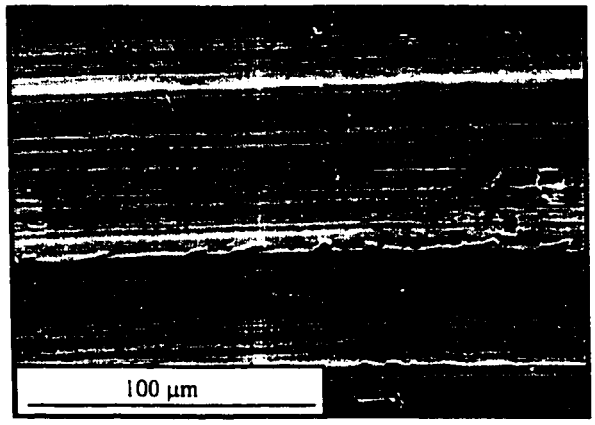

a- Grooves, cavities side flow, and microcracks
(worn tool, Wear land = 0.2 mm)

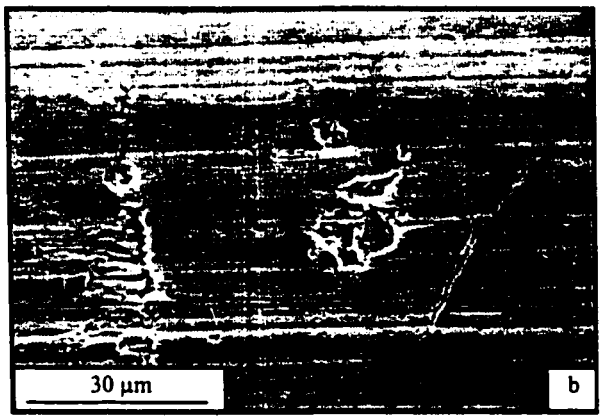

b- Enlarged image of the cavities and microcracks
(worn tool, Wear land = 0.2 mm)

Fig. 6.4 SEM images of surfaces produced by a worn tool
(V = 350 m/min, f = 0.1 mm/rev, d = 0.2 mm, r = 1.2 mm, chamfered edge 20°)

0.1 mm/rev, and a depth of cut of 0.4 mm, the surface behaves as a ductile material despite its hardness. Long, straight, well defined grooves parallel to the direction of relative work-tool motion can be seen in Fig. 6.2-a. An additional feature distinguishable in the specimen, which is always observed when cutting with PCBN tools (Bresseler, et al., 1997) is the presence of microchips, which remain attached to the workpiece surface. This surface defect appears as a porous structure. Figure 6.2-b shows that as the tool wears (flank wear was 0.2 mm) the surface roughness increases, and segments of the workpiece are removed from below the surface, leaving cavities. When the flank wear reaches 0.5 mm, surface metal displaces in the direction opposite to the feed mark ridges (Fig. 6.2-c). This is known as material side flow, and it has been observed previously during hard turning with a worn tool (El-Wardany et al., 1993). The material side flow phenomenon has always been observed in hard turning when the tool wear exceeds a specified limit. It is defined as the displacement of workpiece material in a direction opposite to that of the feed, such that burrs form on the feed mark ridges (Pekelharing and Gieszen, 1971). Examining the machined surface roughness at a high cutting speed (500 m/min) and at different levels of tool wear shows that the machined surface roughness deteriorates as the tool wear increases. For tool wear lands of 0.087 mm, 0.162 mm, and 0.23 mm, the measured surface roughness values are 0.19 μm , 0.3 μm , and 0.59 μm, respectively. The increase in the surface roughness can be attributed to the existence of material side flow on the machined surface. Figure 6.3 shows SEM images of two machined surfaces obtained at two different levels of tool wear (0.06 mm and 0.42 mm) using 270 m/min cutting speed, 0.05 mm feed and 0.2 mm depth

of cut. The observed material side flow is more severe when machining with a worn tool. Similar observation was reported by Bresseler et al. (1997). A detailed investigation of the material side flow phenomenon will be presented later.

Fine discontinuous grooves are also observed, which indicate the existence of material flow due to the occurrence of severe plastic deformations on the workpiece surface. These grooves are short in length and ill-defined. Sections of the workpiece have been removed from the surface leaving cavities, as shown in Figs. 6.4-a and b. Within these cavities, evidence of plastic deformation, microcracks, and voids can be seen. Brittle fractures can be seen in Figs. 6.5 (a and b). These cracks are observed more frequently as the tool wear land increases. The main source of surface microcracks is workpiece material nonhomogeneity caused by local differences in the material elements concentration, as well as the existence of chromium carbide particles. Hence, the material flow during the cutting process is interrupted due to the low deformability of the carbide particles leading to the initiation of microcracks on the machined surface. Figure 6.5-c shows SEM images of the sub-surface structure where a broken carbide inclusion on the surface is observed. These images reveal the possibility of the existence of microcracks on the machined surface.

Figures 6.6-a and b show SEM images of the machined surfaces obtained at two different cutting speeds (150 and 270 m/min). The cutting conditions used were f = 0.05 mm, d = 0.2 mm, with a honed cutting edge having 0.8 mm nose radius. The existence of the surface microcracks is clear in both cases where the microcracks exist in the carbide particles. A typical cutting edge radii of 1.2, and 1.6 mm or round inserts are used in the

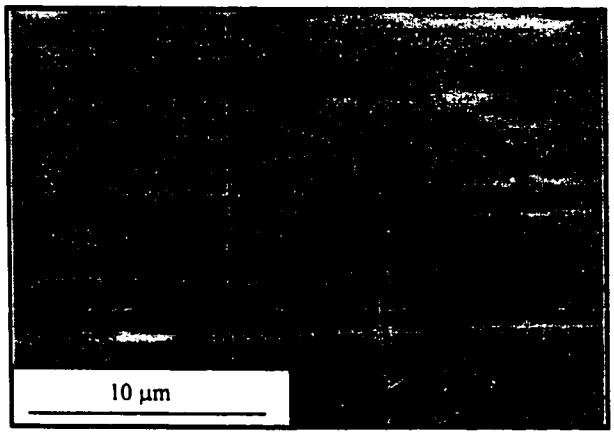

a- Surface microcracks

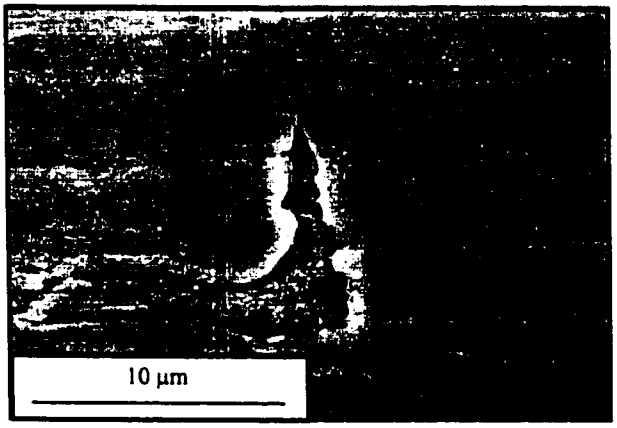

b- Machined surface defects

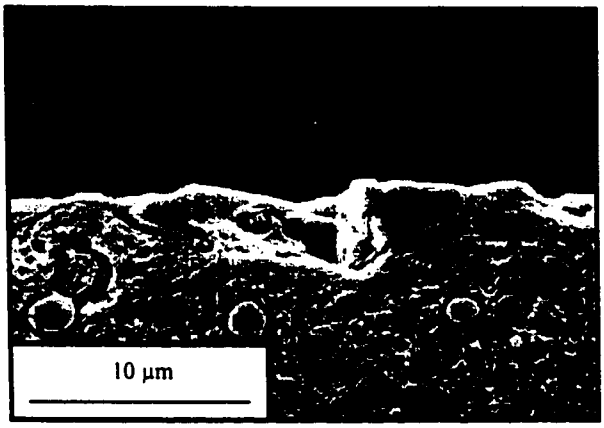

c- Broken carbide particles beneath the surface

Fig. 6.5 SEM images of the machined surface
(V = 350 m/min., f = 0.05 mm/rev, d = 0.4 mm, r = 1.2 mm, chamfered edge 20°)

a- V = 150 m/min

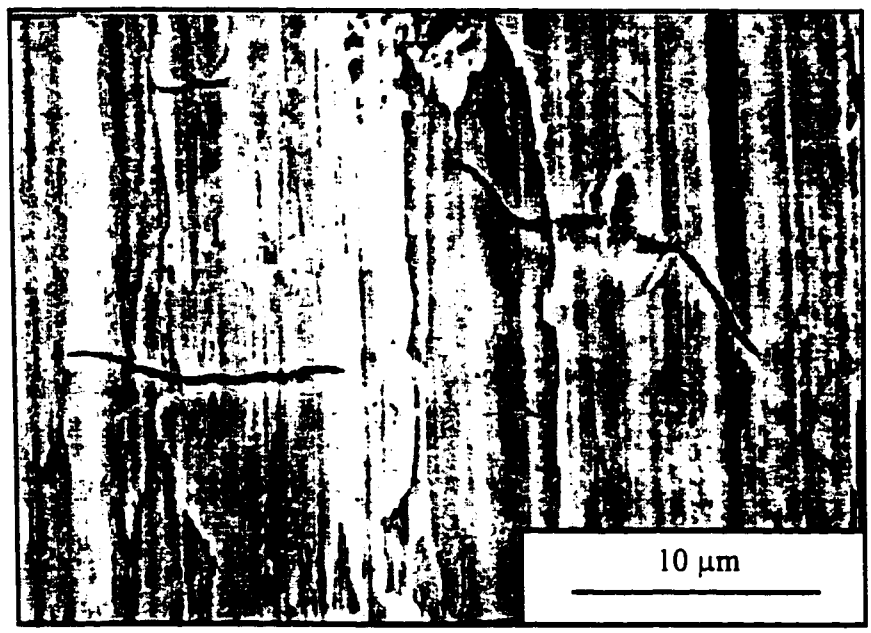

b- V = 270 m/min

Fig. 6.6 SEM images showing the effect of cutting speed on surface microcracks (f = 0.05 mm/rev, d = 0.2 mm, honed tool with 0.8 mm nose radius)

finish machining of hardened steel. Because of the low depth of cut and the large cutting edge radius, chip formation usually takes place only on the tool nose. Hence, the thrust force Fy is the largest force component (Tönshoff et al., 1995a). This generates extremely high stresses in the contact area between the workpiece surface and the tool. With the existence of low deformable inclusions directly in the surface, microcracks are generated in the surface.

Figures 6.7-a and b show the effect of cutting speed on the density of machined surface microcracks. Although microcracks exist in both cases, the density of these microcracks is much less at a higher cutting speed. It is believed that the lower density of surface microcracks at a higher cutting speed is attributed to the increase in the cutting temperature which leads to thermal softening and local ductility of the carbide particles in the vicinity of the machined surface. Figures 6.8 (a and b) reveal the sub-surface structure where a large carbide particle is forced to deform in the vicinity of the surface due to local ductility caused by the cutting temperature and pressure. However, lower deformability of the carbide particle causes microcracks beneath the machined surface where the effect of the cutting temperature diminishes.

As previously mentioned, an additional feature observed during examination of the machined surface was the presence of cavities and grooves. Figures 6.9-a and b show SEM images of machined surfaces obtained using worn tools where segments of the workpiece are removed from the machined surface leaving cavities. With an increase in the cutting speed this type of surface damage decreases in terms of severity the total area affected. A similar observation was reported by Warnecke and Bach (1988).

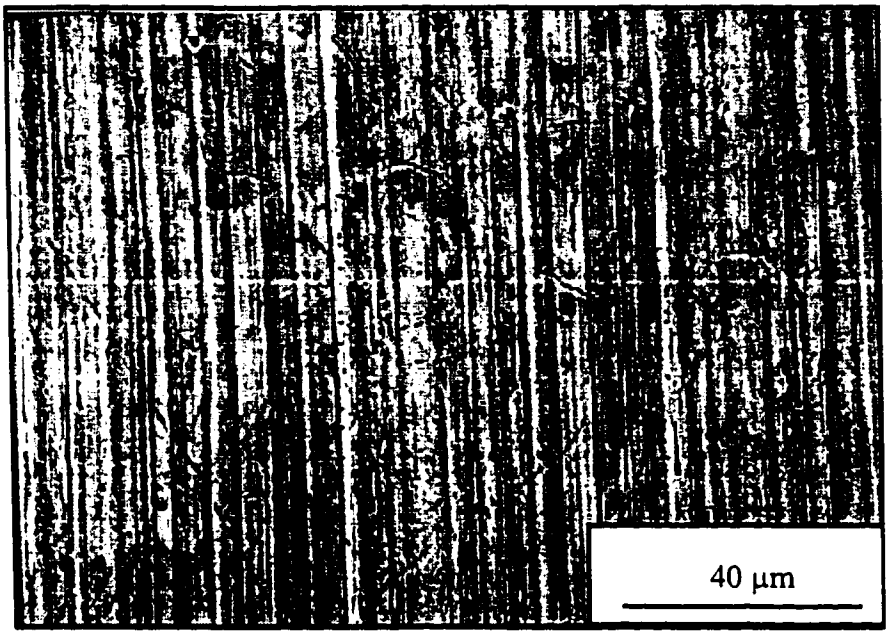

a- V = 150 m/min

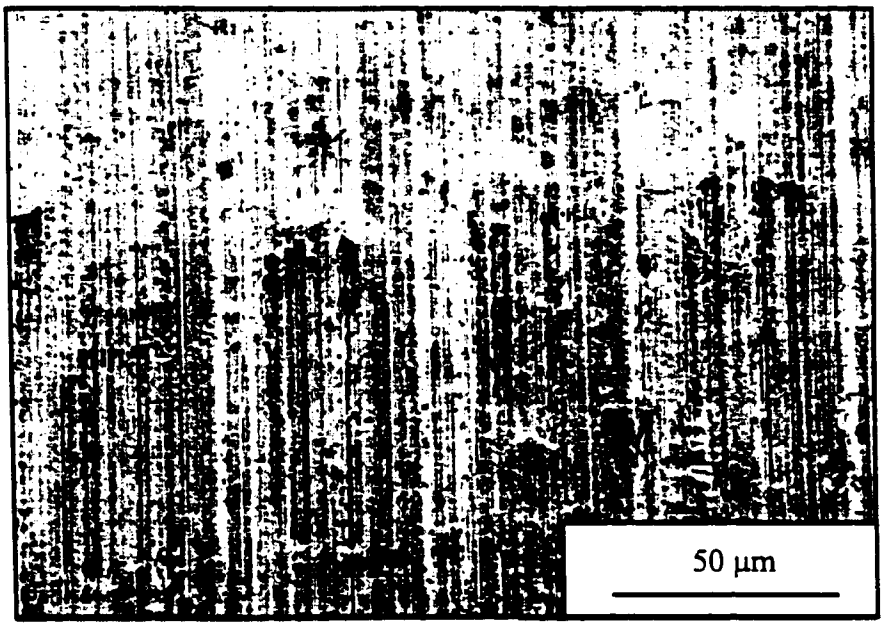

b- V = 270 m/min

Fig. 6.7 Effect of cutting speed on the machined surface microcracks
(f = 0.05 mm/rev, d = 0.2 mm, honed tool with 0.8 mm nose radius)

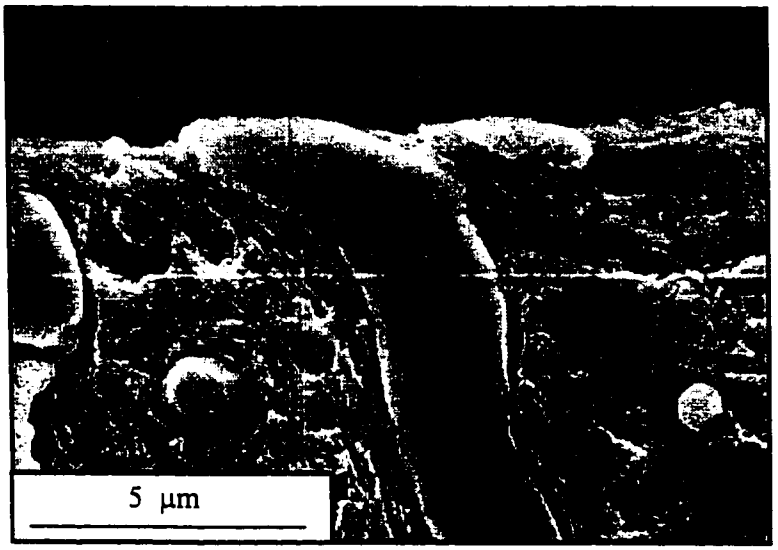

a- Plastic deformation and microcracks in carbide particle

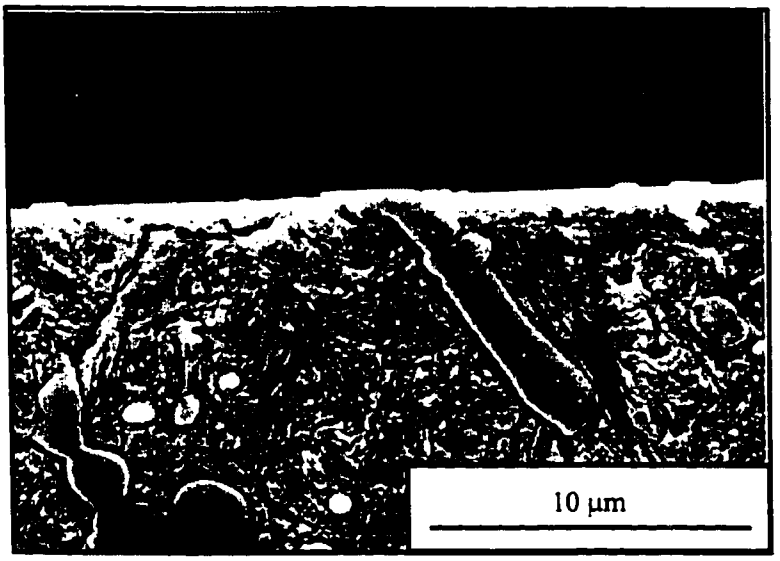

b- Carbide particle deformation due to high temperature

Fig. 6.8 SEM images of the machined sub-surface layer

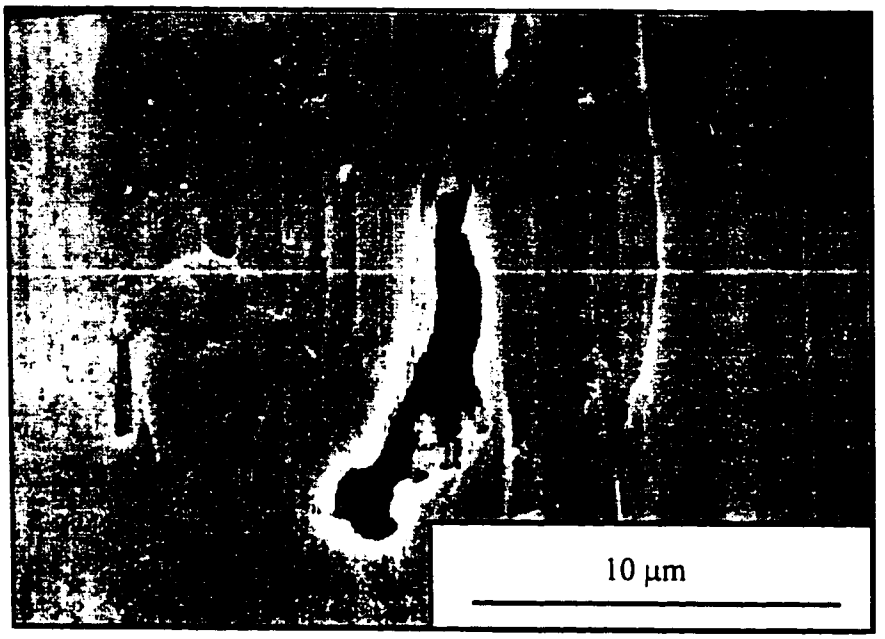

a- Sharp cutting edge

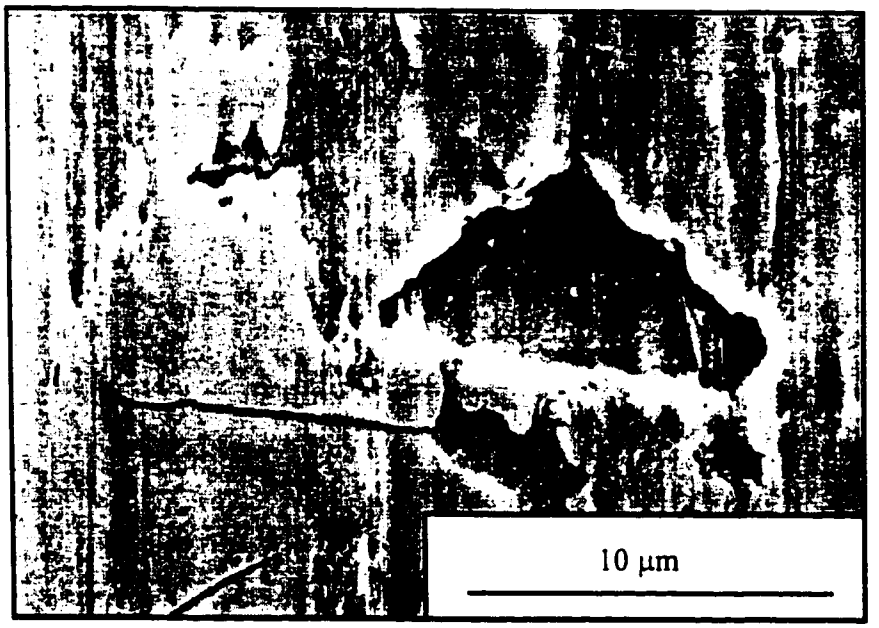

b- Honed cutting edge

Fig. 6.9 SEM images showing cavities in the machined surface

To a great extent, these types of surface damage influence the performance of the product. With the existence of low deformable inclusions directly beneath the surface, microcracks are generated on the surface. Microcracks existing on the surface produced reduce the fatigue resistance of the product. Also, material side flow deteriorates the quality of machined surface.

6.5 Sub-surface examination

The bulk structure of D2 tool steel is all fine tempered martensite. The high carbon contents in D2 tool steel increase the stability of the retained austenite remarkably. This means that the material will require a higher temperature and a longer time to undergo phase transformation (Roberts et al., 1962; Gill et al., 1944). On the other hand, the presence of the carbide particles in the D2 tool steel prevents the grains from growing under a high temperature. These features of the D2 material will affect the conditions of the sub-surface microstructure produced during machining.

The sub-surface structure of the machined specimen was examined under scan electron microscope in the unetched and etched conditions. Figures 6.10 (a and b) show SEM images of the unetched sub-surface structure revealing the existence of microcracks beneath the surface produced. Interestingly, these microcracks were found in the carbide particles. The brittle and hard carbide particles were forced to deform in the cutting vicinity due to the high temperature and force generated. The lower deformability of the carbide will cause microcracks, which spread beneath the surface due to the applied load (Fig. 6.8).

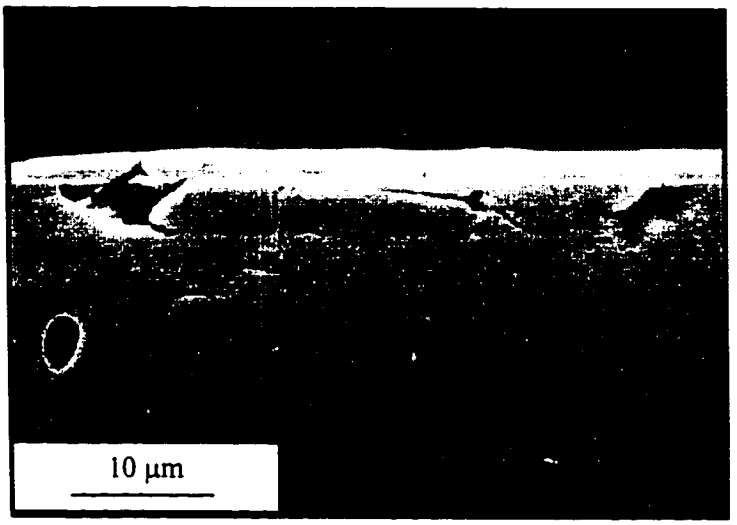

a- d = 0.4 mm

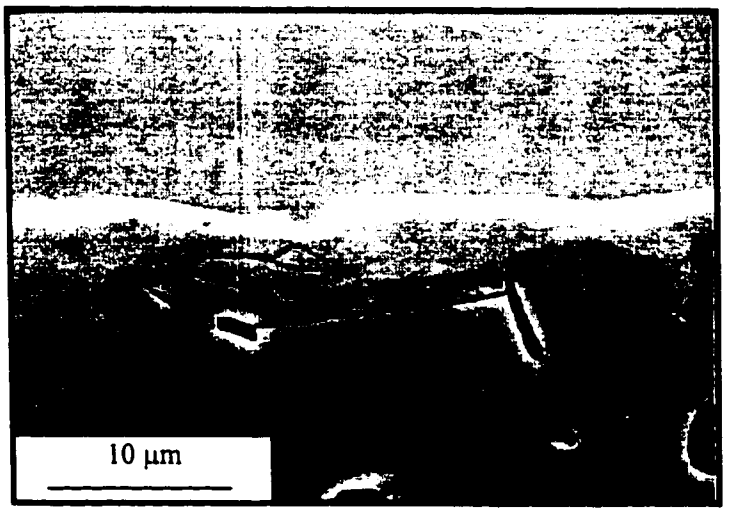

b- d = 0.6 mm

Fig. 6.10 SEM images showing microcracks in the unetched sub-surface
(V = 350 m/min, f = 0.1 mm/rev, r = 1.2 mm, chamfered edge 20°)

Figure 6.11 shows SEM image of the sub-surface produced when machining at 500 m/min cutting speed, 0.1 mm/rev feed, and 0.2 mm depth of cut using a worn tool (0.28 mm wear land) with a nose radius of 0.8 mm. General examination of the machined sub-surface structure shows three different layers. A thin white layer (layer A) is observed at the machined surface. Beneath this layer, a fine martensitic structure (layer B) is observed. This layer represents a plastically deformed layer with a thickness of 4 to 5 μm. The third layer (layer C) has a tempered martensitic structure of the original bulk material. In addition, grain boundary deformation is observed within a depth of 5 μm. This type of sub-surface deformation is attributed to the heavy plastic deformation in the machined surface.

Figure 6.12 shows SEM image of a machined sub-surface structure obtained at 270 m/min cutting speed, 0.1 mm/rev feed, and 0.2 mm depth of cut using a sharp tool having a wear land of 0.35 mm. A very thin layer (1 μm) of untempered martensite (white layer) is obtained. This indicates that the austenization temperature (A3) has been exceeded within this layer leading to the generation of a white layer caused by a rapid self cooling. It should be mentioned that the thickness of the obtained white layer is much less than that obtained in D2 tool steel surface produced by grinding or EDM (Field and Kahles, 1971). In addition, the thickness of the white layer obtained in this investigation is smaller than that obtained during the machining of case hardened steel (Tönshoff et al., 1995). This can be attributed to the high carbon content in D2 tool steel which increases the stability of the retained austenite remarkably . This means that the material will require a higher temperature and a longer time to undergo phase transformation (Roberts et al., 1962; Gill et al., 1944). On

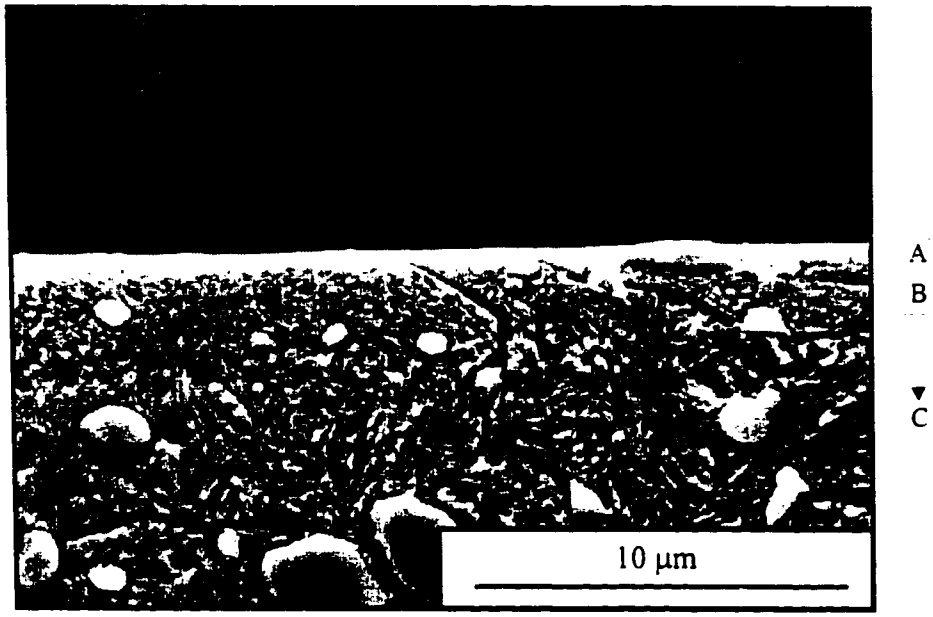

Fig. 6.11 SEM image showing different sub-surface layers
(V = 500 m/min, f = 0.1 mm/rev, d = 0.2 mm, 0.28 flank wear and 0.8 mm nose radius)

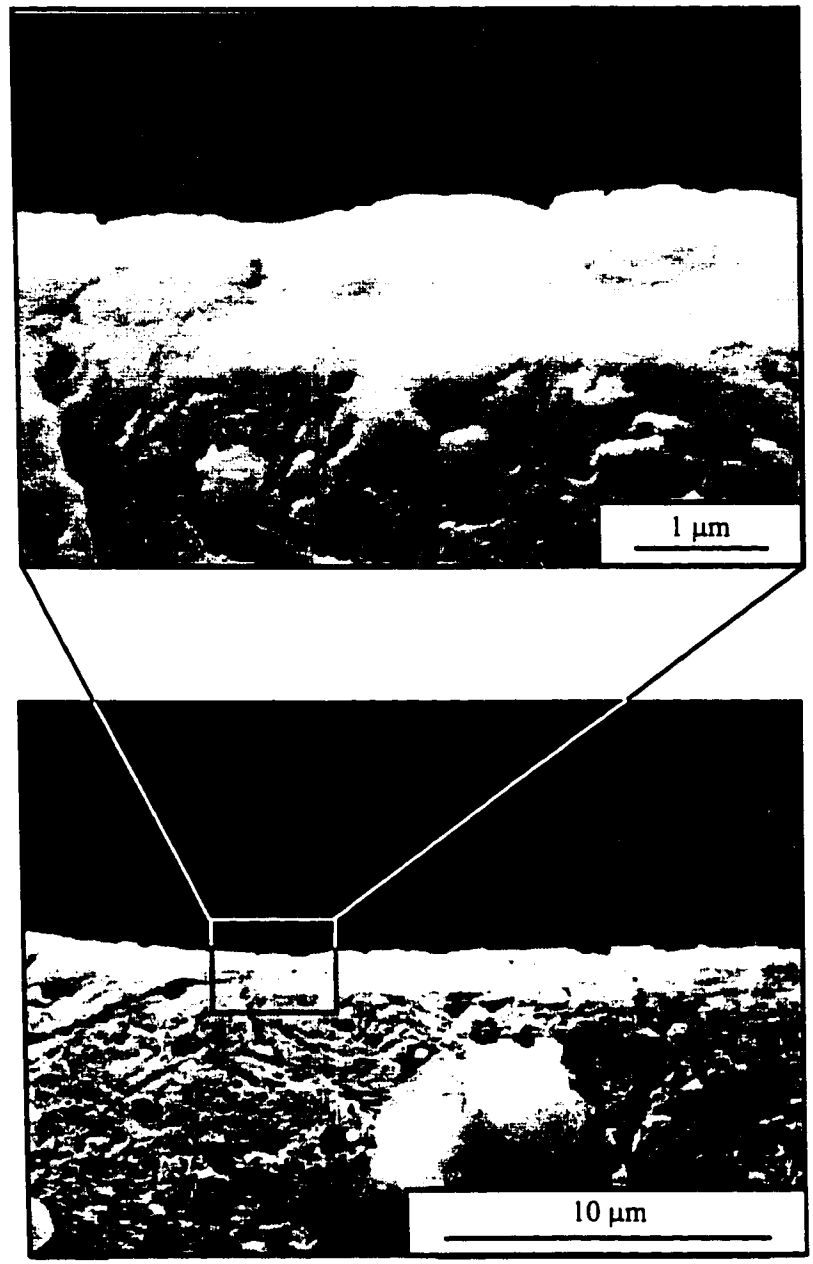

Fig. 6.12 White layer in machined surface
(V = 270 m/min, f = 0.1 mm/rev, d = 0.2 mm , worn tool with 1.2 mm nose radius)

the other hand, the presence of the carbide particles in the D2 tool steel prevents the grains from growing under a high temperature. These features of the D2 material would affect the changes of the sub-surface microstructure during machining.

It was generally observed that the thickness of the heat affected zone (white layer) is in a direct proportion to the tool wear. Furthermore, a combined effect of tool wear and cutting speed alters significantly the depth of the heat affected zone. Figures 6.13-a and b show SEM images of the sub-surface structure generated at two different levels of tool wear using a sharp cutting tool. Cutting speed, feed and depth of cut were kept constant. With an increase in tool wear, the thickness of the heat affected zone is increased. This can be attributed to the effect of tool wear on the heat generated during machining. Although machining at high cutting speeds generates more heat than at a low cutting speeds, the contact time is much lesser at high cutting speeds. In addition, most of the heat generated at high cutting speeds is carried out with the chip resulting in less damage in the sub-surface structure. This is very clear when examining the sub-surface structure of a surface machined at 270 m/min using a sharp tool, Fig. 6.14. The heat affected zone is hardly noticeable in this case. It is believed that within certain values of tool wear, a high cutting speed can eliminate the side effects of the heat generated due to the short contact time between the tool wear land and the workpiece.

Selections of the etched sub-surface microstructures generated during cutting are illustrated in Figs. 6.15 to 6.17, and will be discussed in the following:

1- For a feed of 0.1 mm/rev, and a depth of cut of 0.4 mm, a heat affected zone (white

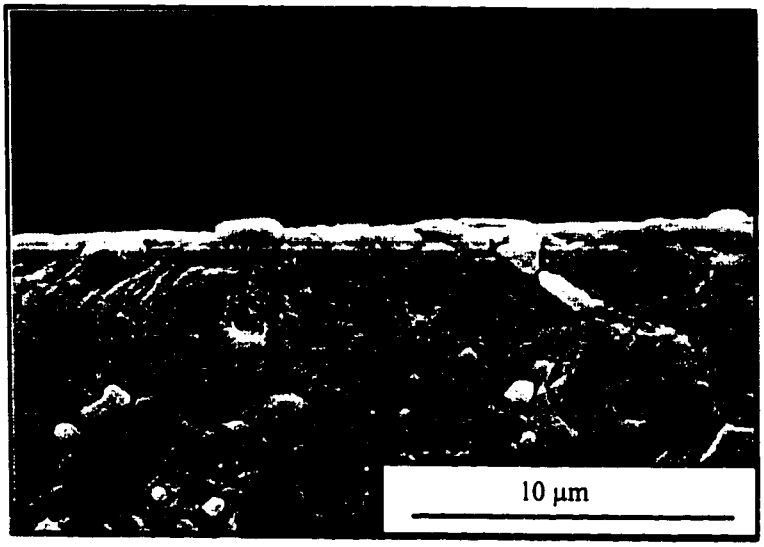

a- 0.162 mm wear land

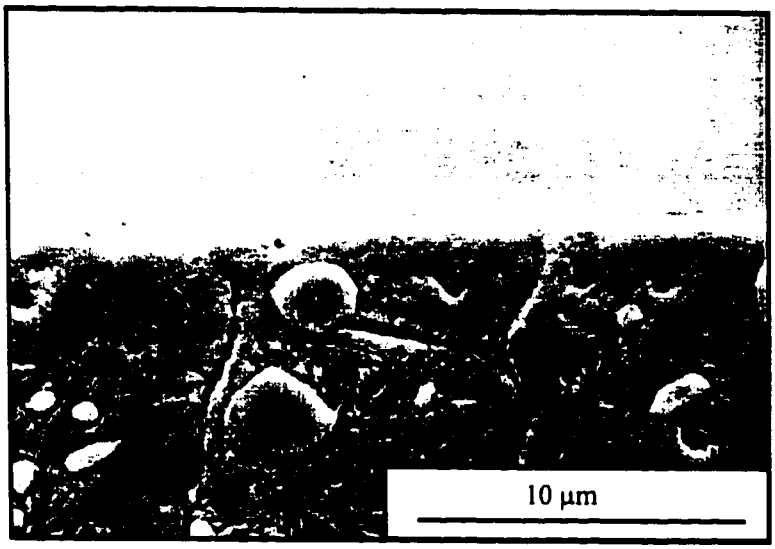

b- 0.25 mm wear land

Fig. 6.13 Effect of tool wear on sub-surface deformation
(V = 140 m/min, f = 0.1 mm/rev, d = 0.2 mm, and 1.6 mm nose radius)

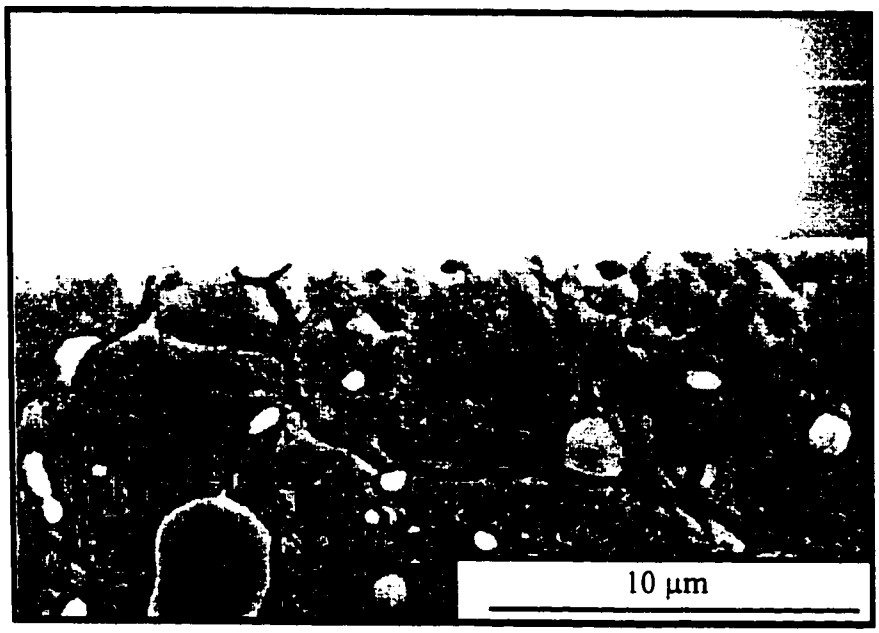

Fig. 6.14 SEM image for sub-surface obtained using sharp tool
(V = 270 m/min, f = 0.1 mm/rev, d = 0.2 mm)

layer of untempered martensite) was present in the surface region of the specimens. When the tool was sharp, the observed layer was very thin (Fig. 6.15-a). With the progress of tool wear, the thickness of the white layer increased to almost 1 μm (Fig. 6.15-b). This is an unusually low thickness since a high cutting speed was used, and it is mainly dependent on the material properties. A white layer thickness of 2 μm was only observed when the tool wear reached 0.5 mm, which is much higher than the tool wear limit specified for the end of the tool life (Fig. 6.15-c). For the same cutting speed and feed, the white layer was hardly noticeable when cutting with a worn tool (0.2 mm wear land) and a depth of cut of 0.6 mm (Fig 16.15-d). For a higher feed of 0.2 mm/rev and a lower depth of cut of 0.2 mm, a very thin layer was observed. The thickness of the white layer observed in this study is much smaller than that which existed on the D2 tool steel surface produced by grinding, EDM or conventional cutting processes (Field and Kahles, 1971). The main reason for the low penetration depth of the surface changes in this case is the shorter contact time and, consequently, the limited time for heat transition. A white layer of 2 to 3 μm was observed by different investigators during the machining of high strength materials under a range of cutting speeds, feeds, and depths of cut (Field et al., 1970; Field and Kahles, 1971; Bailey et al., 1976; Matsumoto et al., 1986; Tonshöff et al., 1995a, b). The heat affected zone was only observed when the cutting tool was excessively worn. The depth of this heat affected zone depended, to a great extent, on the length of the wear land and the cutting speeds (Matsumoto et al., 1986).

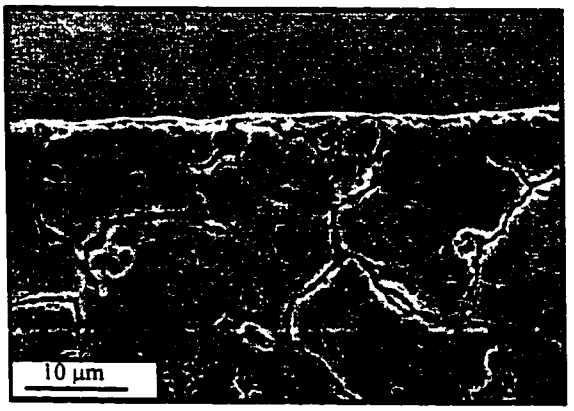

a- SEM image of sub-surface, sharp tool (d = 0.4 mm)

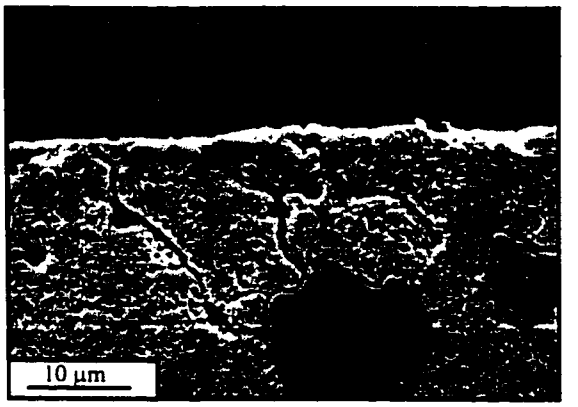

b- SEM image of sub-surface, worn tool (wear land = 0.2, d = 0.4 mm)

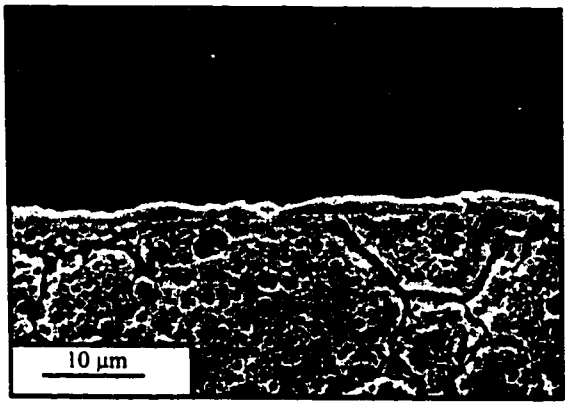

c- SEM image of sub-surface, worn tool (Wear land = 0.5, d = 0.4 mm)

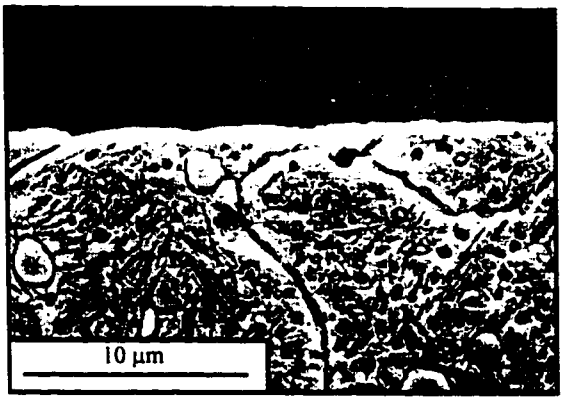

d- SEM image of sub-surface, worn tool (wear land = 0.2, d = 0.6 mm)

Fig. 6.15 SEM images of sub-surface microstructure
(V = 350 m/min, f = 0.1 mm/rev, r = 1.2 mm, chamfered edge 20°)

2- Figures 6.16 (a to c) show SEM images of the layer underneath the surface generated, using different feeds and depths of cut with tools having different levels of tool wear. The cutting speed was kept constant. From these images, the deformation of the grain boundaries underneath the surface generated is clearly visible. For the cutting conditions illustrated in Figs. 6.16-a, b, and c it can be seen that, at a distance from the machined surface of between 1.5 and 3.5 μm thick, the original grains are no longer discernible (region A). The surface itself and the upper region have a non-crystallographic orientation (characteristic of shear bands). The formation of these elongated subgrains has been equally associated with the large localized deformations, which occur under quasi-adiabatic conditions due to high deformation rates. The existence of the above mentioned observation indicates that high cutting temperatures were generated at these cutting and tool conditions.

3- There was no obvious overtempered martensite layer beneath the thin deformed layer. Figure 6.17-a is SEM image of the workpiece cross-section within the first 30 μm from the surface, while Fig. 6.17-b shows an image of the cross-section at a distance of 2 mm from the surface. In both images no increase in the size and spacing of the precipitated carbides was observed indicating the lack of overtempered martensite transformation. The same observation was found when hard turning of H13 tool steel (Abrão et al., 1995).

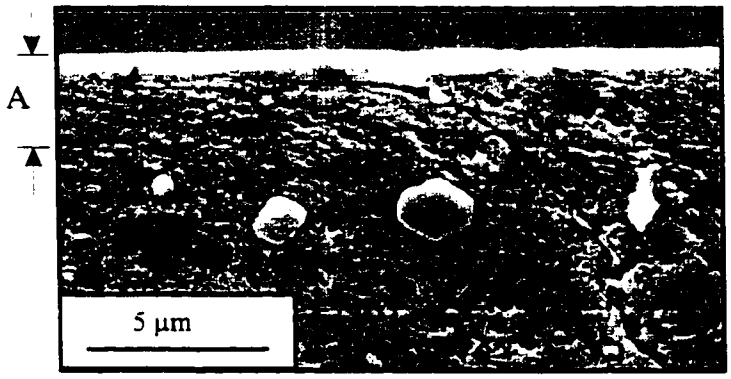

a- f = 0.2 mm/rev, d = 0.4 mm, wear land = 0.2 mm

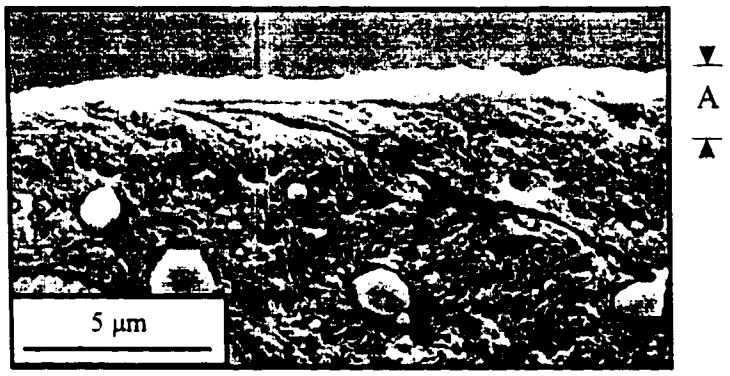

b- f = 0.1 mm/rev, d = 0.2 mm, wear land = 0.2 mm

c- f = 0.1 mm/rev, d = 0.4 mm, wear land = 0.5 mm

Fig. 6.16 SEM images showing the plastic deformation beneath the machined surface produced at different cutting conditions
(V = 350 m/min, r = 1.2 mm, chamfered edge 20 °)

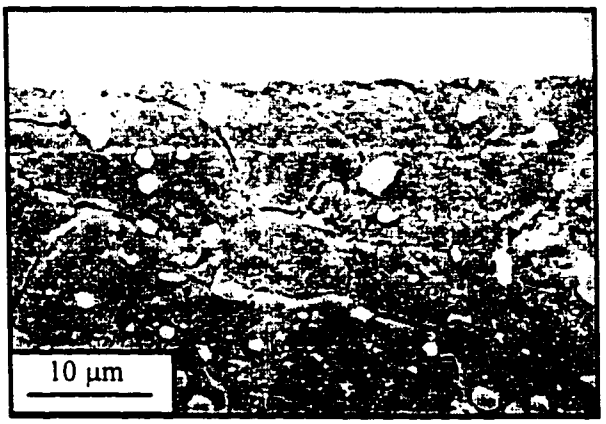

a- Microstructure at 30 μm beneath the surface (d = 0.2 mm)

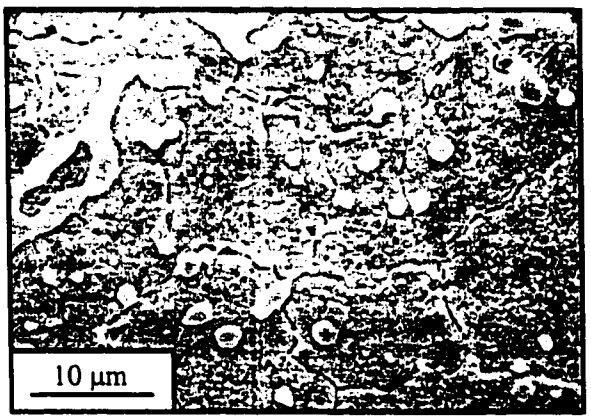

b- Microstructure at 2 mm beneath the surface (d = 0.2 mm)

Fig. 6.17 SEM images of the sub-surface microstructure
(V = 350 m/min, f = 0.1 mm/rev, r = 1.2 mm, chamfered edge 20°)

6.6 Material side flow

The general topography of the machined surface consists of long straight grooves in a direction parallel to the cutting speed. These grooves are caused by the microroughness of the cutting edge and the flank wear topography. Examination of the machined surface using SEM reveals the dependence of surface topography on tool microgeometry as well as the cutting conditions employed. Cutting forces, chip morphology and tool wear have a great influence on material side flow. Thus, it is helpful to study the characteristics and the interactions between these parameters to determine how they can affect the machined surface.

a- Cutting forces

Figure 6.18 shows the effect of cutting length on cutting forces during hard turning. The cutting length has a direct influence on the cutting forces. As expected, the thrust force is always the largest cutting force component in hard turning, which is attributed to the fact that the chip formation takes place mainly along the nose radius. Thus, a high ploughing force exists due to the large negative effective rake angle along the nose radius. In addition, an increase in the cutting length increases the tool wear which, in turn, increases the friction between the tool and the workpiece. Therefore, the ratio between the thrust force and cutting force increases.

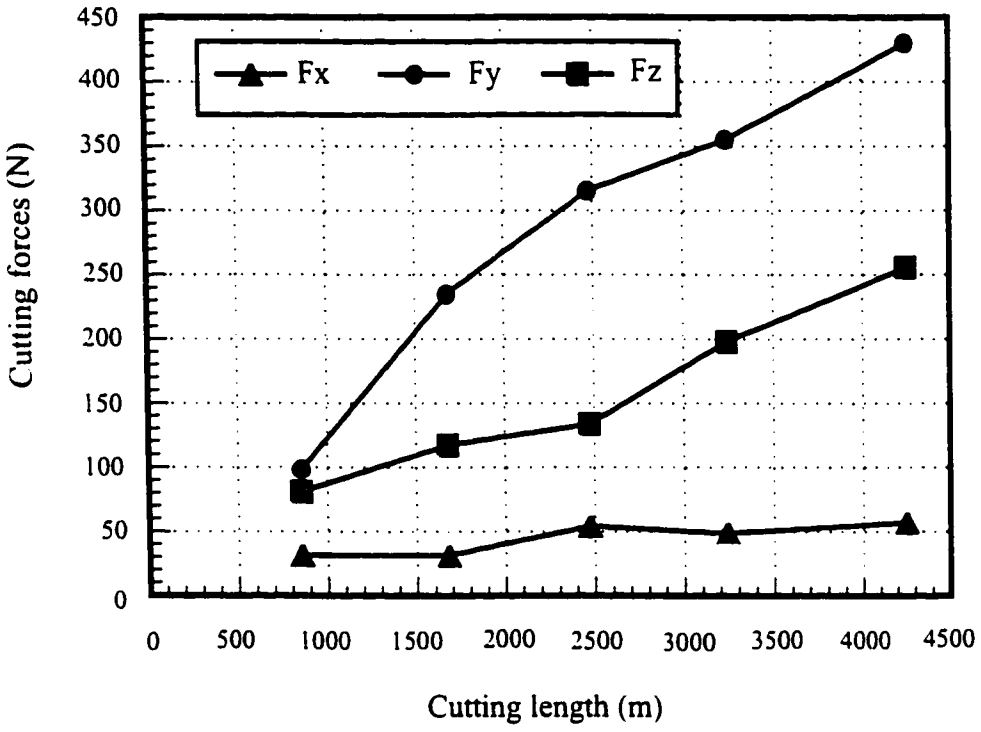

Fig. 6.18 Effect of cutting distance on cutting forces
(V = 250 m/min, f = 0.1 mm/rev, d = 0.125 mm, r = 1.2 mm, chamfered)

b- Chip morphology

The chip formation mechanism and the effect of process parameters as well as edge preparation on the chip morphology were studied in detail in chapter three. In this section, only the effect of nose radius on the chip morphology is presented because of its direct effect on tool wear and, hence, on material side flow. In analysing the chip morphology, it was noticed that an increase in the nose radius increases the chip edge serration, as shown in Fig. 6.19. The chip edge serration can be explained by the reduction in the actual chip thickness near the trailing edge. Since the chip formation takes place mainly along the nose radius, it is expected that the chip thickness varies along the cutting edge, as shown in Fig. 6.20. Due to the nose radius, the chip thickness is gradually decreased to zero and causes high pressure at the trailing edge. Thus, the material at the trailing edge of the tool, where the chip thickness is minimum, is subjected to stress concentration which causes tearing on the weakest edge of the chip. In addition, the variation in the chip particles velocity facilitates the non-uniform displacement along the chip width and, hence, leads to chip edge serration. The existence of the chip edge serration facilitates trailing edge wear. The significant difference in notch wear pattern due to chip serration was reported by Hodgson and Trendker (1981). During the chip formation process, the hot serrated chip can be turned and welded to the surface. The welded material is very hard and brittle and, hence, leads to a dramatic increase in the rate of tool wear, (Bresseler et al., 1997).

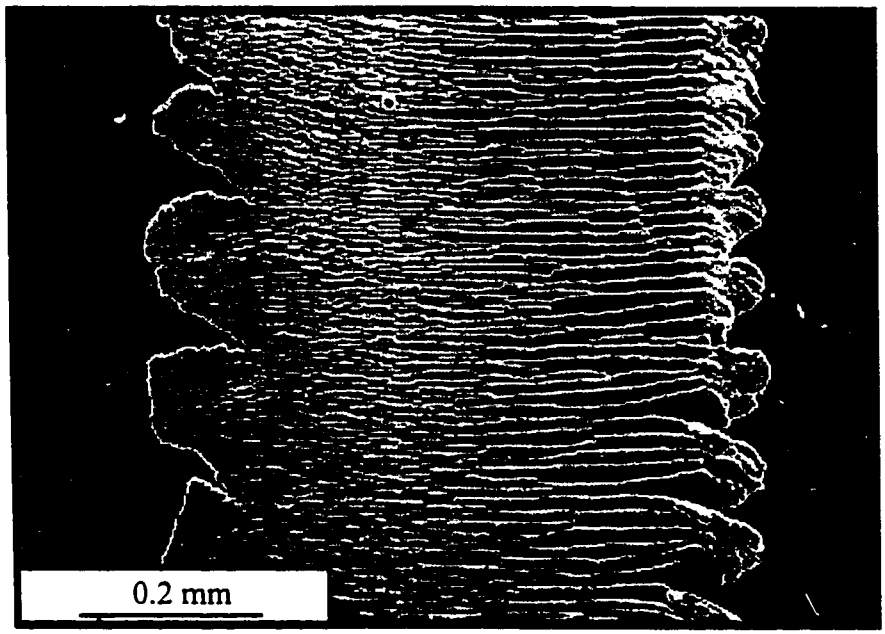

a- Large nose radius, r = 3.2

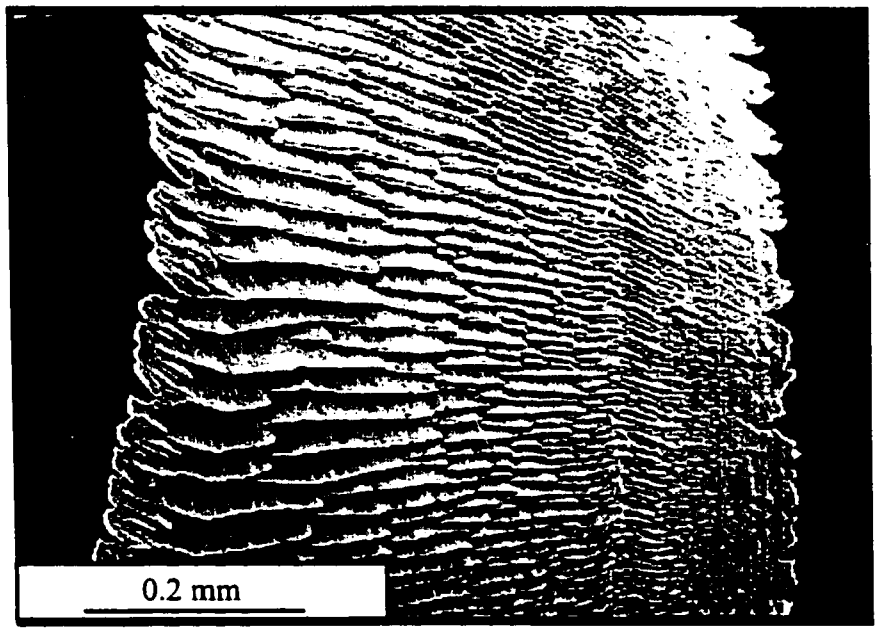

b- Small nose radius, r = 1.2 mm

Fig. 6.19 Effect of nose radius on chip morphology
(V = 250 m/min, f = 0.1 mm/rev, d = 0.125 mm)

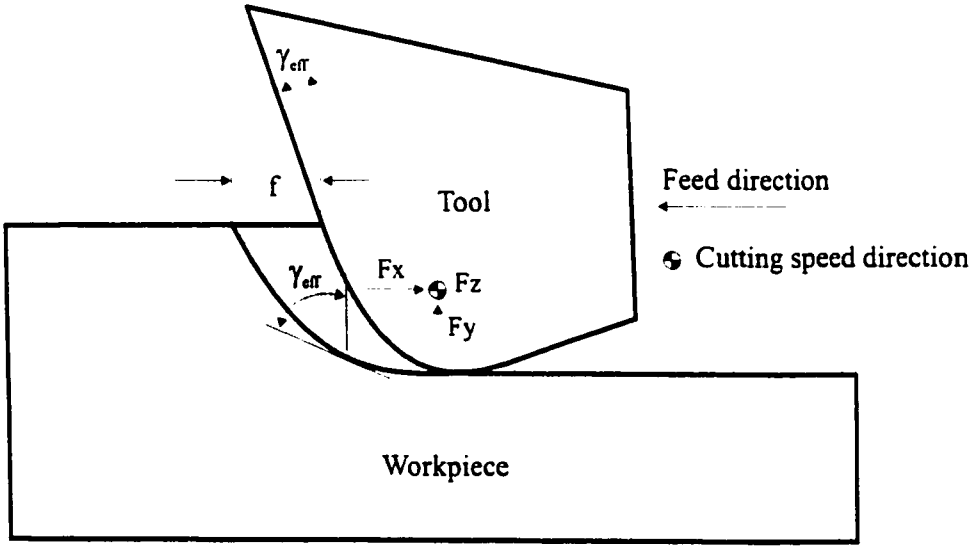

Fig. 6.20 Effect of nose radius on chip formation

c- Mechanisms of tool wear

Figure 6.21 shows the effect of edge preparation on tool wear. In general, increasing the nose radius increases the level of tool flank wear, as shown in Fig. 6.21-a. Cutting with a large nose radius results in a higher value of cutting forces which is more pronounced in the thrust force component (El-wardany et al., 1996). On the other hand, cutting with a small nose radius prolongs tool life which can be explained by the reduction in the ploughing force. Figure 6.21-b shows the measured flank wear when using sharp and chamfered tools. Although the chamfered tool is recommended to prevent the chipping of the cutting edge, there is no significant difference in the rate of tool wear.

As cutting progresses, the tool wear appears as a flat area along the trailing edge of the tool, as shown in Fig. 6.22-a. In addition, the serrated edge of the chip abrades the cutting tool. The flattened area of the tool is in contact with more than one feed mark. Therefore, at small feeds, the feed marks are printed on the tool as small grooves at a distance equal to that of the feed, (Fig. 22-b). In analysing the tool wear, flank wear with a trailing edge notch and a depth of cut notch are the main tool wear mechanisms observed. Figure 6.22-a shows SEM image of typical flank wear during the machining of hardened steel. Several grooves exist at the trailing edge of the tool. As can be seen, the first groove is located precisely at the edge of the chip. This observation proves the assumption that the trailing edge notch is caused by chip edge serration. This assumption was reported by Hodgson and Trendler (1981). The effect of the chip edge serration is observed where two lines are scratched by the chip edges in a direction parallel to that of the chip flow direction,

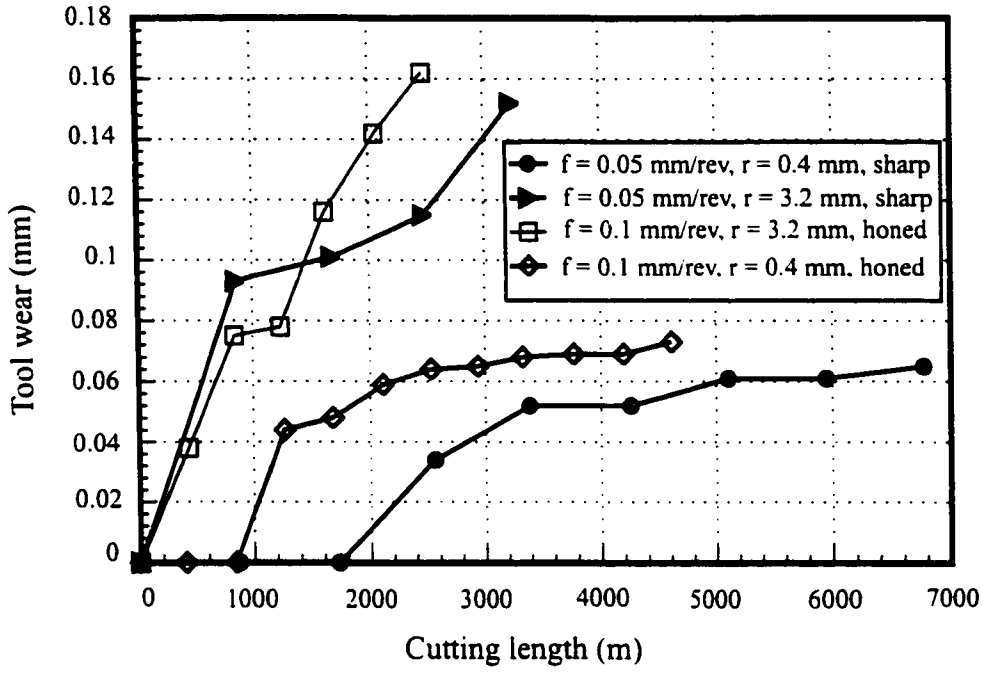

a- Sharp versus honed

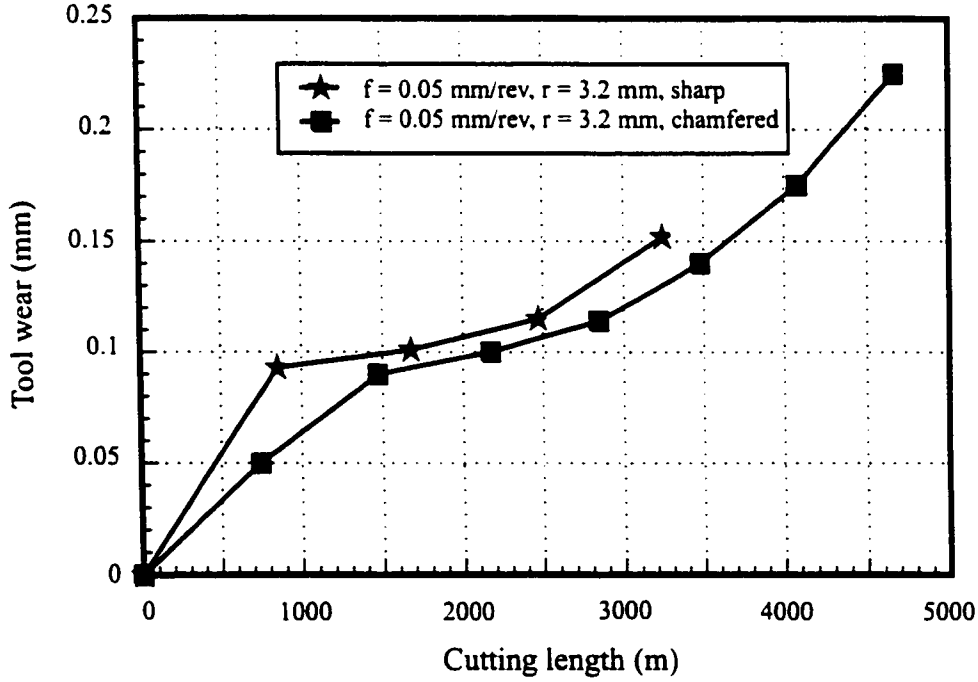

b- Sharp versus chamfered

Fig. 6.21 Effect of edge preparation on tool wear

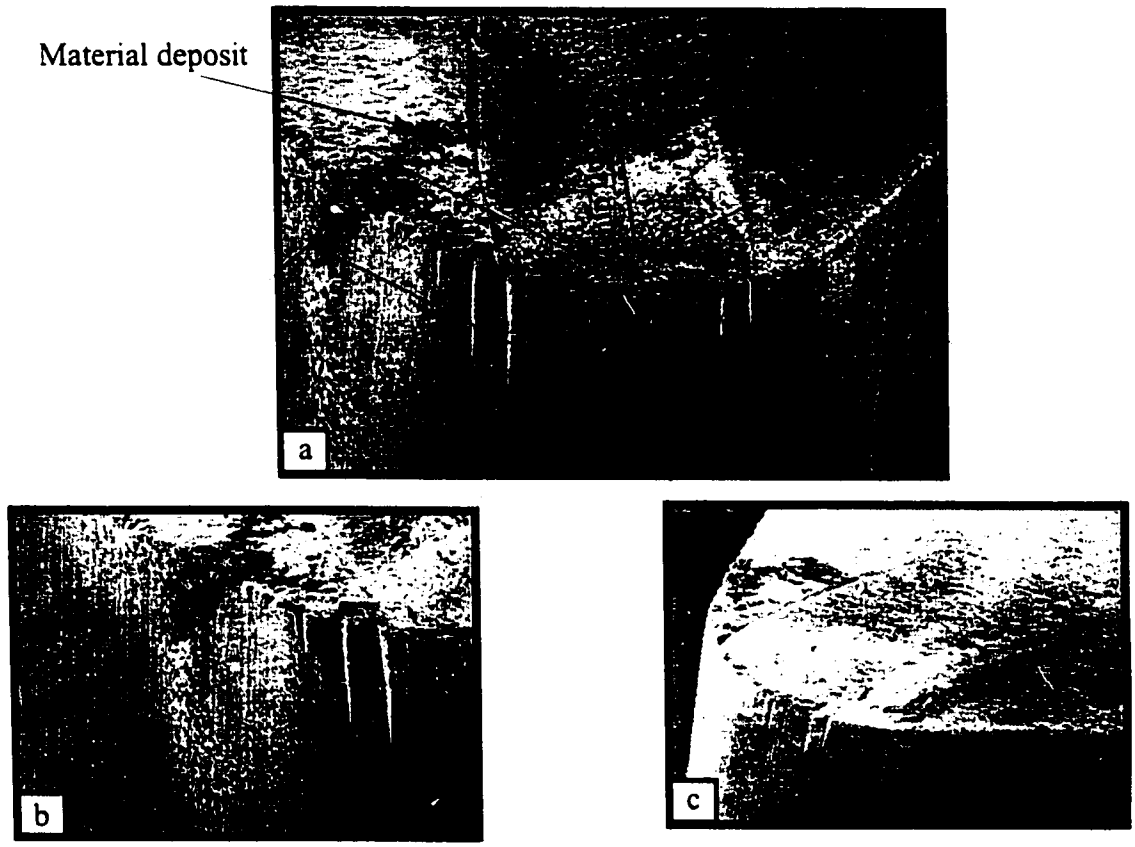

Fig. 6.22 Mechanisms of tool wear
(V = 250 m/min, f = 0.05 mm/rev, d = 0.125 mm, r = 0.4 mm, sharp tool)

as shown in Fig. 6.22. Also, deposited material is observed at both sides of the chip flow.

Figure 6.23 shows the plastic deformation of the cutting edge when using a chamfered tool. It is worth mentioning here that although the trailing edge notch was not very clear in this case, the plastic deformation exists at the cutting edge, reflecting the existence of high temperature and pressure when cutting with a chamfered tool. The existence of plastic deformation changes the tool geometry which leads to cutting with an extremely high negative effective rake angle. This, in turn, leads to increasing the plastification of the workpiece material and, hence, facilitates the existence of more material side flow on the machined surface.

The trailing edge notch is responsible for material side flow where material in the shear zone is displaced towards the first groove (Pekelharing and Gieszen, 1971). The displaced material will fill the first groove and the excess material will form the so-called "material side flow".

6.7 Mechanisms of material side flow

A machined surface examination using SEM shows that different kinds of defects exist during machining process. Material side flow is observed in the area of the feed marks where plastically deformed material is ploughed aside when the chip thickness is less than a certain value (t_{min}) (Shaw, 1984). This minimum chip thickness depends on many factors such as cutting tool material, workpiece materials, cutting conditions, and macrogeometry, as well as microgeometry of the cutting tool (Warnecke and Bach 1988). Tool angles, nose

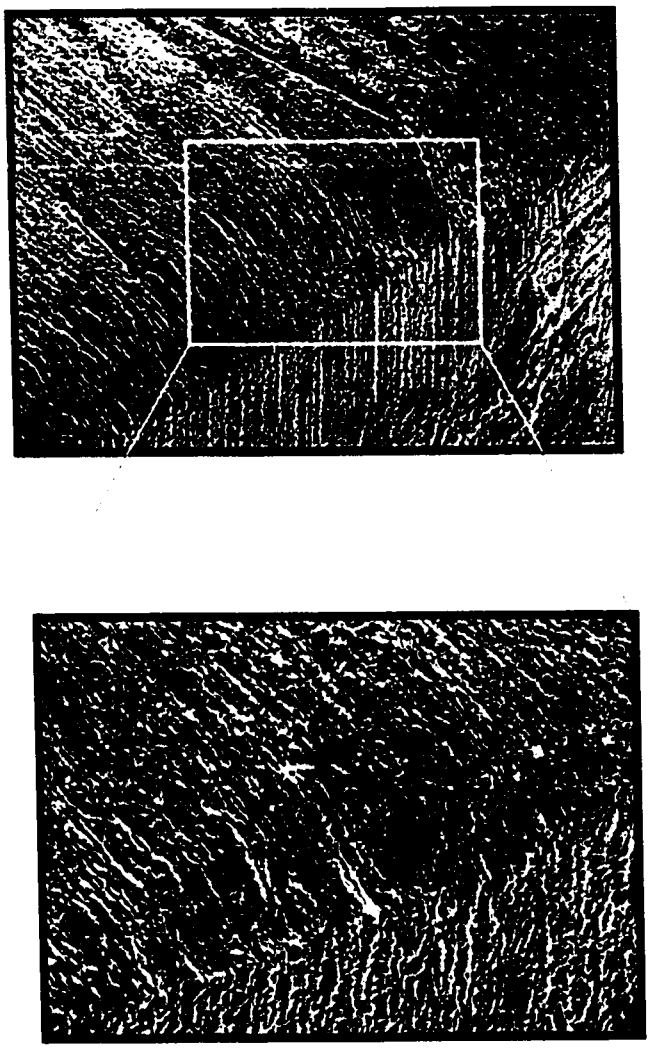

Fig. 6.23 Plastic deformation of the cutting edge
(V = 250 m/min, f = 0.1 mm/rev, d = 0.125 mm, r = 3.2 mm, chamfered tool)

radius and edge preparation represent the tool macrogeometry while the roughness of the cutting edge, grooves at the cutting edge, and the flank wear topography represent the tool microgeometry. The side flow of the workpiece material is facilitated by high temperature and normal stress in the cutting zone where the workpiece material at the chip/tool and workpiece/tool interface behaves as a viscous fluid. The results presented show material plastic deformation not only along the feed marks but also in between the feed marks, as can be seen in Fig. 6.24. If the chip thickness at any point along the nose radius is less than the minimum chip thickness (t_{min}), the workpiece material will be ploughed and squeezed by the tool. This mechanism is facilitated by the tool nose wear. In addition, the material side flow at the feed marks is mainly attributed to the trailing edge wear where material plastic flow fills the groove and the excess material is pressed to the side of the tool. Figure 6.25 is a schematic diagram showing the effect of nose radius on material side flow.

6.7. 1 Effect of feed

Figure 6.26 shows SEM images of two surfaces obtained at different feeds with a tool having a wear land of 20 μm. Although material side flow exists in both cases, examination of the surface machined by the lower feed reveals the existence of severe plastic flow. Despite the fact that a good surface finish is obtained using a small feed (where the height of the feed marks becomes smaller), a close examination of the machined surface shows that more material plastic flow exists. This can be explained by studying the effect of feed on the chip formation, as shown in Fig. 6.26-a and b. A lower feed increases the area

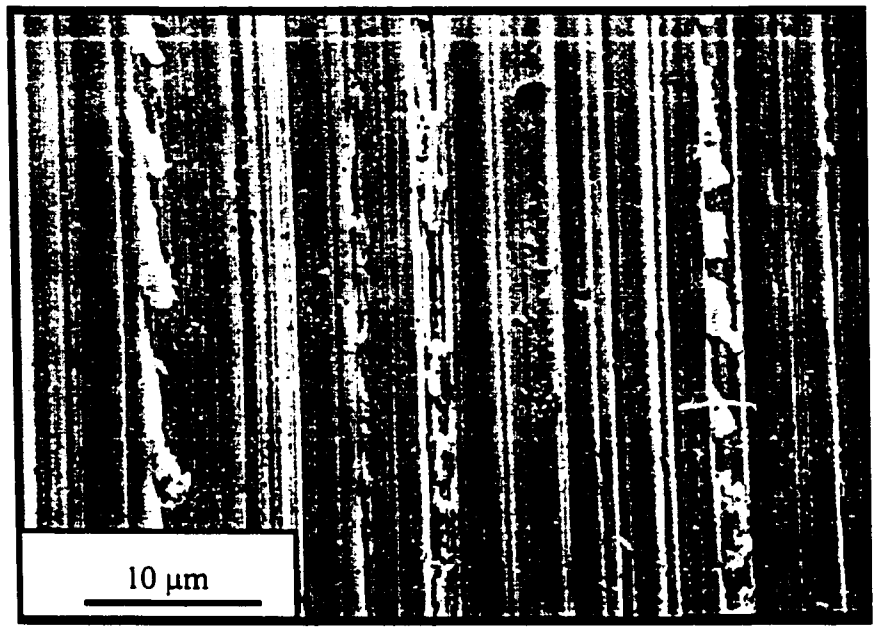

Fig. 6.24 Material side flow
(V = 250 m/min, f = 0.05 mm/rev, d = 0.125 mm, r = 3.2 mm, chamfered tool)

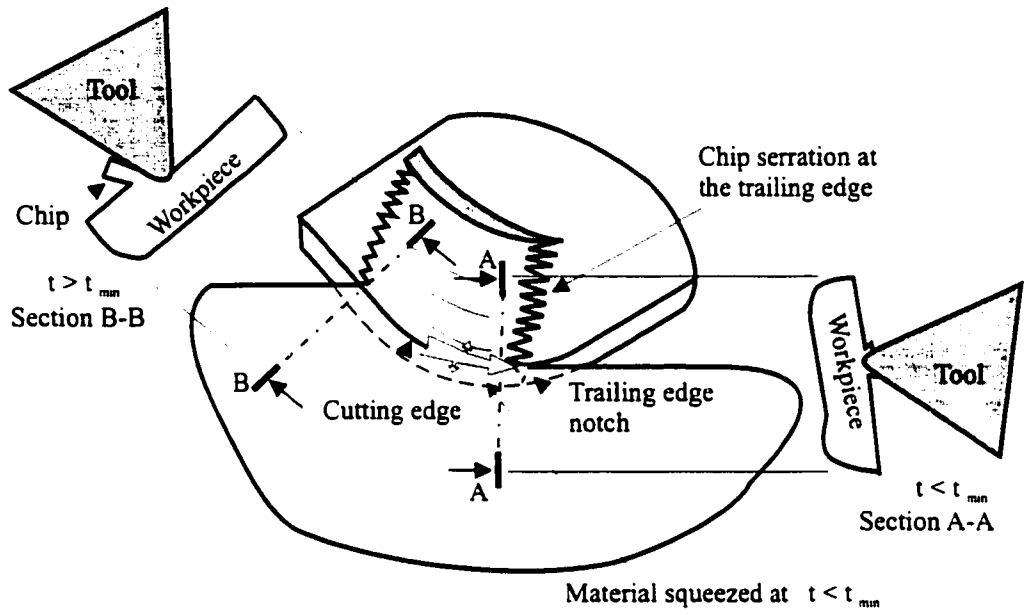

Fig. 6.25 Mechanism of material side flow

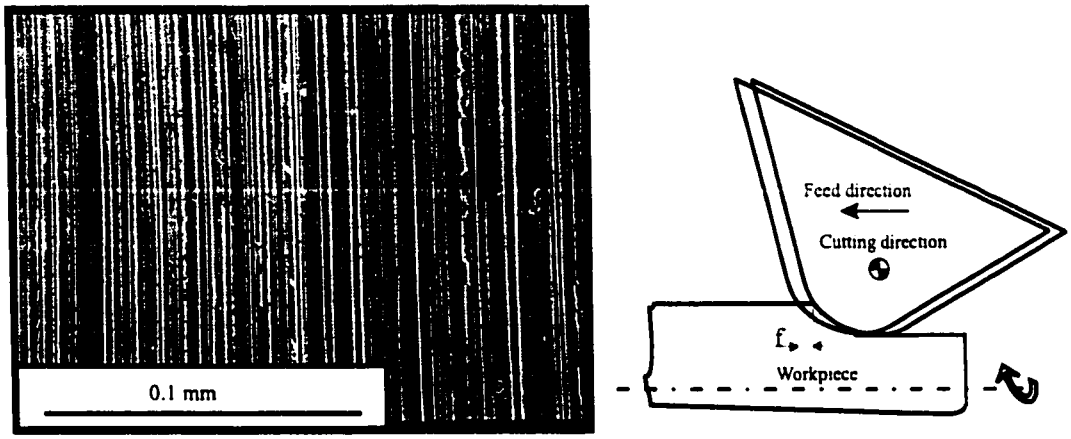

a- Small feed, f = 0.05 mm/rev

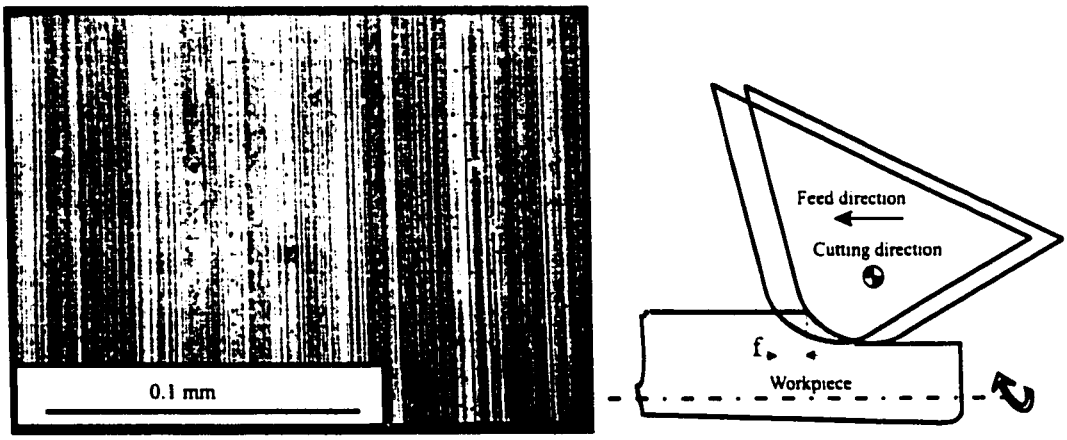

b- Large feed, f = 0.1 mm/rev

Fig. 6.26 Effect of feed on material side flow
(V = 250 m/min, d = 0.125 mm, r = 1.2 mm, chamfered tool)

in which the chip thickness is lower than the minimum chip thickness, (t_{min}). Hence, instead of cutting, a large part of the material is ploughed and leads to material side flow. It should be noted that the side flow exists not only along the feed marks but also along the longitudinal grooves, supporting the hypothesis of material squeezing between the tool flank face and machined surface.

6.7.2 Effect of tool wear

Figure 6.27 shows the effect of tool wear on the surface topography during the machining of hardened steel using a sharp tool. Figure 6.27-a represents the surface produced using a tool with 20 μm flank wear. As cutting progresses the tool becomes more worn and material side flow becomes more severe, as shown in Fig. 6.27-b. However, at a certain level of tool wear, the machined surface appears as a perfect surface consisting of long smooth grooves with relatively high feed ridges, as shown in Fig. 6.27-c. To explain this phenomenon one should consider the wear at the trailing edge of the tool. The groove formed at the trailing edge grows with time and acts as a forming tool that leaves high ridges behind it. The ridges not only contribute to the machined surface roughness, but also serve as a tool producing additional grooves to the side of the first groove as explained previously, and shown in Fig. 6.22. In addition, tool wear has a direct effect on the cutting temperature and cutting forces where a noticeable increase in the thrust force component occurs, as shown in Fig. 6.18. Increasing the thrust force component increases the normal pressure at the cutting zone . Due to the thermal effect of tool wear, the material in the cutting zone

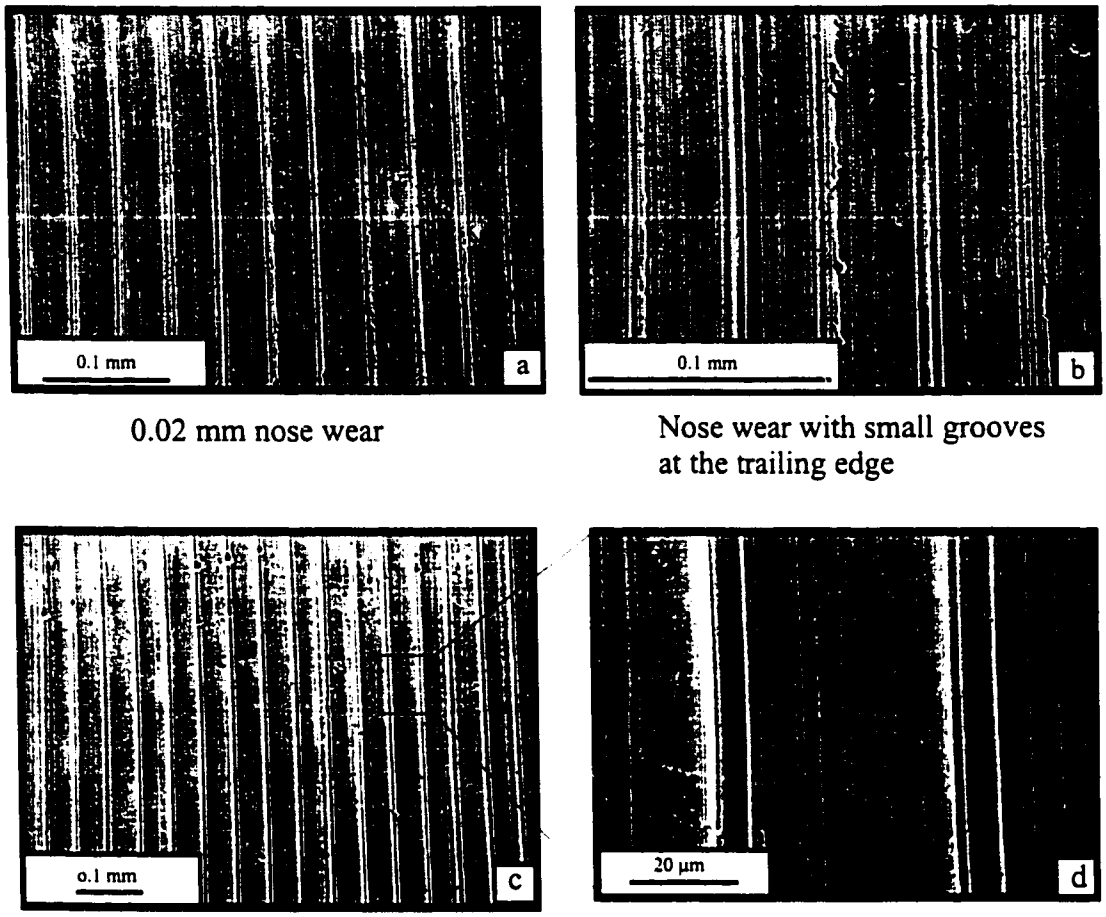

Fig. 6.27 Effect of tool wear on material side flow
(V = 250 m/min, f = 0.05 mm/rev, d = 0.125 mm, r = 0.4 mm, sharp tool)

behaves as a viscous fluid. It fills the grooves and flows in a uniform and homogeneous way to the side of the cutting tool forming high ridges.

6.7.3 Effect of nose radius

Figure 6.28 shows the effect of nose radius on the machined surface topography when cutting with a sharp tool. The material side flow is more defined when using a large nose radius, as shown in Fig. 6.28-a. Again this can be explained by studying the effect of nose radius on the chip formation. During cutting with a tool having a large nose radius, a large part of the chip will have a chip thickness less than the minimum chip thickness value. In addition, increasing the nose radius has a direct effect on cutting forces leading to a significant increase in the ploughing effect in the cutting zone. Increasing the ploughing effect leads to more material side flow on the machined surface.

6.7.4 Effect of edge preparation

Increasing the effective rake angle increases the cutting forces, especially the thrust force component which, in turn, subjects the material in the cutting zone to a high level of normal compressive stress. In addition, high temperatures in the cutting zone facilitate the plastification of the workpiece material and, thus, the material flows to the side in order to relieve this stress. Moreover, the plastic deformation on the cutting edge of a chamfered tool leads to an increase in the effective negative rake angle and, hence, an increase in the pressure on the workpiece in the cutting zone. Figure 6.29 shows a comparison between two

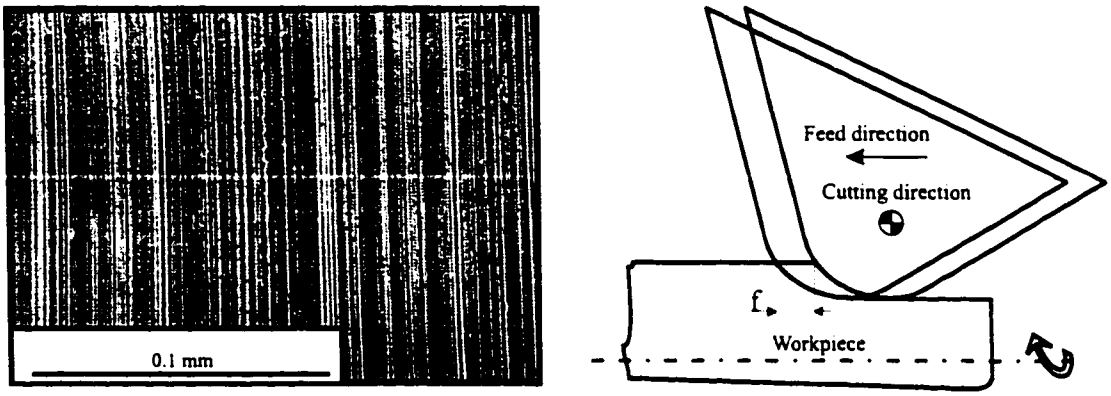

a- Large nose radius, r = 3.2 mm

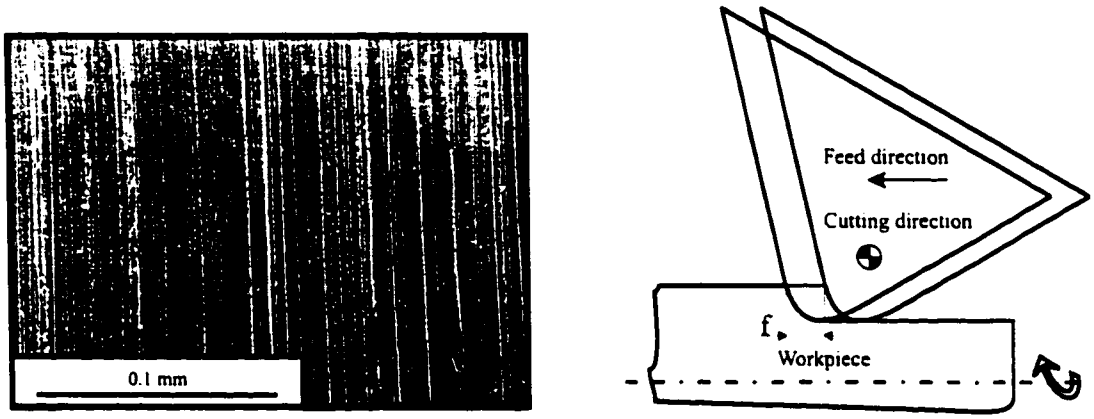

b- Small nose radius, r = 1.2 mm

Fig. 6.28 Effect of nose radius on material side flow
(V = 250 m/min, f = 0.1 mm/rev, d = 0.125 mm, chamfered tool)

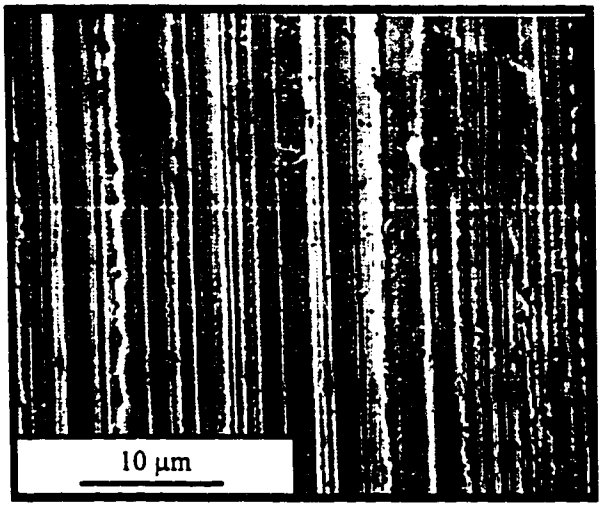

a- Honed tool

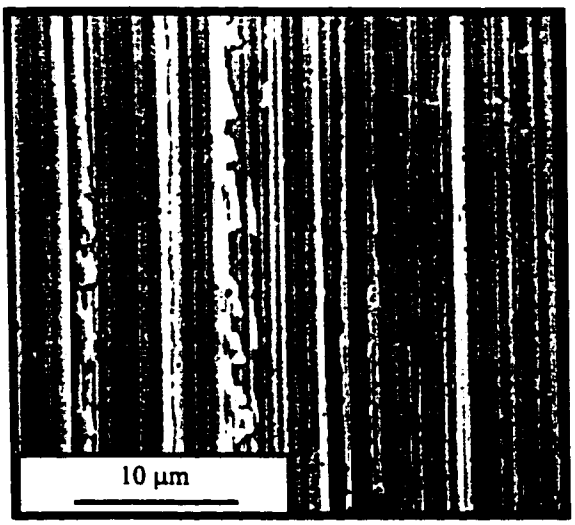

b - Chamfered tool

Fig. 6.29 Effect of edge preparation on material side flow
(V = 250 m/min, f = 0.05 mm/rev, d = 0.125 mm, r = 3.2 mm)

surfaces obtained using honed and chamfered cutting tools. Material side flow is observed when examining the surface machined using a honed cutting edge. The same observation was reported earlier by Chou and Barash (1995), where surface deterioration was observed when using a honed cutting edge. This was attributed to high ploughing which leads to more friction and wear when using a honed tool. In addition, examining the machined surface obtained using a chamfered tool clearly shows more severe plastic material side flow. The increase of material side flow when using honed and chamfered cutting tools can be attributed to the large effective rake angle. The effective rake angle is a function of the honed radius and the undeformed chip thickness for the case of a honed tool, and the chamfered angle in the case of a chamfered tool. This large negative effective rake angle results in more ploughing action and, hence, degrades the machined surface quality.

CHAPTER 7

CONCLUSIONS AND RECOMMENDATIONS

7.1 Introduction

The main objective of this research has been focussed on the analysis of high speed machining of hardened steel. These analyses included the chip formation and the integrity of the machined surface. This chapter starts with a summary and conclusions of the work presented followed by an outline of the main contributions of the work. Finally, recommendations for future work are presented.

7.2 Summary and conclusions

A mechanistic model for the saw toothed chip formation mechanism has been developed. The model explained the kinematics of saw toothed chip formation during the

machining of hardened steel. According to the model presented the chip cross section consists of two main zones. The first one is the fractured part of the chip. The second one is the plastically deformed part of the chip. An experimental investigation has been conducted in order to study the effect of different process parameters on chip morphology. These process parameters included the effect of cutting speed, feed, and edge preparation on the chip morphology. In addition, the effect of process variables on the chip microhardness was investigated. The dynamics of chip formation were also studied experimentally.

The effect of cutting conditions and tool wear on the residual stresses distribution beneath the surface produced during machining of D2 tool steel (62 HRc) was investigated experimentally and analytically. A three dimensional finite element model has been developed in order to predict the distribution of residual stresses beneath the machined surface. In the model presented, the cutting zone was specified based on the tool condition (sharp or worn). X-ray diffraction technique has also been used to measure the residual stresses beneath the machined surface. The residual stresses investigation showed that it is possible to generate a machined surface free of tensile residual stress if the proper cutting conditions and tool configuration are used.

The effect of cutting conditions and tool wear on surface integrity was also investigated experimentally. Different types of surface defects were observed. It has been shown that surface and sub-surface conditions are altered significantly by the cutting speed. The results obtained revealed the dependancy of surface and sub-surface conditions on edge preparation and tool wear, as well as cutting speed. Although a high surface quality was

achieved at a high cutting speed (with a minimum possible surface defects), a sub-surface examination reveals a white layer if the tool is worn. However, there is no noticeable phase change beneath the machined surface when machining at high cutting speed using a sharp tool.

In studying material side flow and based on the results presented, there are two possible mechanisms for the formation of material side flow. In the first mechanism, the workpiece material is squeezed between the tool flank face and the machined surface. This phenomenon is more obvious when the chip thickness is less than a minimum value. Thus, below the minimum chip thickness the material to be cut is ploughed between the tool and the workpiece. The second mechanism is based on the assumption that, under high temperature and pressure, the plastically deformed material is pressed aside. This mechanism of material side flow is facilitated by the trailing edge notch. The trailing edge notch is caused by the chip edge serration.

The main conclusions of this work can be summarized as follows:

1- Saw toothed chips are always formed during the machining of hardened steel.

2- Based on the metallographic analysis there are two different types of deformation zones within a saw toothed chip. Zone one is the chip segment which is caught up between the tool rake face and the crack, and zone two is the plastically deformed segment of the chip.

3- The microhardness test can be used to map out the different deformation zones

through the chip cross section. From the analysis presented, it is obvious that the average microhardness of the chip is significantly altered by the change in the cutting process parameters.

4- Dynamic investigation of the chip formation shows that different combinations of cutting conditions (i.e. cutting speed and feed) have a direct impact on the segmentation frequency of the chip produced. Increasing the feed decreases the segmentation frequency, while cutting speed is in a direct proportion to the segmentation frequency.

5- The fluctuation of the cutting forces in hard turning is the result of chip segmentation and not the cause of it.

6- Cutting tool wear also has a major and direct effect on chip morphology. Roundness of the cutting edge causes chip trailing edge serrations. Consequently, these serrations exist on both sides of the chip edge when the cutting tool is chamfered or given a large angle of approach.

7- High speed machining of die materials in their hardened conditions is feasible, providing that optimum feeds and depth of cuts are chosen.

8- The tensile residual stress induced in the surface is reduced as the feed and depth of cut increases. The distributions of the residual stresses beneath the surface produced depends to a great extent on the tool and cutting conditions.

9- A three dimensional thermo-elasto-plastic finite element model was developed for the numerical simulation of high speed machining of hardened steel. The effects of

material non-linearity, temperature, and large strain were included in the model presented.

10- The finite element predictions of residual stress distributions were comparable to the x-ray diffraction measurement within a 12% error.

11- The predicted tensile residual stress seems to reach a constant level when the applied cutting temperature increases to more than 800 °C. These results show that the cutting temperature has a detrimental effect on the residual stress induced within a specific range of cutting speed.

12- The reduction of the tensile residual stresses as the feed and depth of cut increase can be attributed to the increase in the compressive stresses induced on the workpiece surface by mechanical loads.

13- The magnitude of the surface tensile residual stresses is reduced at high speed machining. In addition, nose radius and type of cutting edge (sharp or honed) affect the produced residual stresses in the machined surface.

14- The effect of cutting speeds on the surface roughness was found to be negligible, and a good surface finish up to 0.5 μm can be obtained regardless of the speeds employed. However, the surface roughness increases with the tool wear because of the material side flow phenomenon, which is one of the major characteristics of hard turned surface.

15- The carbide particles that exist in the workpiece microstructure tend to deform due to the high heat generated during hard turning. Because of their low deformability,

microcracks in the carbide grains exist which create voids and cracks on the surface produced.

16- The shape and geometry of the cutting tools play an important role in determining the nature of surface defects produced during high speed machining of D2 tool steel materials in their hardened conditions.

17- A very thin heat affected zone (white layer of untempered martensite) was present in the surface when a new chamfered tool was used. The thickness of this layer increased to 2 μm when the tool wear was 0.5 mm. The thickness of this heat affected zone depended, to a great extent, on the magnitude of the wear land.

18- Plastic deformation of the grains boundary was observed under all cutting conditions. The plastic deformation of the carbide particles indicates that a very high cutting temperature is generated during the machining of D2 tool steel. The plastic deformation of the grains was found in the first 10-15 μm of the sub-surface layer.

19- Cutting edge preparation has a significant effect upon the material side flow during the machining of hardened steel.

20- Although cutting with a small feed improves the surface finish, it leads to more material side flow on the machined surface and, hence, to a deterioration in the machined surface quality.

21- Increasing the tool nose radius leads to ploughing of a larger part of the chip and, hence, a severe material side flow exists on the machined surface.

7.3 Contributions

The primary contributions of this research lie in obtaining a better understanding of the chip formation mechanism as well as the surface integrity during the high speed machining of hardened steel. Based on the work presented, the main contributions of this research can be summarized as follows:

1- A mechanistic model was developed for the chip formation mechanism in hard turning, which explains the mechanism of saw toothed chip formation. The model developed is based on the assumption that the chip formation starts with the initiation of a crack at the free surface of the workpiece. This crack ceases before reaching the cutting edge where plastic deformation exists due to high compressive stress field and temperature in the vicinity of the cutting tool.

2- The effect of different cutting parameters, cutting edge preparations and tool wear on the chip morphology and dynamics of the chip formation were investigated.

3- A three dimensional finite element model was developed to predict the residual stresses after hard turning. The effect of flank wear on the residual stress distribution beneath the machined surface was introduced during the analysis. An analysis of the effect of mechanical and thermal loads on the residual stress distribution beneath the machined surface was performed using the model presented.

4- Experimental investigation of surface integrity was performed. The investigation included residual stresses, surface quality, surface finish, and the state of deformation in the machined sub-surface layers after hard turning. The experimental investigation

includes the study of the effect of cutting process parameters, tool wear, and cutting edge preparation on surface integrity.

5- An experimental study of the effect of process parameters as well as edge preparation on the phenomenon of material side flow was performed. In this study, two possible mechanisms of material side flow were investigated and the favourable conditions for material side flow were clarified.

7.4 Recommendations for future work

It is suggested that future work in this area can be directed towards the following:

1- The development of a model for material side flow which incorporates the effect of feed and edge preparation.

2- The development of a model for the dynamics of chip segmentation. Thus, the force fluctuation can be determined analytically and, consequently, this would help in studying the cutting tool life.

3- The development of a finite element program to simulate the high speed machining. The model should include the effect of strain rate, temperature, and material phase transformation . An improvement of the finite element model would lead to a better understanding of the mechanism of high speed machining. The model should be able to simulate the chip formation process as well as predicting the plastic deformation and residual stresses in the machined surface.

REFERENCES

Abráo, A. M., and Aspinwall, D. K., 1996, "The Surface Integrity of Turned and Ground Hardened Bearing Steel," Wear, Vol. 196, pp.279-284.

Abráo, A. M., Wise, M. L. H., and Aspinwall, D. K., 1995, "Tool Life and Workpiece Surface Integrity Evaluations When Machining Hardened AISI H13 and AISI E52100 Steels With Conventional Ceramic and PCBN Tool Materials," NAMRC XXIII Conference, May 24-26, Houghton, Michigan, MR95-195, pp. 1-9.

Bailey, J. A., 1974, "On Surface Damage During Machining of AISI 4340 Steel," Wear, Vol. 27, pp. 161-173.

Bailey, J. A., Jeelani, S., and Becker, S. E., 1976, "Surface Integrity in Machining AISI 4340 Steel," Transactions of the ASME, Journal of Engineering for Industry, Vol. 98, No. 3, pp. 999-1006.

Barash, M. M., and Schoech, W. J., 1970, "A Semi-Analytical Model of the Residual Stress Zone in Orthogonal Machining," Proc. 11th International M.T.D.R. Conf., London, Pergamon Press, pp. 603-613.

Bathe, K., J., 1996, "Finite Element Procedures," Prentice Hall, Englewood Cliffs.

Bhattacharyya A., 1984, "Metal Cutting Theory and Practice," Jamini Kanta Sen of Central Book publisher, Calcutta, India.

Black, J. T., 1979, "Flow Stress Model in Metal Cutting," Transactions of the ASME, Journal of Engineering for Industry, Vol. 101, pp. 403-415.

Bresseler, B., El-Wardany, T. I., and Elbestawi, M. A., 1997, "Material Side Flow in High Speed Finish Boring of Case Hardened Steel," 1st French and German Conference

on High Speed Machining, June 17-18, Metz, France, pp. 196-206.

Brinksmeier E., Cammett, J., Konig, W., Leskovar, P., Peters, J., and Tönshoff, H. K., 1982, "Residual Stresses-Measurement and Causes in Machining Processes,"Annals of the CIRP Vol. 31/2, pp. 491-510.

Chou, Y., and Barash, M., 1995, "Review on Hard Turning and CBN Cutting Tools," 1st International Machining and Grinding Conference, SME, MR95-215, Sep. 12-14, Dearborn, Mechigan, pp. 951-962.

Buschmohle, N., 1995, "Hard Turning with Ceramics," 1st International Machining and Grinding Conference, SME, Dearborn, Michigon, pp. 981-987.

Chou, Y. K. and Evans, C. J., 1996, "Microstructural Effects in Precision Hard Turning," Proc. ASME. International Mechanical Engineering Congress and Exposition, Manufacturing Science and Engineering, MED-Vol. 4,, pp. 237-242.

Cook, N. H., Finnie, I., Shaw, M. C., Mass, C., 1954, "Discontinuous Chip Formation," Transactions of the ASME, Vol. 76, pp. 153-162.

Cullity, B. D., 1978, "Elements of X-ray Diffraction," Addison-Wesely Publishing Company, INC. Second Edition.

Davies, M. A., Chou, Y., and Evans, C. J., 1996, "On Chip Morphology, Tool Wear and Cutting Mechanics in Finish Hard Turning," Annals of the CIRP, Vol 45, pp. 77- 82

Elbestawi, M. A., Srivastava, A. K., and El-wardany, T., 1996, "A model for Chip Formation During Machining of Hardened Steel,"Annals of the CIRP, Vol 45, pp. 71-76.

Elbestawi, M. A., Chen, L., Becze, C. E., and El-Wardany, T. I., 1997, "High Speed Milling of Dies and Moulds in their Hardened State," Annals of the CIRP Vol. 46, pp. 57-62.

El-Khabeery, M. M., and Fattouh, M., 1989, "Residual Stress Distribution Caused by Milling," Int. J. Mach. Tools Manufact., Vol. 29/3, pp. 391- 401.

Eyre, T. S. and Baxter, A., 1972, "The Formation of White Layers at Rubbing Surfaces," Tribology, Vol. 12, pp. 256-261.

El-Wardany, T. I., Elbestawi, M. A. , Attia, M.H., , and Mohammed, E. , 1992, "Surface Finish Characteristics in Turning of Hardened Steel," Proc. ASME, International Mechanical Engineering Congress and Exposition, Engineered Surfaces, PED. Vol. 62, pp. 146-160.

El-Wardany, T. I., Mohammed, E., and Elbestawi, M. A., 1993, "Material Side Flow in Finish Turning of Hardened Steel with Ceramic Tools," Proc. ASME, International Mechanical Engineering Congress and Exposition, PED-Vol. 67/TRIB-Vol. 4, pp. 159-170.

El-wardany, T. I., Boelhouwer, A. M. and Elbestawi, M. A., 1995, "High speed Machining of Nickel-Based Super Alloys with Silicon Carbide Whisker Reinforced Ceramic," 1st International Machining and grinding conference, SME, Dearborn, Michigan. pp. 3-28.

El-wardany, T.I., Mohammed, E., and Elbestawi, M. A., 1996, "Cutting Temperature of Ceramic Tools in High Speed Machining of Difficult-To-Cut Materials," Int. J. Mach. Tools Manufact., Vol. 36, No. 5, pp. 611-634.

Field, M., and Kahles, J., 1971, "Review of Surface Integrity of Machined Components," Annals of the CIRP Vol. 20/2, pp. 153-163.

Field, M., Koster, W. P., Kohls, J. B., Snider, R. E., and Maranchic, J., 1970, "Machining of High Strength Steels With Emphasis on Surface Integrity," Technical Report AFML-TR-70-11, Air Force Material Laboratory, MATF, Wright-Patterson Air Force Base, Ohio, U.S.A.

Field, M. and Merchant, M. E., 1949, "Mechanics of Formation of The Discontinuous Chip in Metal Cutting," Transactions of the ASME, Vol. 71, pp. 421-430.

Gill, J. P., Rose, R., S., Roberts, G. A., Johnstin, H.G. and George, R. B., 1944, "Tool Steels," The American Society for Metals, Cleveland, Ohio.

Hilly, M. E., J. A. Larson, C. F. Jatczak, and R. E. Ricklefs, 1980, "Residual Stress Measurement by X-Ray Diffraction," SAE Information Report J784, Society of Automotive Engineers, INC. Second Edition

Hodgson, T., and Trendler, P. H. H., 1981, "Turning Hardened Tool Steels with Cubic Born Nitride Inserts," Annals of the CIRP, Vol. 30, pp. 63-66

Ikeda, T., Takahashi, I, Matsuoka, T. and Nakagawa, T., 1992, "Ultra High Speed Milling of Die Steel with Ball-nose End Mill," Proc. 2nd Int. Conf. On Die and Mold Technology, Singapore, Sept., pp 48-56.

Jain, V. K., Kumar, S., and Lai, G. K., 1989, "Effects of Machining Parameters on the Microhardness of Chips," ASME, Journal of Engineering for Industry, Vol 111, pp. 220-228.

Kloss, K. H., and Kaiser, B., 1990, "Residual Stresses Induced by Manufacturing," Association for Heat Treatment and Materials Technology and German Society for Material Science and Technology, pp. 205-226.

Koistinen, D. P. and Maburger, R. E., 1959, "A Simplified Procedure for Calculating Peak Position in X-Ray Residual Stress Measurements on Hardened Steel,"Transactions of the ASME, Vol. 51, pp. 537-550.

Komanduri, R. and Brown, R. H., 1981, "On the Mechanics of Chip Formation in Machining," Transaction of the ASME, Journal of Engineering for Industry, Vol 103, pp. 33-51.

Komanduri, R., Schroeder, T., Hazra, J., Von Turkovich, B. F., and Flom D. G., 1982, "On the Catastrophic Shear Instability in High-Speed Machining of an AISI 4340 Steel, " Transaction of the ASME, Journal of Engineering for Industry, Vol. 104, pp. 121-131.

Kono, Y., Hara, A., Yazu, S., Uchida, T., and Mori, Y., 1980, "Cutting Performance of Sintered CBN Tools," Cutting Tool Materials, Proceedings of the International Conference, American Society for Metals, Ft. Mitchell, Kentucky, September 15-17, pp. 281-295.

König, W., Cronjager, L., Spur, G., Tönshoff, H. K., Vigneau, M., and Zdeblick, W. J., 1991, "Machining of New Materials," Processing of Advanced Materials, Vol. 1, pp. 11-26.

Koistinen, D. P. and Maburger, R. E., 1959, "A Simplified Procedure for Calculating Peak Position in X-Ray Residual Stress Measurements on Hardened Steel," Transactions. ASM, Vol. 51, pp. 537-550.

König, W., Komanduri, R., Tonshoff, H. K., and Ackershott, G., 1990, "Machining of Hard Materials," Annals of the CIRP Vol. 39/1, pp. 417-427.

König, W., Berktold, A., and Koch, F. K., 1993, "Turning Versus Grinding- A Comparison of Surface Integrity Aspects and Attainable Accuracies," Annals of the CIRP, Vol. 42, pp. 39-43.

Lajczok, M. R., 1980, "A Study of Some Aspects of Metal Machining Using the Finite Element Method," Ph. D. Dissertation, North Carolina State University.

Lapsley, J. L., Grassi, R. C., and Thomsen, E. G., 1950, "Correlation of Plastic Deformation During Metal Cutting With Tensile Properties of the Work Material," Transactions of the ASME, Journal of Engineering for Industry, Vol. 72, pp 979-985.

Lee, E. H., and Shaffer, B. W., 1951, "The Theory of Plasticity Applied to a Problem of Machining," Transactions of the ASME, Journal of Applied Mechanics, Vol. 73, pp. 404-413.

Leskovar, P., Peklenik, J., 1982, "Influences Affecting Surface Integrity in the Cutting Process," Annals of the CIRP Vol. 31/1, pp. 447-450.

Lin, Z. C., Lin, Y. Y. and Liu, C. R., 1991, "Effect of Thermal Load and Mechanical Load on the Residual Stress of a Machined Workpiece," Int. J. Mech. Sci. Vol. 33, No. 4, pp. 263-278.

Lindberg, B., and Lindstörm, B., 1983, "Measurements of the Segmentation Frequency in the Chip Formation Process," Annals of the CIRP, Vol. 32, pp. 17-20.

Liu, C. R., and Barash, M. M., 1982, "Variables Governing Patterns of Mechanical Residual Stress in a Machined Surface," Transactions of the ASME, Journal of Engineering for Industry, Vol. 104, No.3, pp. 257-264.

Liu, C. R. and Lin, Z. C., 1985, "Effects of Shear Plane Boundary Condition on Stress Loading in Orthogonal Machining," Int. J. Mech. Sci. Vol. 27, No. 5, pp. 281-290.

Maekawa, K., Nakano, Y., Kitagawa, T., 1996, "Finite Element Analysis of Thermal Behaviour in Metal Machining, 1st Report, Influence of Thermophysical Properties on Cutting Temperature," Transactions Jpn. Soc. Mech. Eng., Vol. 62, No. 596, C, pp. 857-863.

Mallock, A., 1882, "The Action of Cutting Tools," Proc. Soc., Vol. 33, p.127

Matsumoto, Y., Barash, M. M., and Liu, C. R., 1986, "Effect of Hardness on the Surface Integrity of AISI 4340 Steel," Transactions of the ASME, Journal of Engineering for Industry, Vol. 108, No. 3, pp. 169-175.

Merchant, M, 1945, "Mechanics of Metal Cutting Process. I. Orthogonal Cutting and a Type 2 Chip," Journal of Applied Physics, Vol. 16, No. 5, pp. 267-275.

Meyers, M. A., 1994, "Dynamic Behavior of Materials," John Wiley and Sons, Inc

Mills, A. F., 1992, "Heat transfer," Irwin, Boston, pp. 330-331.

Mishra, A. and Prasad, T., 1985, "Residual Stresses Due to A Moving Heat Source," Int. J. Mech. Sci. Vol. 27, No. 9, pp. 571-581.

Moore, M. G. and Evans, W. P., 1958, "Mathematical Correction for Stress in Removal layers in X-Ray Diffraction Residual Stress Analysis," Transactions. SAE, Vol. 66, pp. 340-345.

Nakayama, K., 1974, "The Formation of Saw-toothed Chip in Metal Cutting," Proceedings of International Conference on Production Engineering, Tokyo, pp. 572-577.

Nakayama, K., Arai, M. and Kanda, T, 1988, "Machining Characteristic of Hard Materials," Annals of the CIRP, Vol. 37, pp. 89-92.

Nakayama, K., and Arai, M., 1992, "Comprehensive Chip Form Classification Based on the Cutting Mechanism," Annals of the CIRP, Vol. 71, pp. 71-74.

Natarajan, R., and Jeelani, S., 1983, "Residual Stresses in Machining Using Finite Element Method," Computers in Engineering, Computer Software and Applications, Vol. 3, ASME, New York, pp, 19-20.

Obikawa, T., Usui, E., 1996, "Computational Machining of Titanium Alloy-Finite Element Modeling and a Few Results," Transactions of the ASME, Journal of Engineering for Industry, Vol. 118, No.2, pp. 208-215.

Ogata, M., 1989, "Einsatz von PCBN-Werkzeugen in der Produktion," VDI Berichte, No. 762, pp. 271-279.

Oishi, K., 1995, "Built-up Edge Elimination in Mirror Cutting of Hardened Steel," Transactions of the ASME, Journal of Engineering for Industry, Vol. 117, No. 1, pp. 62-66.

Okushima, K., and Kakino, Y., 1971, "The Residual Stress Produced by Metal Cutting," Annals of the CIRP, Vol. 10, pp. 13-14.

Palmer, W. B., and Oxley, P. L. B., 1959, "Mechanics of Orthogonal Machining," Proc. Instn. Mech. Engrs., Vol. 173, No. 24, pp. 623-638.

Palmer, W. B., 1967, "Plastic Deformation When Cutting Into an Inclined Plane," Jornal of Mechanical Engineering Science, Vol. 9, No. 1, pp. 1-9.

Park, Y. W., Cohen, P. H., and Ruud, C. O., 1993, "The Development of Mathematical Model for Predicting the Depth of Plastic Deformation in a Machined Surface," Materials and Manufacturing Processes, Vol. 8, No. 6, pp. 703-715.

Pekelharing, A. J. and Gieszen, C. A., 1971, "Material Side Flow in Finish Turning," Annals of the CIRP, Vol. 20, pp. 21-22.

Poggie, R. A. and Wert, J. J., 1991, "The Influence of Surface Finish and Strain Hardening on Near Surface Residual Stress and the Friction and Wear Behaviour of A2, D2 and CPM-10V Tool Steels," Wear of Materials, ASME, pp. 497-501.

Prevey, P. S., 1986, "A Method of Determining the Elastic Properties of Alloys in Selected Crystallographic frictions for X-Ray Diffraction Residual Stress Measurement," Adv. In X-Ray Anal., Vol. 20, pp. 345-354.

Recht, R. F., 1964, "Catastrophic Thermoplastic Shear," Journal of Applied Mechanics, Transactions of the ASME, Vol. 86, pp. 189-193.

Rigby, P., 1993, "High Speed Milling in the Mould and Die Making Industries," Diamond and CBN Ultra Hard Materials Symposium-93, Ontario, Canada.

Roberts, G. A., Hamaker, Jr., J. C. and Johnson, A. R., 1962, "Tool Steels," The American Society for Metals, 3rd Edition, Metals, Park, Ohio.

Sadat, A. B., 1990,"Effect of High Speed on Surface Integrity of AISI 4340 Steel During Turning," Material Science and Technology, Vol. 6, pp. 371-375.

Sadat, A. B., and Baiely, J. A., 1987,"Residual Stresses in Turned AISI 4340 Steel," Experimental Mechanics, Vol. 27, No. 1, pp. 80-85.

Schreiber, E., and Schlicht, H., 1986, "Residual Stresses After Turning of Hardened Components," The International Conference on Residual Stresses, Garnish - Partenkirchen (FRG), pp. 853-860.

Semiatin, S. L., and Rao, S. B., 1983, "Shear Localization During Metal Cutting," Materials Science and Engineering, Vol. 61, pp. 185-192.

Shaw, M. C., and Vyas, A., 1993, "Chip Formation in the Machining of Hardened Steel," Annals of the CIRP, Vol. 42, pp. 29-33.

Shaw, M. C., 1995, "Precision Finishing," Annals of the CIRP, Vol.44, pp. 343-348.

Shaw, M. C., 1984, "Metal Cutting Principles," Oxford Science Publications, New York

Shih, A. J., 1995, "Finite Element Simulation of Orthogonal Metal Cutting," Transactions of the ASME, Journal of Engineering for Industry, Vol. 117, No. 1, pp. 84-91.

Shih, A. J., 1993, "Finite Element Analysis of the Rake Angle Effects in Orthogonal Metal Cutting," Proc. ASME, International Mechanical Engineering Congress and Exposition, PED-Vol. 64, Manufacturing Science and Engineering, pp. 475-483.

Shih, A. J. and Yang, H. T. Y., 1993, "Experimental and Finite Element Predictions of Residual Stresses due to Orthogonal Metal Cutting," Int. J. for Numerical Methods in Engineering. Vol. 36, pp. 1487-1507.

Sowerby, R. And Chandrasekaran, N., 1989, "A Proposal for the Onset of Chip Segmentation in Machining," Materials Science and Engineering, A., Vol. 119, pp. 219-229.

Thomsen, E. G., 1966, "Application of the Mechanics of Plastic Deformation to Metal Cutting," Annals of the CIRP, Vol. 14, pp. 113-117.

Tlusty, J., and Masood, Z., 1978, "Chipping and Breakage of Carbide Tools," Transactions of the ASME, Journal of Engineering for Industry, Vol. 100, No. 4, pp. 403-412.

Tönshoff, H. K. and Bartsch, S., 1988, "Wear Mechanisms of Ceramics Cutting Tools," Ceramic Bulletin, Vol. 67, No. 6, pp. 1020-1025.

Tönshoff, H. K., Wobker, H. G., and Brandt, D., 1995a, "Tribological Aspects of Hard Turning with Ceramic Tools," Journal of the Society of Tribologists and Lubrication Engineers, Vol. 51, No.2, pp 163-168.

Tönshoff, H. K., Wobker, H. G., and Brandt, D., 1995b, "Hard Turning - Influences on the Workpiece Properties," Transactions of NAMRI/SME, Vol. XXIII, pp. 215-220.

Tönshoff, H. K., Wobker, H. G., and Brandt, D., 1995c, "Potential and Limitation of Hard Turning," 1st International Machining and Grinding Conference, MR95-215, Sep. 12-14, Dearborn, Mechigan.pp 965-977.

Trent, E. M., 1991, "Metal Cutting," Butterworth-Heinemann Ltd, Third Edition.

Wang, B. P., Sadat, A. B., and Twu, M. J., 1988, "Finite Element Simulation of Orthogonal Cutting-A Survey," Proc. ASME, International Mechanical Engineering Congress and Exposition, Chicago, IL, pp. 322-329

Warnecke, G. and Bach, P., 1988, "Mechanical and Material Influences on Machined Surface in Precision Turning of Steel With Ceramics," Proc. of the 16th North American Research Conference, pp. 209-216.

Wu, D. W., and Matsumoto, Y., 1990, "The Effect of Hardness on Residual Stresses in Orthogonal Machining of AISI 4340 Steel," Transactions of the ASME, Journal of Engineering for Industry, Vol. 112, No.3, pp. 245-252.

Zhang, B. and Bagchi, A., 1994, "Finite Element Simulation of Chip Formation and Comparison with Machining Experiment," Transactions of the ASME, Journal of Engineering for Industry, Vol. 116, No. 3, pp. 289-297.

APPENDIX A

CONSTITUTIVE EQUATIONS

Constitutive equations describe the relation between stress and strain in elastic, or plastic regimes in terms of strain rate and temperature. General form of a constitutive equation is given in this form:

$$f\left(\sigma, \varepsilon, \dot{\varepsilon}, \mathrm{T}\right) = 0 \qquad \text{(A.1)}$$

where ε, $\dot{\varepsilon}$ and T are strain, strain rate and temperature, respectively.

Machining operations involve high temperature and high strain rates, thus, a constitutive equation that describe the material behaviour at high temperature and strain rate is required. There are many constitutive equations that have been proposed and successfully used to describe the material plastic behaviour as a function of the applied temperature and strain rate.

For small strain rate material works harden and follows the following parabolic

hardening equation:

$$\sigma = \sigma_0 + k\varepsilon^n \tag{A.2}$$

where σ, σ_o , n, and K are the working stress, yield stress, hardening coefficient and exponential factor, respectively. Strain rate has a direct effect on the material behaviour such that:

$$\sigma \; \alpha \; \ln \varepsilon \tag{A.3}$$

However, this equation is valid only at strain rates that are not too high. Other forms of constitutive equations that describe the effect of temperature on the flow stress of the material can be represented by:

$$\sigma = \sigma_r \left[1 - \left(\frac{T - T_r}{T_m - T_r} \right)^m \right] \tag{A.4}$$

where T_m is the melting point, T_r is a reference temperature at which the reference stress, σ_r is measured, and T is the temperature for which σ is calculated. The constants in the empirical constitutive equations are normally measured experimentally using a simple curve fitting method.

A general constitutive equation was proposed by Johnson and Cook (Meyers, 1994)

where the effect of both temperature and strain rate are included.

$$\sigma = \left(\sigma_0 + B\varepsilon^n\right)\left(1 + C\ \ln\frac{\dot{\varepsilon}}{\dot{\varepsilon}_0}\right)\left[1 - \left(T^*\right)^m\right] \tag{A.5}$$

where σ_0, B, C, n, and m are five constants that can be determined experimentally. The temperature's term (T*) is given by:

$$T^* = \frac{T - T_r}{T_m - T_r}$$

where T_r is the reference temperature at which σ_0 is measured and $\dot{\varepsilon}_0$ is a reference strain rate that can be, for convenience, made equal to one. This equation has been tested on many materials and successfully described the material behaviour under different strain rates and temperatures. More details about the empirical constitutive equations can be found in Meyers (1994) from which the material presented was obtained.

APPENDIX B

A SAMPLE OF THE FINITE ELEMENT INPUT FILES

```
Prepared by DECODN 1.30 -S
$FREE

***Master control lines***
1089 0 0 0 1 1 1 0 1 1 20 0.500000E-01 0.000000E+00 4 9.000000E-01 0 0 11.14
0 0 0 0 0 0 0 0 1
0 0 0 0 0 0 0 0 0
0 0 0 0 0
0 0 0.000000E+00 1
1 0 1 50 2.000000E-03 1.000000E+00 5.000000E-01 0 1 0 0 0
0 0.000000E+00 0.000000E+00
0 0 0 0

***Nodal Points***
1 1 1 1 1 1 1 0.000000e+00 -4.500000e+01 -1.000000e+02 0 5.688100e+01
2 1 1 1 1 1 1 1.318500e+01 -4.060000e+01 -1.000000e+02 0 5.688200e+01
3 1 1 1 1 1 1 -2.250000e+01 -3.897115e+01 -1.000000e+02 0 5.686500e+01
4 1 1 1 1 1 1 2.637000e+01 -3.620000e+01 -1.000000e+02 0 5.684100e+01
5 1 1 1 1 1 1 3.626000e+01 -2.630000e+01 -1.000000e+02 0 5.679900e+01
6 1 1 1 1 1 1 -3.897114e+01 -2.250000e+01 -1.000000e+02 0 5.685300e+01
7 1 1 1 1 1 1 -2.258838e+01 -2.092982e+01 -1.000000e+02 0 5.694100e+01
8 1 1 1 1 1 1 0.000000e+00 -1.848500e+01 -1.000000e+02 0 5.699600e+01
9 1 1 1 1 1 1 1.315580e+01 -1.726300e+01 -1.000000e+02 0 5.696800e+01
```

10 1 1 1 1 1 1 2.630107e+01 -1.573532e+01 -1.000000e+02 0 5.690200e+01
11 1 1 1 1 1 1 3.638451e+01 -1.451308e+01 -1.000000e+02 0 5.686300e+01
12 1 1 1 1 1 1 4.260000e+01 -1.380000e+01 -1.000000e+02 0 5.687300e+01
13 1 1 1 1 1 1 4.336930e+01 -9.277088e+00 -1.000000e+02 0 5.690600e+01
14 1 1 1 1 1 1 4.413859e+01 -4.754177e+00 -1.000000e+02 0 5.687600e+01
15 1 1 1 1 1 1 4.490789e+01 -2.312651e-01 -1.000000e+02 0 5.677600e+01
16 1 1 1 1 1 1 4.492400e+01 -1.460780e-01 -1.000000e+02 0 5.679100e+01
17 1 1 1 1 1 1 4.493230e+01 -1.000000e-01 -1.000000e+02 0 5.681400e+01
18 1 1 1 1 1 1 -4.498700e+01 -5.000000e-02 -1.000000e+02 0 5.684300e+01
19 1 1 1 1 1 1 -3.897100e+01 -5.000000e-02 -1.000000e+02 0 5.688200e+01
20 1 1 1 1 1 1 -2.250000e+01 -5.000000e-02 -1.000000e+02 0 5.697200e+01
21 1 1 1 1 1 1 0.000000e+00 -5.000000e-02 -1.000000e+02 0 5.701700e+01
22 1 1 1 1 1 1 1.315580e+01 -5.000000e-02 -1.000000e+02 0 5.697800e+01
23 1 1 1 1 1 1 2.631160e+01 -5.000000e-02 -1.000000e+02 0 5.692300e+01
24 1 1 1 1 1 1 3.625990e+01 -5.000000e-02 -1.000000e+02 0 5.698300e+01
25 1 1 1 1 1 1 4.259985e+01 -5.000000e-02 -1.000000e+02 0 5.694800e+01
26 1 1 1 1 1 1 4.336520e+01 -5.010000e-02 -1.000000e+02 0 5.687900e+01
27 1 1 1 1 1 1 4.413570e+01 -5.010000e-02 -1.000000e+02 0 5.679600e+01
28 1 1 1 1 1 1 4.490770e+01 -5.010000e-02 -1.000000e+02 0 5.681300e+01
29 1 1 1 1 1 1 4.492400e+01 -5.010000e-02 -1.000000e+02 0 5.684000e+01
30 1 1 1 1 1 1 4.493229e+01 -5.017777e-02 -1.000000e+02 0 5.685800e+01
31 1 1 1 1 1 1 4.494115e+01 -5.000000e-02 -1.000000e+02 0 5.687500e+01
Applied Loads
24 2 4
1 4
0.000000E+00 0.000000E+00 5.000000E-01 1.000000E+00 6.000000E-01
1.000000E+00 1.000000E+00 0.000000E+00
2 4
0.000000E+00 0.000000E+00 5.000000E-01 1.000000E+00 6.000000E-01
1.000000E+00 1.000000E+00 0.000000E+00
355 3 1 -5.000000E+00
355 2 1 8.000000E+00
355 1 1 -1.000000E+01
370 1 1 -2.000000E+01
370 2 1 1.700000E+01
370 3 1 -1.000000E+01
445 2 1 8.000000E+00
445 3 1 -5.000000E+00
445 1 1 -1.000000E+01
460 3 1 -1.000000E+01
460 2 1 1.700000E+01
460 1 1 -2.000000E+01

```
535 2 1 8.000000E+00
535 3 1 -5.000000E+00
535 1 1 -1.000000E+01
550 3 1 -1.000000E+01
550 2 1 1.700000E+01
550 1 1 -2.000000E+01
625 2 1 8.000000E+00
625 3 1 -5.000000E+00
625 1 1 -1.000000E+01
640 3 1 -1.000000E+01
640 2 1 1.700000E+01
640 1 1 -2.000000E+01
***Thermal Loading***
1
2
***Initial Conditions***
0 1
***3-D Elements***
25 846 2 0 0 0 8 0 0 3 3 0 0 0 10 1 16 0
1 7.800000E-06
2 0.0 0 0
0.00e+00      5.00e+02
2.060000E+05  2.060000E+05
3.000000E-01  3.000000E-01
1.12e-05      1.12e-05
4.900000E+02  4.900000E+02
2.060000E+03  2.060000E+03
1 8 8 1 1 0 0
1 3 7 8 82 84 88 89
0 0 0 0 0 0 0 0 0 0 0 0 0 0
2 8 8 1 1 0 0
9 2 1 8 90 83 82 89
0 0 0 0 0 0 0 0 0 0 0 0 0 0
3 8 8 1 1 0 0
3 6 7 7 84 87 88 88
0 0 0 0 0 0 0 0 0 0 0 0 0 0
4 8 8 1 1 0 0
4 2 9 10 85 83 90 91
0 0 0 0 0 0 0 0 0 0 0 0 0 0
5 8 8 1 1 0 0
5 4 10 11 86 85 91 92
0 0 0 0 0 0 0 0 0 0 0 0 0 0
```

6 8 8 1 1 0 0
5 11 12 12 86 92 93 93
0 0 0 0 0 0 0 0 0 0 0 0 0
7 8 8 1 1 0 0
20 7 6 19 101 88 87 100
0 0 0 0 0 0 0 0 0 0 0 0 0
8 8 8 1 1 0 0
21 8 7 20 102 89 88 101
0 0 0 0 0 0 0 0 0 0 0 0 0
9 8 8 1 1 0 0
22 9 8 21 103 90 89 102
0 0 0 0 0 0 0 0 0 0 0 0 0
10 8 8 1 1 0 0
23 10 9 22 104 91 90 103
0 0 0 0 0 0 0 0 0 0 0 0 0
11 8 8 1 1 0 0
24 11 10 23 105 92 91 104
0 0 0 0 0 0 0 0 0 0 0 0 0
12 8 8 1 1 0 0
6 18 19 19 87 99 100 100
0 0 0 0 0 0 0 0 0 0 0 0 0
13 8 8 1 1 0 0
25 12 11 24 106 93 92 105
0 0 0 0 0 0 0 0 0 0 0 0 0
14 8 8 1 1 0 0
26 13 12 25 107 94 93 106
0 0 0 0 0 0 0 0 0 0 0 0 0
15 8 8 1 1 0 0
27 14 13 26 108 95 94 107
0 0 0 0 0 0 0 0 0 0 0 0 0
16 8 8 1 1 0 0
28 15 14 27 109 96 95 108
0 0 0 0 0 0 0 0 0 0 0 0 0
17 8 8 1 1 0 0
29 16 15 28 110 97 96 109
0 0 0 0 0 0 0 0 0 0 0 0 0
18 8 8 1 1 0 0
30 17 16 29 111 98 97 110
0 0 0 0 0 0 0 0 0 0 0 0 0
19 8 8 1 1 0 0
17 30 31 31 98 111 112 112
0 0 0 0 0 0 0 0 0 0 0 0 0